# Plexcitonics – Fundamental principles and optoelectronic applications

Ajay P. Manuel,[1] Aaron Kirkey,[2] Najia Mahdi[1] and Karthik Shankar[1]

[1]Department of Electrical and Computer Engineering, University of Alberta, Edmonton, AB, T6G 2V4, Canada

[2] Department of Chemistry, University of Alberta, Edmonton, AB, T6G 2G2, Canada

## Abstract

The nanoscale confinement and coupling of electromagnetic radiation into plexcitonic modes has drawn immense interest because of the innovative possibilities for their application in light harvesting and light emitting devices (LEDs). Plexcitons arise from the coupling between two types of quasiparticles, plasmons and excitons, and can be distinguished by the strength of the coupling into strong and weak coupling regimes. Plexcitons have been used to modulate the rate of Förster-type resonance energy transfer in quantum dot assemblies and enhance the spontaneous emission rate in quantum dot LEDs. The clearest examples of a plexcitonic enhancement of photocatalytic reaction rates have been evidenced in hybrid systems wherein the strongly bound exciton found in 2D sheet-like semiconductors is coupled to the surface plasmon resonance of close-lying noble metal nanoparticles. Plexcitonic photocatalysts and solar cells aim to increase the lifetime of hot carriers and thereby enhance the quantum yields for energy harvesting. Since plexcitonics requires the placement of plasmonic and excitonic components in close proximity with one another to facilitate their coupling, it provides a rich arena for chemists and materials scientists to form deterministic and non-deterministic arrays and heterojunctions involving noble metal thin films and nanostructures, quantum dots and dye molecules. This review summarizes the dynamics of plexcitons in the various composite systems and provides an overview of the latest theoretical and experimental developments in the field of plexcitonics.

Keywords: J-aggregates, plasmonic dimers, core-shell nanoparticles, corrugated silver films, 2D semiconductor nanosheets, nanodisk arrays, electron beam lithography

# Table of Contents

## 1. Introduction

The study and design of devices that are capable of harnessing and controlling light-matter interactions at the nanoscale have long been subjects of intense research activity.[1] Metallic nanostructures are considered most ideal for this purpose since they have the ability to focus and confine optical energy in subwavelength spatial regions.[2] The resultant diverse modes of behavior observed upon the interaction of electromagnetic radiation with metallic nanostructures serve as probes that reflect properties of the material system as well as the formation of hybrid states of light and matter that display properties of both.[3] The most explicit of said manifestations are polaritons – quasiparticles that result from the mixing of electromagnetic radiation with the polar excitation of a material. Polaritons encompass a wide variety of light-matter hybrids including exciton-polaritons, plasmons, and plexcitons, to name a few (Fig. 1).[4] Investigations of these quasiparticles have revealed much about the nature of light-matter interactions at the nanoscale while promoting the exploitation of said phenomena in nanophotonic applications including light-emitting diodes, solar cells, photocatalysis, quantum information processing, catalysis, environmental science, and telecommunications.[5]

The focus of this review is to provide a theoretical and experimental overview of one such light-matter hybrid, the plexciton. It is imperative that we begin by considering the theoretical principles used to describe plexcitons. This review will provide an outline of recent progress that has resulted in the proliferation of plexcitonic applications.

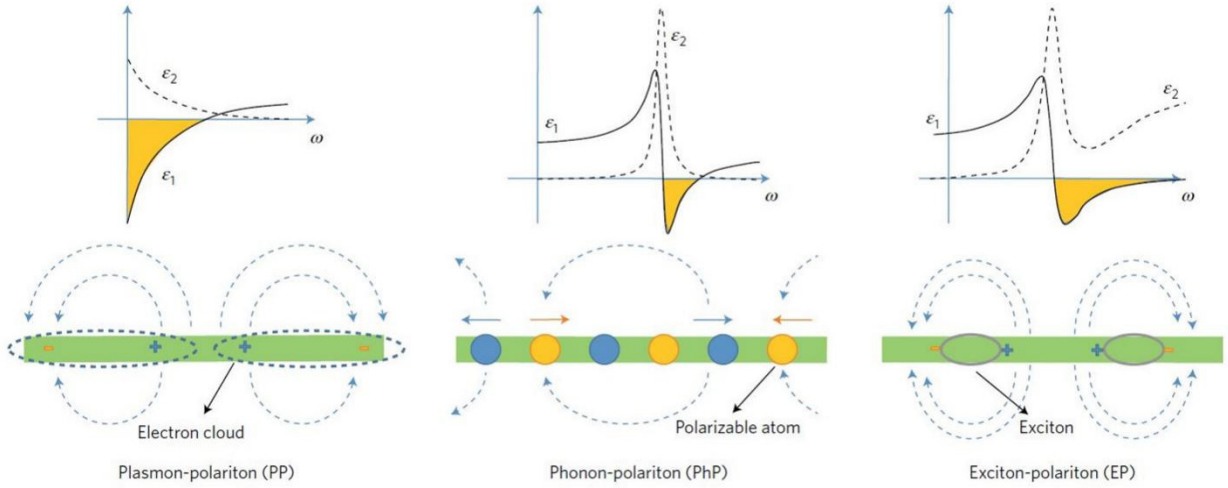


**Fig. 1 Flavors of Light-Matter Interactions**. Polaritons characterize the diverse modes of light-matter interactions that occur at the nanoscale which subsequently result in the formation of exotic states of light and matter displaying properties of both. These light-matter hybrids or quasiparticles each identify with a different mode of interaction or "coupling" between the incident light and a material structure: exciton-polaritons involve the coupling of light and excitons, phonon polaritons involve the coupling of light with the phononic modes of a semiconductor or polar dielectric, and lastly, plasmon-polaritons describe the coupling of light with the collective and coherent motion of delocalized electrons at a metal-dielectric interface. Reprinted with permission from Ref[6]. Copyright Nature Publishing Group (2016).

## 2. What are Plexcitons?

Plexcitons are an amalgamation of excitons and plasmons; they are polaritonic modes that essentially describe the interaction or *coupling* of plasmons and excitons.[7, 8] The concept of excitons was first introduced by Frenkel in 1931 and Peierls in 1932 in the form of "excitation waves" when light is absorbed and transformed into heat in solids.[9, 10] An exciton is an electrically neutral quasi-particle involving the bound state of an electron and a hole attracted to each other by the electrostatic Coulomb force. Excitons can exist in a variety of materials ranging from semiconductors to insulators, and are further classified as Frenkel, Mott-Wannier, and Davydov excitons based on the strength of the coupling observed between the electron and

hole amidst the screening effect exhibited by the background material matrices which include, respectively, ionic solids, covalent solids, and organic molecular crystals.[10] Mott-Wannier excitons (also known as just Wannier excitons) are typically found in inorganic semiconductors with low effective masses and high dielectric constants, which result in binding energies smaller than thermal energy ($kT$ ~ 26 meV) at room temperature.[11-13] Frenkel excitons are found in organic dye aggregates, conjugated polymers and molecular crystals wherein the low dielectric constant and high effective mass result in large binding energies of 0.2-1.2 eV.[11] Based on the spin-states of the bound electron and hole constituting the exciton, Frenkel excitons can be classified into short lived but fast diffusing singlet excitons, and long lived but slow diffusing triplet excitons.[14] Charge transfer (CT) excitons are a special type of Frenkel exciton wherein the electron and hole are found in different materials on opposite sides of a heterojunction interface and are yet bound coulombically. CT excitons are typically more delocalized than conventional Frenkel excitons and have low oscillator strengths. Wannier excitons are delocalized over tens to hundreds of atoms and are therefore characterized by large Bohr radii while Frenkel excitons are highly localized and the effective separation between the bound electron and hole (~ 1 nm), typically does not exceed 1-2 unit cells.[15] While Wannier excitons have a weaker oscillator strength compared to Frenkel excitons, their large size enables them to interact at much lower population densities and enables a plethora of nonlinear and other effects arising from many body interactions.[16] On the other hand, the large oscillator strength of conventional Frenkel excitons enables them to leave huge signatures in the optical absorption and emission spectra.[17] 2D semiconductors, particularly monolayers of transition metal dichalcogenides (TMCDs), exhibit an unusual type of Wannier exciton that is delocalized over several unit cells in the two-

dimensional sheet but is nevertheless coulombically bound with high exciton binding energies of the order of 0.5 V.[18]

Surface plasmons (or commonly just plasmons), are the collective and coherent oscillations of delocalized electrons that are excited by incident photons at a metal-dielectric interface.[19] The electric field component of the incident light is responsible for the excitation of the collective oscillations of these free electrons. These oscillations are commonly categorized into two modes, Surface Plasmon Polaritons (SPPs) and Localized Surface Plasmon Resonance (LSPRs), depending on the morphology of the metallic structure that enables them (Fig. 2).[20] SPPs are excited on continuous metal structures of characteristic dimensions larger than the wavelength of incident light; these plasmonic oscillations travel along the metal surface for distances of tens to hundreds of micrometers.[21] LSPRs are excited in metal nanostructures that are smaller than the electron mean free path, within the material, as well as the incident wavelength of light.[20] A resonance is achieved when the frequency of the free electron oscillations match that of the electric field component of the incident light. Unlike SPPs, LSPRs are non-propagating in nature, are strictly confined to the metal nanostructure, and can be excited on metal nanoparticles as well as around nanoholes or gaps in thin metal films.[22]

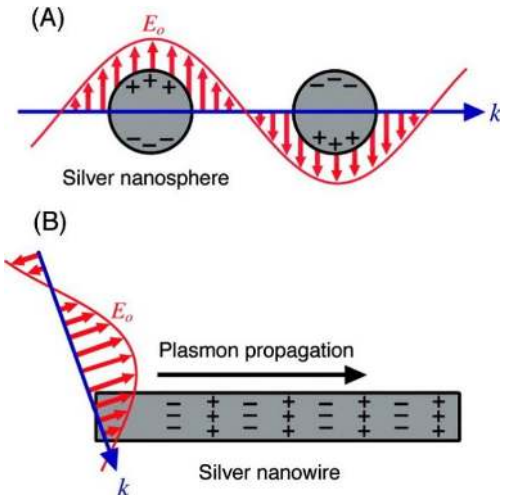

**Fig. 2 Plasmonic Modes.** Schematic illustrations of the two modes of plasmons evident in metallic nanostructures, (A) Surface Plasmon Polaritons (SPPs) and (B) Localized Surface Plasmon Resonances (LSPRs), depending on the morphologies that enable them. LSPRs are excited on metal nanostructures of characteristic dimensions smaller than the electron mean free path within the material as well as the wavelength of incident light (with an electric field of $E_0$ with wavevector $k$) like the nanospheres in (A) where delocalized electrons are displaced from the positive ions, their collective oscillations in resonance with the incident light. In (B) the nanowire's larger characteristic dimension compared to that of the wavelength of incident light results in excitation of a propagating mode of plasmons or SPPs traveling along the metal nanostructure's surface. The resonant interaction between the metallic nanostructure and the incident light is the main factor behind the two plasmon modes leading to the confinement of light energy to the surface of the nanostructure over time-scales exceeding that photons would generally spend in the same volume traveling at the speed of light.[23] Reprinted with permission from Ref[24]. Copyright American Chemical Society (2011).

Plexcitons, or plasmon-excitons, are characterized by the nature of coupling between the constituent excitons and plasmons. Molecular crystal excitons can be combined with the collective excitations of electrons within metals to create plexcitons. Most commonly, plexcitons are observed when an organic molecular layer is conjoined with a metallic film at an interface. A classic example of such a molecular plexcitonic system consists of J-aggregates of dye molecules on the surface of plasmonic nanostructures such as gold nanoshells or corrugated silver films or silver nanoprisms or a lithographically patterned array of Ag or Au nanodisks.[8, 25-27] Plexcitons can also result from the interaction of Mott-Wannier excitons with surface plasmons. Examples of such all-inorganic plexcitonic systems include chalcogenide nanorods coated with gold tips,[28] isolated nanoparticles or arrays of silver nanodisks on top of a 2D excitonic semiconductor such as $MoS_2$ or $WSe_2$ or $WS_2$,[29-31] layer-by-layer assembled quantum dot solids integrated with noble metal nanoparticles at tailored spacings[32] etc. Plexcitons offer an appealing platform for

exploring exotic phases of matter at nanoscale interfaces, as well as their potential application in controlling nanoscale energy flow. The examples of plexcitonic systems mentioned above also illustrate the importance of materials chemistry in engineering excitonic emitters in close proximity to noble metallic nanostructures or in placing excitonic materials in the gaps between coupled noble metal nanoparticles.

## 3. Principles of Plexcitonics

The principles of interaction in plexciton coupling and the subsequent conversion process of plasmon-exciton-photon modes have been widely investigated.[8, 32-35] The classical description of light-matter hybrids follow an approach where Maxwell's equations are utilized to define the position-local dielectric response of the system, $\varepsilon(\omega)$.[3] The dielectric response refers to the analysis of the storage and dissipation i.e. the interaction of electric and magnetic fields in a given material.[36] This parameter is experimentally accessible for many systems, via methods such as dielectric spectroscopy, impedance spectroscopy, and ellipsometry.[37, 38] Plexciton coupling refers to the collective interaction of metal plasmons and molecular excitons, and can be categorized into two modes: strong coupling, and weak coupling. But first, to understand the physical principles that dictate plexciton dynamics, it is necessary to review the models used to describe the constituent metal plasmons and molecular excitons.

### 3.1 The Metal Plasmon System

For metals, the Drude model provides the simplest description of the dielectric response,[39, 40] where the conducting electrons of a metal are considered as an ideal gas of non-interacting charged particles governed by Newton's second law along with a phenomenological friction term.[41, 42] The dielectric response function is written in the form, $\epsilon_r(\omega) = \epsilon_{r,\infty} - \frac{\omega_p}{\omega(\omega - i\gamma)}$. $\omega_p$ is

the plasma frequency, $\omega_p = \frac{n_e e^2}{(\epsilon_0 m_e)} \approx 10^{16} s^{-1}$, where $m_e$ and $n_e$ are the electron mass and electron density, respectively, and $\epsilon_{r,\infty} = \frac{\epsilon}{\epsilon_0}$ describes high frequency contributions from atomic core electrons. The corresponding dispersion relation, $k = \frac{\omega}{c}\sqrt{\epsilon_{r,\infty} - \frac{\omega_p^2}{\omega^2}}$, is found when the Drude model is applied to light propagation in homogeneous bulk metals. Accordingly, the creation of hybrid plasmon modes are indicated as the strong or resonant coupling between light and plasma charge oscillations in the metal when $\omega \to \omega_p$.

The Drude model is limited in its provision of describing the optical response of metals for only a short range of frequencies.[3] Apart from the Drude model, the Lorentz-Drude model provides an even more general description of the optical response of metals by combining the Drude model with the Lorentz function.[3, 43] An additional phenomenological term representing the effect of interband transitions and the motion of ionic cores is included. Combining the Lorentz-Drude model with Maxwell's equations, mathematical relations for the various behaviors observed along the interfaces of various dielectrics, such as an organic molecular layer and a metallic thin film, can be modeled.

In utilizing these relations to describe the general collective optical response of metallic nanostructures or the excitation of SPPs and LSPRs, one must not forget, as mentioned earlier, the significant influence that the geometry and characteristic dimension of the nanostructure impose on the construction of its mathematical model.

### 3.2 The Molecular Exciton System

For the sake of simplicity, the molecule is often modeled as a polarizable point object.[3] In this limit, a molecule's effect on a plasmonic system is largely relegated to the influence a molecule's proximity to a metal surface has on the local electromagnetic field. This local field describes the

response of the metal system to the electromagnetic field of the molecule as well as the originally incident radiation.[44] This simplistic model is efficient in providing qualitative, and at times quantitative, descriptions of various phenomena including the electromagnetic theory of surface enhanced Raman scattering.[45, 46] Nevertheless, the modeling of a molecule as a point dipole is a significant constraint, and is largely ineffective in describing realistic molecular-plasmon systems,[47, 48] where the molecular system is not a single molecule but an assembly of atoms or molecules, a molecular aggregate or semi-crystalline film, adsorbed on a metal surface.[8, 49-51] Additionally, the classical approach of utilizing a local dielectric function to describe the dielectric response of small particles has also been found to be inadequate.[52, 53] At the opposite extreme, for large particle sizes, and molecular distances the electrostatic approximation notably breaks down.[3] This leads to the consideration of the collective response of the molecular exciton-metallic plasmon system.

### 3.3 The Molecular Exciton-Metallic Plasmon System

An ideal theory must account for two major attributes in a realistic molecular-plasmon system: (i) the considerable effect the molecular subsystem may have on the plasmonic response of the metal and (ii) the response of the molecular assembly itself and the role it may play in the ensuing dynamics of the ensemble system.[3] Such a theory must also allow an approach where the optical behavior of the collective system is self-consistent with the molecular and metal sub-systems.

Dicke et al.[54] offered one such alternative in a theory where the molecule is modeled as a 2-level system; a molecular assembly, an assembly of two-level atoms. Dicke et al.[54] were able to demonstrate that such a system, consisting of a cluster of two-level atomic emitters, can result in super-radiant modes or super-fluorescence, and weakly-radiant modes depending on the

strength of the coupling to the incident radiation field. In the years following Dicke's contributions, further experiments focused on the integration of such molecular clusters of emitters with a plasmon-sustaining interface. This subsequently brought to observation the modifications of standard molecular optical properties, such as absorption, emission, and carrier lifetimes[55, 56] in plasmon-induced enhancement of energy transfer between the emitters.[57-61] Building on the premise of Dicke's work, all phenomena associated with plexciton coupling such as enhanced emission and exciton transport were discovered to be analogous to systems of excited molecules and molecular assemblies, optical modes of localized microcavities, structures where the radiation field is confined by reflecting faces on two sides of a spacer layer or optical medium,[3] as well as other nanostructures such as photonic crystals, where the coupling between the molecule and incident radiation field is intrinsically dependent on the geometrical characteristics of the system.[62-64] Consequently, the molecular system was noted to highly influence the plasmonic response of the metal, as well as that of itself, along with the corresponding charge transfer dynamics and dephasing mechanisms that may occur in the ensemble. This theory of interaction between molecules and plasmonic metal surfaces has been recently redefined in terms of two modes of coupling identified to occur at the interface of molecular exciton-metal plasmon structures: strong and weak coupling (Fig. 3).[56, 65] In this new framework, the resonant response of the system's coupling to the incident radiation field is dominated by the plasmon-exciton coupling that occurs at the interface, which can be super-radiant or strong, or sub-radiant or weak in nature.[66, 67] Strong coupling and weak coupling essentially describe the integration strength of the individual sub-systems, the molecular excitons and the metal plasmons, in a plexcitonic complex.

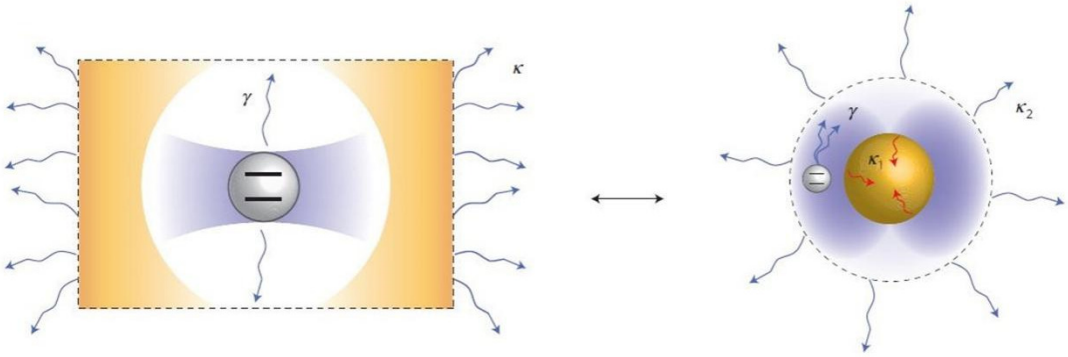


**Fig. 3 Weak and Strong Coupling.** Plexcitonic modes of coupling are analogous to those evidenced in systems of optical cavities (Left) governed by cavity quantum electrodynamics (CQED),[68] where the two regimes of Strong and Weak coupling are defined by the comparison of *g*, the energy transfer rate between light and matter and the subsequent sources of damping of the emitter and the cavity ($\gamma$ and $\kappa$). Strong and weak coupling are said to occur when $g >> \gamma, \kappa$ and g << $\gamma, \kappa$ respectively. The CQED description of modes in an optical cavity is very similar to what happens in a realistic plexciton complex (Right) where coupling occurs between the LSPR mode supported by a metal nanoparticle and a nearby atomic emitter. Here too, the comparative dependence of *g*, $\gamma$, and $\kappa$ define the coupling strength of the system. The principal difference between the two systems though is their dissipation channels. The optical cavity loses photons via transmission through its sidewalls, while the LSPR mode is damped through radiative losses and a myriad other interaction processes such as electron-electron bulk scattering and electron surface collision damping in the metal nanoparticle.[69] Reprinted with permission from Ref[70]. Copyright Nature Publishing Group (2013).

Strong coupling is the resonance hybridization of the material and optical modes resulting in a hybrid state that comprises both,[71] typically concomitant with a Fano resonance,[72] and is defined by three parameters: *g,* the energy transfer rate between light and matter, $\kappa$, the escape rate of light from the system, and $\gamma$, the polarization loss rate of matter. Strong coupling occurs when the rate of energy transfer between light and matter, *g*, is greater than that of $\kappa$ and $\gamma$. [73] The strong interaction between light and matter creates a hybrid light-matter state with

significantly different energy levels from the individual material and optical systems involved. An asymmetric Fano resonance typically accompanies this light-matter coupling.[74] Polaritons are quasiparticles that emerge as a consequence of strong light-matter coupling. As a hybrid entity, polaritons offer the possibility to shape the chemical and material properties of matter.

The strong coupling of plasmon-exciton modes is often introduced in optical microcavities. The intersystem coupling between matter and the microcavity is described as equivalent to two coupled classical harmonic oscillators.[75] This results in two independent modes of resonance frequencies that serve as distinct signatures of strong coupling at rate *g* when matter and the microcavity resonate, and can be identified from reflectance and transmittance spectra. The resonance frequencies are expressed as $\omega_{\text{exciton}} = \omega_{\text{microcavity}} = \omega_0 \pm g$.[5] It is important to note that when strong coupling occurs, the emitter that is identified is not just an eigenstate of the system but corresponds to a superposition of high energy and low energy polaritons, of different frequencies, and leading to coherent oscillations that characterize the excitation of the emitter and the cavity mode.[74] In the classical approach to science, systems are largely analyzed on the basis of their components, where the identification of these components is made on the basis that their individual properties are invariant when they are isolated. When these components are combined, their properties change, and as such new ones emerge from the composite system. The global properties of the composite system are then described by how the "mixing" has occurred between its constituents and their coupling. Quantum mechanics challenges this very notion. If the quantum state of a system can be defined precisely, the same cannot be said about the state of its constituents. This is the fundamental notion of entanglement, and it is very much applicable in what has been considered thus far in our study of light-matter coupling. For

example, while fluorescence as a process is usually associated with matter, it is also linked to the electromagnetic fluctuations in the quantum vacuum.[74, 76]

The splitting of the microcavity transmission peak into a pair of resolvable peaks is referred to as vacuum Rabi splitting, and is a characteristic of this quantum entanglement observed close to resonance where the normal mode frequencies of the coupled matter-microcavity system induce an avoided crossing or an energy level repulsion between the low and high energy states corresponding to the two resonance frequencies. The Rabi splitting energy provides a metric of the coupling strength and the coherent energy exchange between plasmons and excitons, while the depth of a Fano resonance indicates the efficiency of the energy transfer from plasmons to molecular excitons in the hybrid structure.[8, 77, 78] Even more subtly, Rabi splitting can be considered as a phenomenon that directly follows from the laws of quantum mechanics, in particular Fermi's rule, which shows that the spontaneous emission rate depends on the density of states (DOS) of the coupled electromagnetic modes. When there is a change in this DOS, there is a subsequent increase or reduction in spontaneous emission. This is indeed what is known as the Purcell effect,[79, 80] which when applied to the system of an optical microcavity essentially states that the environment molds the properties of the atom trapped in the cavity and vice versa. In other words, the fluorescence of a quantum emitter is modified inside a cavity and is such that the coupling of light and matter occurs even when there is no photon in the cavity, due to quantum fluctuations. The states of matter and the electromagnetic field are essentially coupled so much so that they cannot be defined independently as constituents of a whole. They are instead entangled (Fig. 4).[74] Weak coupling, the counterpart to strong coupling, is simply the regime where matter and the optical field can be considered separate entities that merely exchange energy.[74] Weak coupling is characterized by an increased

radiation rate, enhanced absorption cross-sections and energy exchange between excitons and plasmons.[5] The plasmonic enhancement of the local electromagnetic field in the vicinity of the excitonic material and Forster-type coulombic interactions are the primary mechanisms through which weak coupling occurs. The fundamental distinction between the two regimes is that while strong coupling displays characteristics similar to reversible spontaneous emission,[81] weak coupling has the characteristics of irreversible spontaneous emission.[5]

Together, strong and weak coupling highlight the modern approach towards understanding light-matter coupling from a quantum perspective. Strong light-matter coupling, in particular, has been of great interest due to its immediate potential in the fields of material science and chemistry for tuning the physical properties and chemical reactivities of molecules and materials.[74] In hindsight, the quantum nature of the coupling between the plasmons and excitons, an entanglement crucial to plexcitonics, is highly significant to our understanding of said coupled systems.[3, 5, 33, 70, 82, 83] Further understanding of the two coupling mechanisms, and their role in plexciton dynamics will be elicited by reviewing the assortment of nanophotonic applications where plexcitons play a key role.

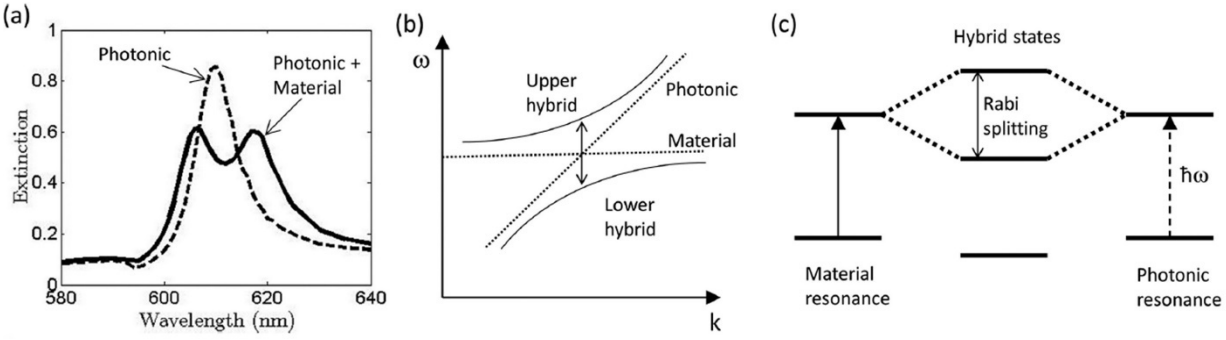


**Fig. 4 Plexcitonic Entanglement.** (a) The individual extinction spectra showing the photonic resonance of a plasmonic component (dashed) and the Rabi splitting (solid) that occurs when an excitonic material is introduced atop the plasmonic component (b) The coupling of these two quasi states of matter and light is

evidenced in the form of an avoided crossing where the separate modes (dotted) strongly shift as an evidence of strong coupling (c) As a result, in a plexcitonic system, the material resonance overlaps that of the photonic resonance leading to two hybrid states split by an energy difference which is the aforementioned Rabi splitting.[74] Reprinted from Ref[74] with attribution and adherence to Creative Commons Attribution License (CC BY) http://creativecommons.org/licenses/by/4.0/.

## 4. The Plasmonic Landscape

Plasmons and plexcitons are not standalone phenomena but are rather closely related, particularly from the perspective of how they manifest in diverse, yet similar, nanophotonic applications. To have a deeper appreciation of the advantages plexcitons provide over plasmons, it is necessary to consider what the current landscape in the field of plasmonics has to offer.

As mentioned earlier, plasmons consist of two modes: SPPs and LSPRs depending on the morphology of the metallic structure that enables them. SPPs are propagating in nature while LSPRs are non-propagating and strictly confined to the metal nanostructure. Plasmonic systems capitalize on the resonant interaction of light, manifested in these two modes, with the collective and coherent motion of electrons in metal nanostructures to allow for diverse abilities such as the ability to focus light into small volumes, perform chemical reactions, and fabricate nanostructures to name a few. A brief review of characteristic applications illustrating said abilities will now be presented and will serve to be complementary to the plexcitonic counterparts discussed later in this review.

### 4.1 Plasmonic Nanolithography

The fabrication of nanoscale devices is a fundamental element towards realizing nanophotonic applications. Photolithography is one such classical and widely used fabrication technique, and in the optical near field, used for the fabrication of features beyond the diffraction limit.

Demonstrative examples include contact imaging through a transmission mask or a binary phase-shift mask,[84, 85] evanescent near field lithography with an embedded-amplitude mask,[86] light coupling masks,[87] and evanescent interferometric lithography.[88]

Luo et al.[89] demonstrate a unique nanofabrication method, that can provide for pattern fabrication beyond the diffraction limit, but by employing surface plasmon polaritons. The proposed surface plasmon resonant interference nanolithography technique (SPRINT) is shown to produce sub-half-wavelength structures of high efficiency using monochromatic illumination of a standard photoresist with UV or visible light. The working principle of the technique involves employing a periodic corrugation material such as a prism to couple the incident light with a surface plasmon upon the metallic surface and subsequently obtain propagating surface plasmon polaritons (SPP) of high electric field intensities and shorter wavelengths. Subsequent interference of the SPP "waves" within the corrugated material results in an enhancement of the spatial distribution of the electric field near the metal surface. The thin layer of resist directly below the mask soon finds itself with increased exposure to the incident light when the resonance frequency of the SPP falls within the sensitivity range of the photoresist layer thanks to the enhanced optical field close to the metal surface. A schematic representation of the SPRINT process is shown in (Fig. 5). Here, a silver mask is fabricated upon a thin layer of quartz with a thickness of 2 mm using electron beam lithography and liftoff. The mask is illuminated from the top side with the light tunneling through via SPP and reradiating onto the photoresist on the opposite side. Conventionally, the set up so far by Luo et al.[89] is similar to a diffraction limited exposure but thanks to the resonant excitation of the SPP waves on the metallic surfaces, as mentioned earlier, this limit can be alleviated.

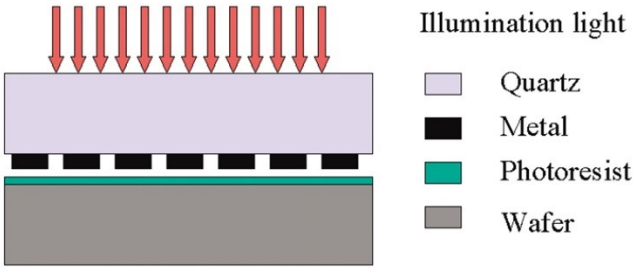


**Fig. 5 SPRINT.** Schematic representation of the surface plasmon resonant interference nanolithography system. Reprinted with permission from Ref.[89] Copyright AIP Publishing (2004).

Quantitative and qualitative support of the technique's feasibility is explored by Luo et al.[89] using numerical FDTD simulations, as well as experimental replication showing that high resolution features of 50 nm can be readily created when using SPP interference in the optical near field, on metallic masks, with an excitation wavelength of 436 nm corresponding to the mercury g-line. Arbitrary patterning, as per the need, is proposed for the unperforated metallic mask with corrugated surfaces on both sides. It is the corrugated surface of the metallic mask on the illuminated side that collects light via SPP coupling, while redistributing the light into nanoscale spatial distributions on the exit side and which can subsequently be used to fabricate nanostructures. FDTD calculations are used to demonstrate that the SPP excitations resulting in the enhancement of the near-field distributions are highly localized around the metal/dielectric interface. The observation of interference of the SPP fields proves that the metallic patterns utilized on the mask act as field redistributors with areas of vacant holes experiencing rapid decays in the field, while those in areas of the metal parts dominate the far-field emission. The transmitted light presents both evanescent and nonevanescent components (Fig. 6). In fact, the feature sizes that are obtained using SPRINT are seen comparable to those involving nanoimprints from a non-photobased method.[90] Furthermore, since SPRINT is not limited by

diffraction, even smaller structures are demonstrated to be produced with large illumination wavelengths.

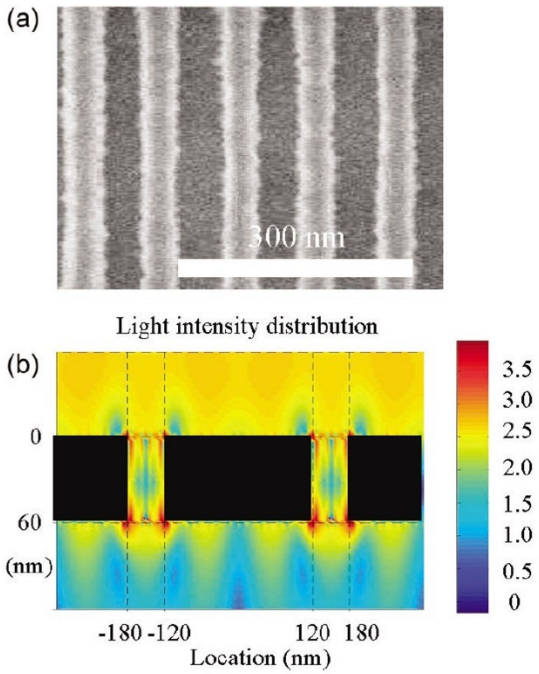


**Fig. 6 Numerical and experimental investigations of SPRINT.** (a) SEM image of nanolithographic features procured via SPRINT. (b) FDTD simulation of the near field. Reprinted with permission from Ref.[89] Copyright AIP Publishing (2004).

In conclusion, Luo et al.[89] have demonstrated that nanofabrication beyond the diffraction limit can be achieved via near-field exposure using a metallic pattern through SPP excitation. By changing selective parameters of the mask, the near-field pattern can be optimized to generate features of the smallest lateral dimension. Aside from the technique's novelty, Luo et al.[89] have shown SPRINT satisfies many of the requirements of single-step lithographic applications, especially from the economic approach it provides towards fabricating high-resolution, high-density optical lithography for various areas of research and technology. Nonetheless, it remains an open question on how SPRINT can be adapted to the more complicated needs of electronic device fabrication involving multiple successive alignment of features.

### 4.2 Plasmonic Optical Recording

The nature of light-matter interactions in plasmons also promotes a variety of applications in optical communications, and information processing. One such potential application is discussed by Zijlstra et al.[91] in their investigations of five-dimensional optical recording, for high density optical data storage, mediated by surface plasmons in gold nanorods. In general terms, multiplexed optical data storage systems utilize polarized light to increase the storage capacities of optical storage mediums such as optical disc drives used to often read or write data to or from compact discs, DVDs, Blu-ray discs etc. Multiplexed optical recording is of great importance as it helps increase the information density beyond $10^{12}$ bits/cm$^3$ by storing multiple, and yet individually accessible patterns within the same recording volume. However, the lack of a suitable recording medium that can provide for high optical data storage as well as selectivity in the domains of wavelength and polarization as well as the three spatial domains, resulting in orthogonality in all five-dimensions has been a major obstacle.[91] Furthermore, while extensive research has been achieved in exploiting wavelength,[92, 93] polarization,[94, 95] and spatial dimension[96, 97] dependent approaches for multiplexing, never have they been assimilated into a single approach that could ultimately increase the information storage capacity by orders of magnitude.

A successful five-dimensional encoding would require a recording material that is orthogonal in all dimensions, provides multiple recording channels in each dimension, and is stable in ambient conditions. Zijlstra et al.[91] succeed in satisfying all three criteria by devising a system that exploits the properties of the longitudinal surface plasmon resonance of gold nanorods. Plasmonic gold nanorods have been utilized in a wide range of applications due to their unique optical and photothermal properties. These properties are exploited to great effect by

Zijlstra et al.[91] who take the narrow longitudinal surface plasmon resonance linewidth of a gold nanorod (100-150 meV, 45-65 nm in the near infrared), and combine it with its dipolar optical response as a means to achieve selective longitudinal SPR mediated recording and readout that can be controlled by photothermal reshaping and two-photon luminescence detection, respectively (Fig. 7).

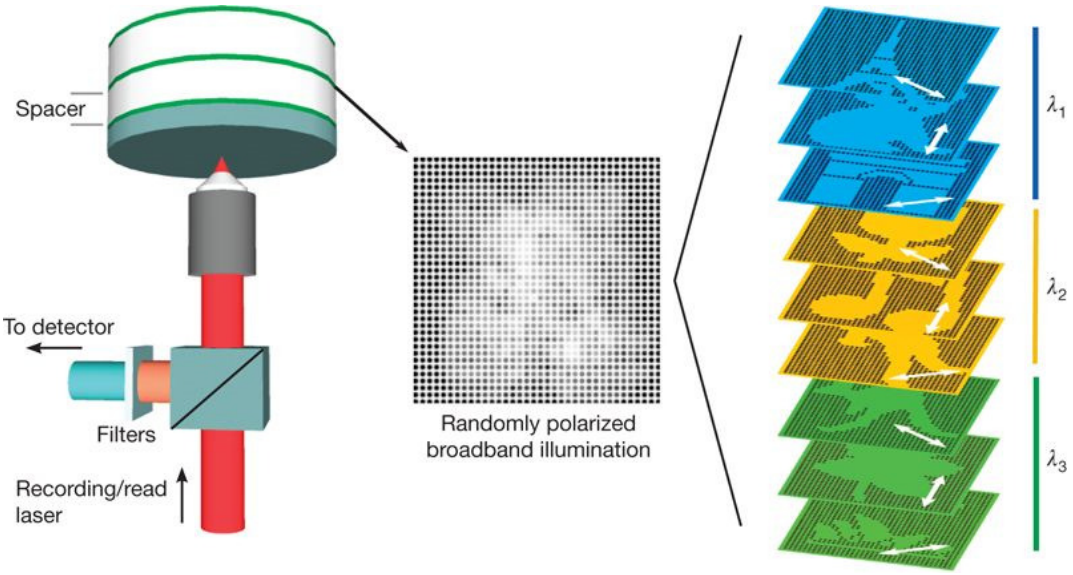


**Fig. 7 Plasmonic Optical Recorder Device Schematic.** (Left) The plasmonic optical recorder fabricated by Zjilstra et al.[91] is a device where the sample is made of thin recording layers of polyvinyl alcohol (spin-coated) doped with gold nanorods on a glass substrate. The consecutive layers are spaced by a transparent pressure-sensitive adhesive of thickness 10 mm. It is upon these recording layers that various images are patterned using different wavelengths and polarizations of the recording laser. (Middle) By illuminating the records with unpolarized broadband illumination, a convolution of all the pattered images are observed on the detector with filters barring any reflected laser light from the readout. (Right) With the right selection of polarization and wavelength, individual patterns that were printed upon the records can be read individually without any crosstalk. In this manner, Zjilstra et al.[91] propose a plasmonic optical recorder advice that assimilates wavelength, polarization, and spatial dimension selectivity in its approach towards multiplexing and high density optical data storage. Reprinted with permission from Ref.[91] Copyright Springer Nature (2009).

The longitudinal SPR provides for wavelength and polarization sensitivity, while axial selectivity is provided by the energy thresholds required for the photothermal recording mechanism (Fig. 8). Longitudinal SPR-mediated two-photon luminescence, due to its enhanced wavelength and angular selectivity, is then used to detect the recordings and demonstrating a definitive improvement compared conventional linear detection mechanisms. Despite their immediate use of a femtosecond pulse laser for patterning, Zijlstra et al.[91] demonstrate that the recordings can also be performed with low-cost recording apparatus such as a continuous wave laser or laser diode.

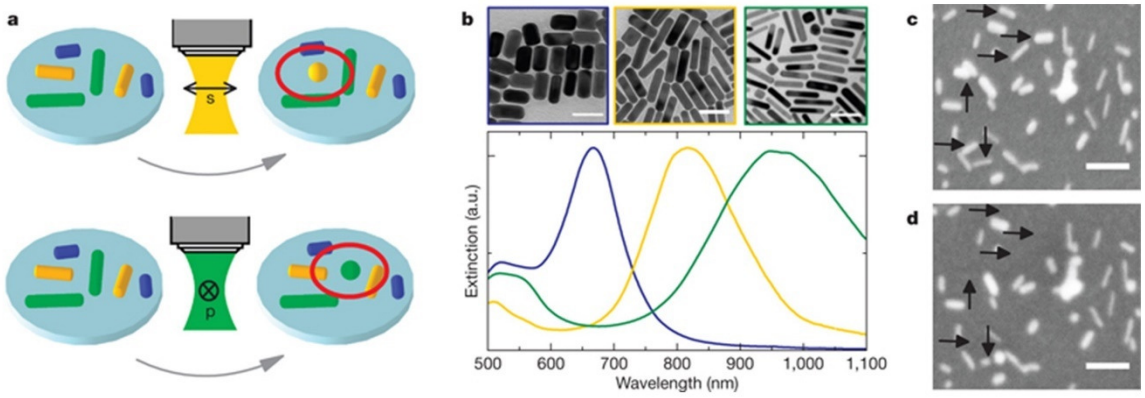


**Fig. 8 Photothermal Patterning.** (a) Photothermal reshaping of the gold nanorods is used to define the patterning mechanism of the plasmonic optical recorder, and sets the stage for selectivity in wavelength, spatial dimension, and polarization.[91] Gold nanorods in the focal volume of the objective are selectively reshaped with differing aspect ratios and orientations, as a consequence of which, varying modes of SPRs are excited upon the metallic structures. Only gold nanorods aligned along the polarization of the laser light and which exhibit an absorption cross-section that matches the incident laser wavelength absorb the incident light pulse. This is illustrated in (Top) where incident light that is s-polarized only shapes the nanorods with an intermediate aspect ratio aligned to the laser polarization while (Bottom) p-polarized light reshapes only those gold nanorods with high aspect ratios aligned to the laser polarization. (b) Normalized extinction spectra of the gold nanorod solutions that were utilized. (Insets) Transmission

electron micrographs of the gold nanorods on a copper grid. The average sizes of the nanorods utilized (from Left to Right) are 37 x 19 nm (aspect ratio of 2 $\pm$ 1), 50 x 12 nm (4.2 $\pm$ 1), and 50 x 8 nm (6 $\pm$ 2). Scale bars correspond to 50 nm. Zijlstra et al.[91] utilize these nanorods where each recording layers in the multi-layered sample is doped with mixtures of said assemblies to form an in-homogeneously broad extinction spectrum profile. (c)-(d) The corresponding SEM images of the gold nanorods spin-coated on an indium tin oxide coated glass substrate before (c) and after (d) irradiation with a single femtosecond laser pulse of 840 nm with horizontal polarization. The nanorods affected by the laser pulse are indicated with arrows, and the scale bars correspond to 100 nm. In this manner, images are patterned onto the multiple record layers. Reprinted with permission from Ref.[91] Copyright Springer Nature (2009).

As a result, Zijlstra et al.[91] patent a technique that enables non-destructive, crosstalk-free readout and that can be applied with high effectiveness for optical patterning, encryption, and data storage applications where higher data densities are of great importance. Their presented technique proves to have great potential for improving security imprinting and encryption via the addition of extra dimensions that can act as extended counterfeit-proof encryption keys while foregoing the need for raster scanning, and most importantly, by incorporating two polarization and three wavelength channels in their patterning procedure, is beneficial for high density optical data storage (Fig. 9).

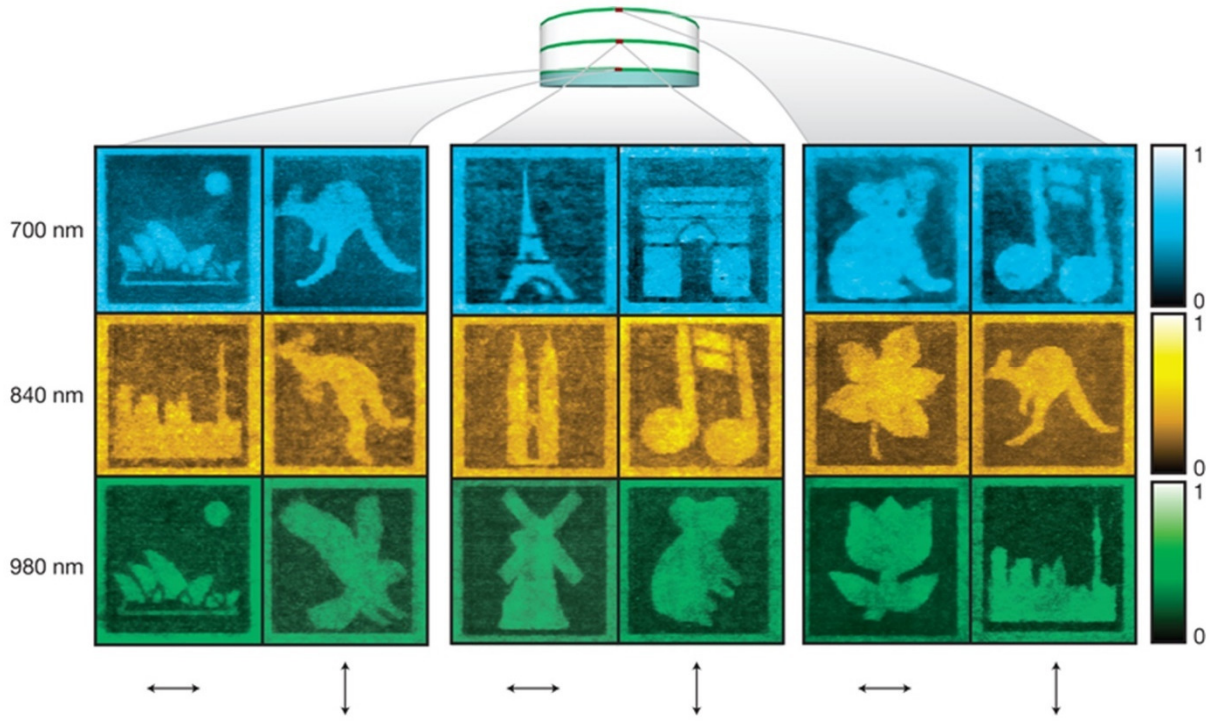


**Fig. 9 High-density Optical Storage.** With five-dimensional patterning and readout, the technique presented by Zjilstra et al.[91] is highly beneficial for high density optical storage. As demonstrated, we have here normalized two-photon luminescence raster scans of 18 patterns all encoded within the same area using two polarizations of laser light, and three different wavelengths. The patterns are recorded in three layers each spaced from the other by 10 mm. By detecting the excited two photon luminescence with the same wavelength and polarization the recordings can then be retrieved. The sizes of all the images patterned as such are 100 x 100 μm and the patterns are 75 x 75 pixels. The bit spacing used equals the bit diameter of 0.75 μm which is equivalent to a bit density of 1.1 Tbit $cm^{-3}$ resulting in a high-density disk capacity of 1.6 Tbyte for a DVD sized disk. Reprinted with permission from Ref.[91] Copyright Springer Nature (2009).

### 4.3 Plasmonic Photocatalysis

Photocatalysis addresses the use of light to activate a substance that modifies the rate of a chemical reaction without being involved itself. Nature provides a direct example of this in the process of photosynthesis, where plants, algae, protists, and photosynthetic bacteria capture sunlight along with $CO_2$ in the atmosphere to promote water-splitting chemistry (Fig. 10).[98] Semiconductor photocatalysts constitute the most common artificial photosynthetic technology; $TiO_2$ is the benchmark photocatalyst which has been used to photoelectrochemically split water, photooxidize organic compounds in water and photoreduce $CO_2$ in the vapor phase.[99-104] Critical material-related limitations in semiconductor photocatalysts involving optimal band-gap energetics, light absorption, catalytic activity, stability, and sustainability have led to the development of a potential alternative in plasmonic photocatalysts.[20]

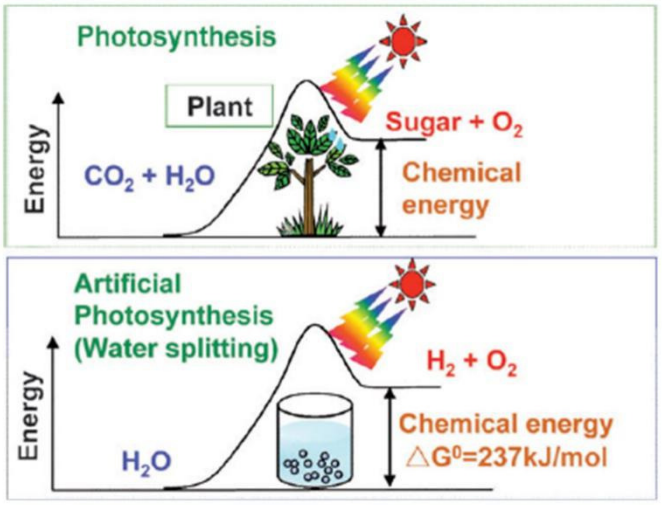


**Fig. 10 Artificial Photosynthesis.** In mimicking nature, artificial photosynthetic systems based on semiconductors utilize photocatalysis to provide for alternative energetic pathways and selectivity in desirable chemical reactions including: $CO_2$ photoreduction, water splitting, and the degradation of harmful organic pollutants. Reprinted with permission from Ref.[105] Copyright Royal Society of Chemistry (2009).

Plasmon-enhanced photocatalytic systems focus on taking advantage of "hot electrons", energetic charge carriers that appear due to a resonant interaction of light with the collective motion of electrons in metal nanostructures to enhance and support photocatalytic activity.[106] The injection efficiency of "hot electrons" in plasmonic systems (Fig. 11), such as plasmonic photo-detectors and plasmon-sensitized solar cells, has thus far been quite poor.[107] This is due to the short lifetime of hot electrons, ranging around 100-500 fs,[108] and subsequent damping processes involving electron-electron bulk scattering, radiative damping, electron-surface collisions, and electron-phonon collisions in plasmonic nanostructures.[109] Thus, improved injection efficiencies of hot electrons generated in plasmonic photocatalytic systems are highly desirable, and this goal is an active subject of research.

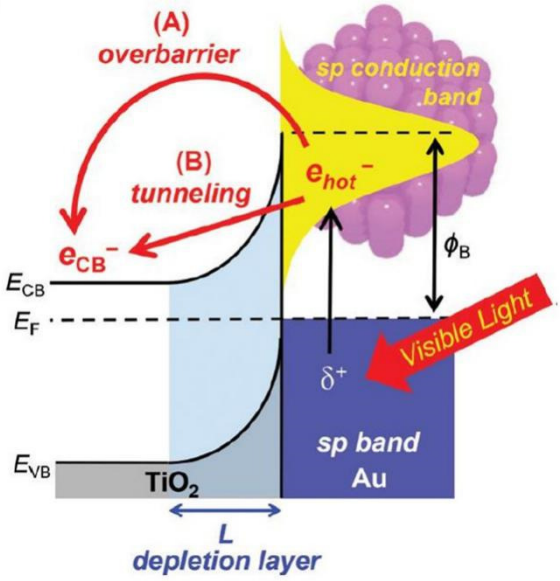


**Fig. 11 Plasmonic Photocatalysis.** Critical material-related limitations in semiconductor photocatalysts led to the development of an alternative in plasmonic photocatalysts. Despite their immense potential, plasmonic photocatalytic systems have largely been setback by poor injection efficiencies of energetic charge carriers resulting in low performance efficiencies. Reprinted with permission from Ref.[110] Copyright Royal Society of Chemistry (2017).

Various experiments have engaged the development of plasmon-enhanced photocatalytic systems that take advantage of high energy charge carriers or hot electrons. Au and Ag are the most common plasmonic noble metals utilized in plasmonic photocatalysis while $TiO_2$ has served as a benchmark material for semiconductor-mediated photocatalysis.[111, 112] $TiO_2$, apart from its environmental-friendly nature, is an inexpensive and easily accessible photocatalyst that has proven to be greatly effective in diverse scenarios.[102, 113] $TiO_2$ is a wide band gap (3.2 eV for anatase and 3.0 eV for the rutile phase) photocatalyst that absorbs primarily in the UV spectrum of light, where less than 5% of solar energy resides.[114] Considerable efforts have been made to extend the light absorption range of $TiO_2$ from UV to visible wavelengths, for example doping, though there has always been a negative feedback on the absorption coefficient and subsequent photocatalytic activity of the semiconductor.[115, 116] $TiO_2$ has been implemented as a photocatalyst in various structural forms: powders in an aqueous solution, nanoparticles (0D), nanorods (1D), nanosheets and films (2D), 0D-1D-2D integrated nanostructures (3D),[117] doped heterojunctions, varying crystalline phases (rutile, anatase, and brookite systems),[118] and mesoporous supports.[119-121] The focus in most of these efforts has been to optimize the optical path length, carrier mobility,[120] charge carrier kinetics,[122] light absorption,[121] band bending etc. Nonetheless, sustained success in expanding the photocatalytic potential of $TiO_2$, as a semiconductor, to visible wavelengths has not been achieved.[113] Plasmon enhanced photocatalytic systems, involving plasmonic noble metal-$TiO_2$ semiconductor heterojunctions, come into play here as by using the knowledge that Au and Ag have surface plasmon resonance in the visible spectrum of light, one can capitalize on the charge transfer of hot electrons to the neighboring $TiO_2$ semiconductor. The $TiO_2$ semiconductor can then serve as the location for photocatalytic reactions in addition to those on the surface of the noble metal.

Setting aside the immense expanse of research that has been done in optimizing semiconductor-mediated photocatalysis, the rise of plasmon-mediated photocatalytic systems as a new standard has been met with its fair share of research, focusing not only on understanding the inherent physical mechanism involved in hot charge carrier transfer but also in the optimization of said systems. Although the inherent mechanisms that govern hot electron charge transfer from the noble metal to the semiconductor is yet to be fully understood,[23, 69, 113] the potential of plasmonic photocatalysis has not been overlooked with many said experiments over the years involving hot electron harvesting systems consisting of a $TiO_2$-noble metal nanoparticle heterojunction for diverse applications including photocatalytic degradation/aerobic oxidation of organic compounds, photocatalytic $CO_2$ reduction and $H_2$ generation, and photoelectrochemical water splitting.[103, 105, 123-130,131]

## 5. Exploiting Plexcitons

The motivation to combine metal and semiconductor nanostructures is largely due to their complementary optical properties. Metal nanostructures promote the localization of electromagnetic modes, giving rise to high emission yields and light-harvesting capability, while semiconductor nanostructures support long-lived charge excitations that enable efficient trapping of electromagnetic energy and enhanced optical fields and nonlinearities.[132] Plexcitonics research follows efforts to analyze the nature of light-matter interactions at the nanoscale and exploit the collective and coherent motion of electrons and holes, via diverse modes, in exciton-metal plasmon nanostructures. This has allowed for the selective design and modification of absorption and emission properties,[65, 133] energy transfer between excitonic and plasmonic systems,[34, 134, 135] and the exploration of strong coupling through coherent plasmon-exciton interactions (Fig. 12).[136, 137]

The transfer of energy through optical near-field interactions is widely valued for the observation, detection, and measurement of minute separation distances in molecular systems and alike. Forster resonance energy transfer (FRET) is widely understood as the process where the energy of an excited molecule can be transferred, through non-radiative means, to a molecular of lower transition energy via dipole-dipole coupling.[138] As such, FRET pairs can be used as probes for cell-material interactions,[139] as molecular sensors,[140] to study the length and flexibility of polymers and biomolecules,[141] and to investigate dynamical biomolecular processes involving molecular interactions and protein folding processes.[142, 143] The energy transfer evidenced in FRET processes are characterized by the Forster radius $R_0$ defined as the separation distance at which the energy transfer efficiency is 50 %. As noted by Rodarte et al.[144], for a small change in separation distance, a correspondingly large change can be observed in the fluorescence spectrum (Fig. 12a). Therefore, FRET is primarily used as a spectroscopic ruler. Unfortunately, due to the dipole-dipole interaction reducing coupling efficiency by a factor of inverse sixth power of the distance between molecules ($R^{-6}$), FRET is effectively limited to function in separation ranges below 10 nm.

Rodarte et al.[144] explore a promising alternative in a plexcitonic ruler aggregate composed of plasmonic and organic fluorophore components. Plasmon rulers composed of noble metal nanoparticles, and their LSPRs provide strong scattering cross sections that allow the nanoparticles to be visible in a dark-field microscope. The additional caveat that metallic nanoparticles are not prone to blinking or bleaching makes them promising candidates for sensing applications. In a plasmon ruler, two metal nanoparticles are used to measure the separation distance. Capacitive coupling between the two nanoparticles results in a strong red-shift of the LSPR wavelength as shown in (Fig. 12b), the coupling strength being proportional to

$R^{-3}$ as opposed to $R^{-6}$ for FRET.[145] By combining the higher efficiencies of plasmon nanoparticle rulers with fluorescence tags commonly used in FRET pairs to label the relevant biomolecules being considered, a plexcitonic ruler complex is established.

Such a system can function between the two regimes of weak and strong coupling that characterize plexcitonic systems. The weak coupling scenario involves the case where the energy transfer between the fluorophore and the metal nanoparticle is observed as a quenching or enhancement of fluorescence depending on the separation distance from the surface of the nanoparticle (Fig. 12c).[146] Alternatively, the strong coupling scenario manifests as a Fano resonance observed as the asymmetric dip in absorbance at the exciton transition frequency together with Rabi splitting (Fig. 12d). In their studies, Rodarte et al.[144] exploit these mechanisms by demonstrating the dependence of separation distance on coupling strength between plasmons and exciton in a Ag nanoparticle and monomer dye conjugate. By showing that the coupling strength follows a single-exponential decay with a decay length of $13.7 \pm 5$ nm, Rodarte et al.[144] prove that such a conjugate system can be used as a spectroscopic ruler.

Similarly, another study by Ozel et al.[32] demonstrated the use of plexcitons to improve the rate of Förster-type resonance energy transfer in quantum dots. Layer-by-layer assembled CdTe quantum dots of two different sizes were interspersed with gold nanoparticles located at well-defined spacings that enabled the plasmon-exciton coupling to be selectively tuned to either the donor quantum dots (smaller size) or the acceptor quantum dots (larger size), which in turn has applications in fluorescence microscopy (Fig. 13).[32] Ozel et al.[32] are able to structurally control the plexcitonic interactions of the composite systems described by placing the plasmonic layers in proximity of the donor quantum dots (for strong donor plexciton coupling) while having them sufficiently far away from the acceptors (for weak acceptor plexciton coupling) and vice

versa. As such, Ozel et al.[32] identify a means to independently control the individual plexcitonic coupling to the donors and the acceptors in a cascaded energy transfer mechanism. The modification of the FRET mechanism via selective control on the plexcitonic energy transfer allows for the selective manipulation of the detection signal and sensitivity of the desired donor or acceptor species. This is of great importance for FRET-driven nanophotonic devices and FRET-based bioimaging applications. Set in context with the work of Rodarte et al.[144] involving FRET studies where the energy transfer is used as the molecular ruler, these results from Ozel et al.[32] provide a possible means to enhance the resolution of said molecular measurements due to the enhanced energy transfer rate via the donor or the acceptor species of interest.

Plexcitonic applications are categorized by the strength of plasmon-exciton coupling identified at the interface between the excitonic and metal nanostructures. In this review, we shall focus on many such applications varying between the regimes of strong and weak coupling, and highlight the current state of research in the field including plexcitonic photocatalysis, photovoltaics, and luminescence.

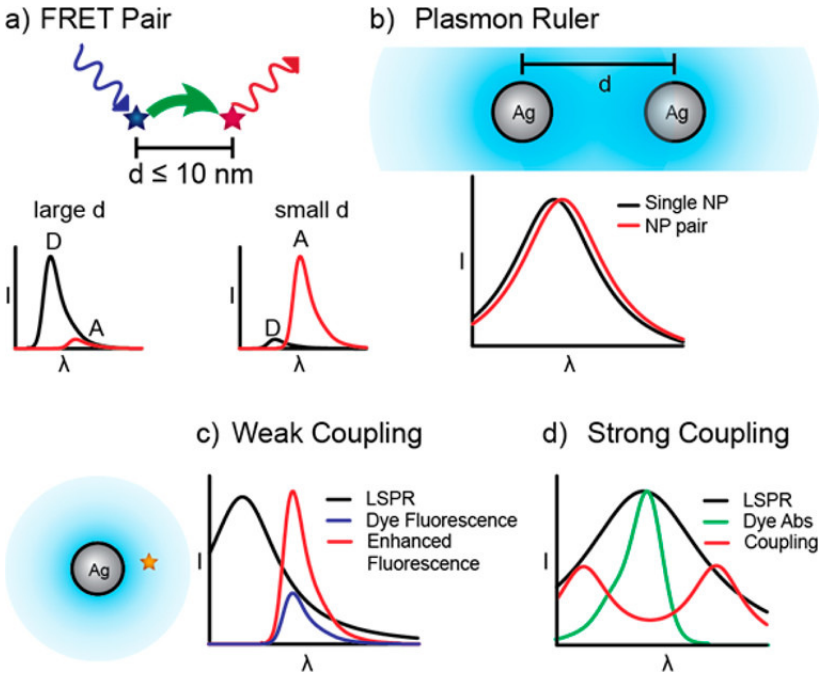

**Fig. 12 Energy transfer mechanisms.** Various energy transfer mechanisms encompass molecular, plasmon, and molecular-plasmon systems and are observed most commonly in their fluorescence spectral characteristics.[144] (a) Forster Resonance Energy Transfer,[138] a non-radiative form of energy transfer between two fluorophores where the donor molecule transfers energy to the acceptor molecule, for molecular distances less than or equal to 10 nm, increasing the acceptor fluorescence. (b) Plasmon coupling in a plasmon ruler containing an Ag nanoparticle pair, the close-spacing of the two nanoparticles resulting in a LSPR coupling that red-shifts the LSPR peak wavelength. (c) Weak coupling between an Ag nanoparticle and a nearby fluorophore that results in enhanced fluorescence of the coupled system, and (d) Strong coupling, resulting in the Rabi splitting of the coupled system. Reprinted with permission from Ref.[144] Copyright American Chemical Society (2017).

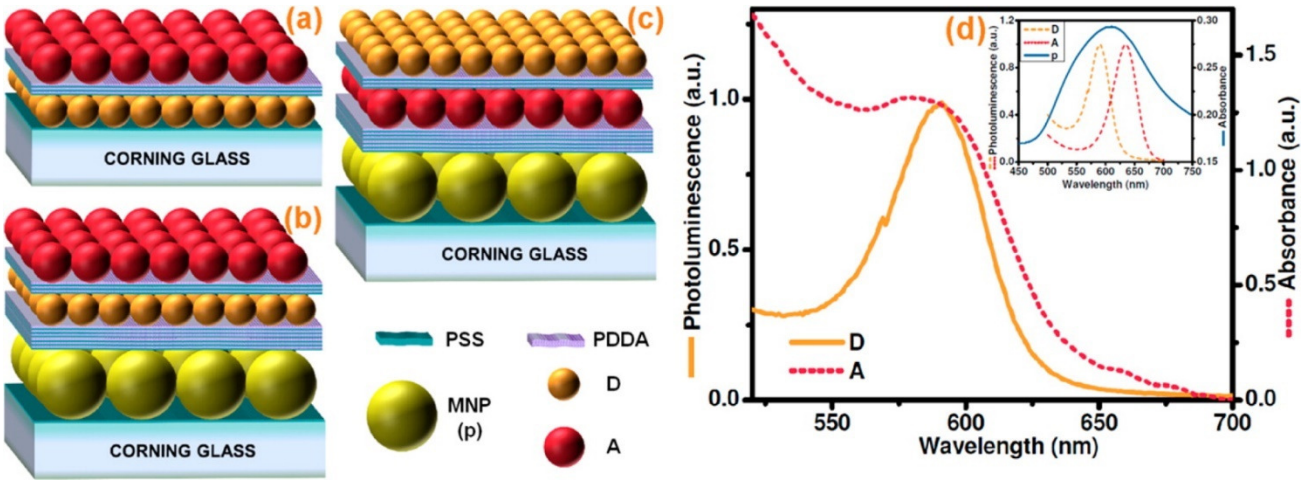


**Fig. 13 Quantum Dot-Metal nanoparticle FRET architectures.** Layered constructs of quantum dots and metal nanoparticles are utilized to demonstrate plasmonic and nonradiative energy transfer interactions via selective, and controlled generation of plexcitons at either the donor (D) and acceptor (A) quantum dot energy transfer pairs. The layered architectures vary from those utilized in conventional FRET (a), plasmon-mediated FRET (PM-FRET) where coupling occurs only to the donor quantum dots, and complementary PM-FRET where coupling occurs only to the acceptor quantum dots. (d) Photoluminescence spectrum of the donor quantum dots and the absorption spectrum of the acceptor quantum dots and the photoluminescence spectrum of the composite quantum-dot metal nanoparticle film (inset). Reprinted with permission from Ref.[32] Copyright American Chemical Society (2013).

### 5.1. Optimizing Plexcitonic Coupling

One promising method to tackle the problem of the low-yield of hot electrons is to consider hybrid systems of plasmonic metals and excitonic semiconductors (Fig. 14).[8, 72, 147-151] Such hybrid structures have provided for decreased bandgaps, adjusted densities of states (DOS), and prolonged lifetimes for hot electrons,[150] subsequently setting a new platform for the mediation of efficient surface catalytic reactions. The working principle of these composite nanomaterials is the strong coupling observed between the plasmons and excitons, which has been attributed to prolonging the lifetime of hot electrons and increasing reaction efficiencies.[72, 147, 150]

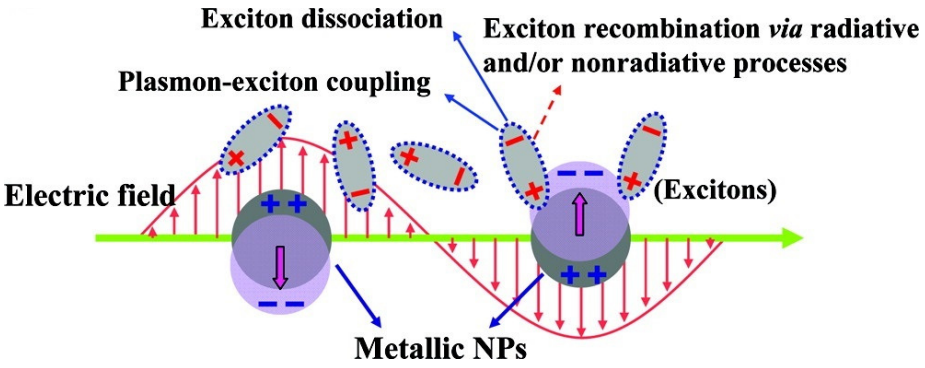


**Fig. 14 Plexcitonic Photocatalysis.** Plexciton sensitized photocatalytic systems are now setting the stage for improvements on both fronts by utilizing strong coupling in molecular exciton-metal plasmon systems to promote energetic charge-carrier or "hot excitons" at a metal-dielectric interface to enhance energetic charge-carrier lifetimes, and injection efficiencies. Reprinted with permission from Ref.[152] Copyright American Chemical Society (2011).

The analytical characterization of plexciton dynamics was addressed in the work of Fofang et al.[8] where the formation of nanoshell J-aggregate nanoparticle complexes are demonstrated to produce coherent coupling between the localized plasmons of the metallic nanoparticle and the excitons of the molecular J-aggregate. By varying the core size/shell thickness ratio of the Au nanoshells- plasmonic nanoparticles that consist of a spherical silica

core coated with a thin, uniform layer of Au-NPs, the plasmon energies of the nanoparticle can be modified and tuned to the excitonic energy of the molecular adsorbate, the J-aggregate.[153, 154] As such, the diverse multipolar plasmon modes and their coupling dynamics to the excitonic J-aggregate can be thoroughly explored. Fofang et al.[8] demonstrate this in a series of experiments where two Au nanoshell size ranges of radii 45 nm and 90 nm, corresponding to the dipolar and quadrupolar nanoshell plasmon mode resonances with the J-aggregate exciton line, are utilized to theoretically analyze the dynamics and strength of the plasmon-exciton coupling interaction in a quantitative manner (Fig. 15).

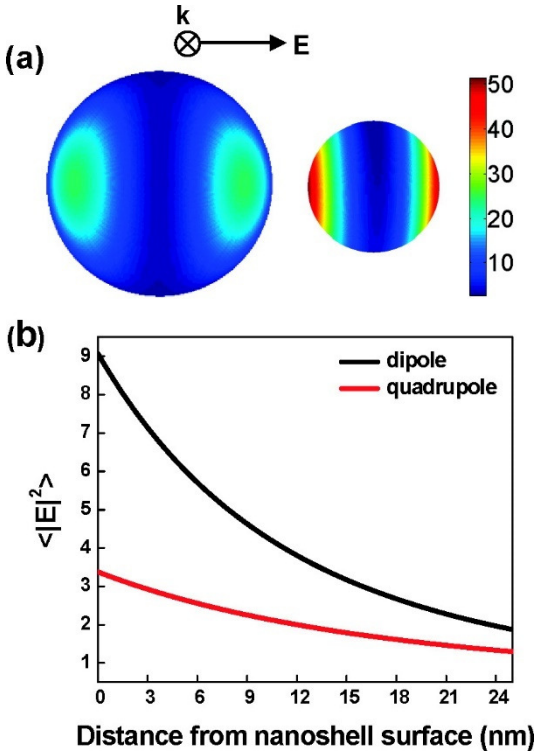


**Fig. 15 Multipolar Plasmon modes in Au nanoshells.** Fofang et al.[8] use two nanoshell size ranges (a) in their experiments, corresponding to the dipolar and quadrupolar nanoshell plasmon modes. The near field enhanced electromagnetic fields correspond to the 693 nm excitation wavelength with the $[r_1,r_2]$ = [45, 63] nm nanoshells displaying a dipolar field with greater intensity as opposed to the quadrupole field of the [90, 120] nm nanoshell. The near field properties of the structures are further explored in (b) where the variation of the surface average field intensity, $\langle|E|^2\rangle$, with distance from the nanoshell surface is

measured for the two nanoshell sizes. Reprinted with permission from Ref.[8] Copyright American Chemical Society (2008).

An optimal J-aggregate with high oscillator strengths and narrow transition line widths is formed from the dye 2,2'-dimethyl-8-phenyl-5,6,5',6'-dibenzothiacarbocyanine chloride, and provides for strong coupling at room temperature. UV-vis spectroscopy along with surface enhanced Raman scattering (SERS) measurements are performed to confirm the formation of the nanoshell-J-aggregate complex. By considering a concentric three-layer model of a two-layer spherical shell particle surrounded by a layer of J-aggregate, Fofang et al.[8] are able to describe the system theoretically (Fig. 16).

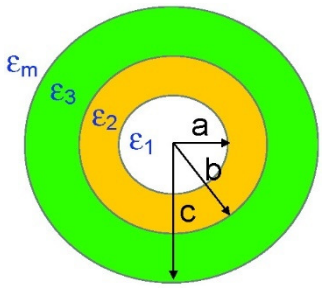


**Fig. 16 Gold Nanoshell-J-aggregate complex model.** Schematic of the gold nanoshell-J-aggregate complex model for the theoretical calculation. $\varepsilon_1$, $\varepsilon_2$, $\varepsilon_3$, and $\varepsilon_M$ represent the silica core, gold shell, J-aggregate molecule layer, and the surrounding medium, respectively. (a), (b), and (c) represent the core, nanoshell, and nanoshell-J-aggregate complex radii. Reprinted with permission from Ref.[8] Copyright American Chemical Society (2008).

Using Gans theory, a solution of Maxwell's equations for plane wave excitation of a spheroidal metallic nanoparticle within the quasi-static approximation, an analytical expression for the hybridized plasmon-exciton states of the system is derived. Subsequently, it is observed that the splitting energies of the plexciton complex are limited by the thickness of the excitonic J-aggregate layer on the nanoparticle surface with a nominal effective thickness value of 4 nm

(Fig. 17). By means of their results, Fofang et al.[8] show the inherent potential of coupled plasmon-exciton nanostructures with controlled coupling, and unique optical properties that can be harnessed with hybrid plexcitonic materials. Their work was further supplemented in a follow up report where time-resolved studies were utilized to analyze the same J-aggregate-Au nanoshell complexes and the inherent plexciton dynamics involved in said systems.[155]

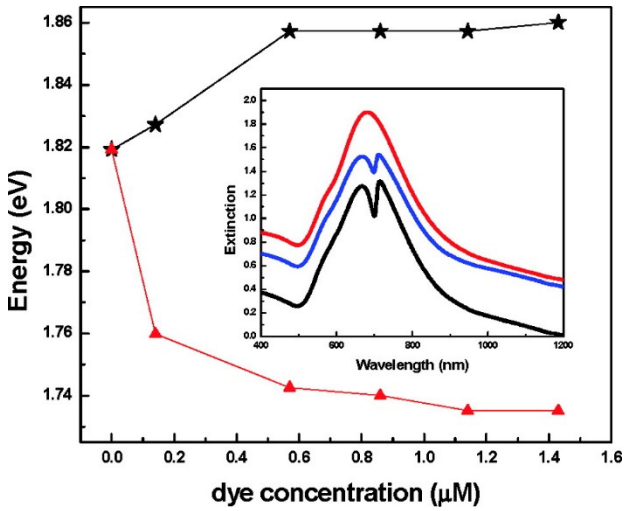


**Fig. 17 Plexcitonic energy-splitting.** By functionalizing the nanoshell with sodium 2-mercaptoethane sulfonate prior to complexation with J-aggregates, and then exposing said sulfonated nanoshells to dye solutions of various concentrations, Fofang et al.[8] are able to produce J-aggregates of various thicknesses. The onset of splitting-energies in the complex as a function of dye concentration in media is then observed. The experiment reveals a strong asymmetry in the onset of plexciton interaction in the complex with the spectra for various dye concentrations (Inset): 0 μL (red), 4 μL (blue), 10 μL (black), a characteristic that is attributed to dielectric screening or phase retardation effects. Reprinted with permission from Ref.[8] Copyright American Chemical Society (2008).

More recently, Tsargorodska et al.[156] have shed further light on the effective mechanisms of plasmon and exciton interactions that are so crucial in plexciton-based photocatalytic systems in their observation of gold nanostructure arrays exhibiting a splitting of their surface plasmon resonances upon attachment to Rhodobacter sphaeroides, a purple bacterium that captures sunlight via a light-harvesting complex 2 (LH2) which is then transmitted to another LH1 that

funnels the excitation into the photosynthetic reaction center resulting in the reduction of ubiquinone and allowing for the conversion of solar energy to chemical potential energy in the organic complex. Numerous studies have already demonstrated the plasmonic enhancement of fluorescence emission from light-harvesting complexes of bacteria[157], but Tsargorodska et al.[156] provide a new perspective by presenting changes in the extinction of metal nanostructures after the attachment of light harvesting complexes. This splitting is attributed to strong coupling between the localized surface plasmon resonances and excitons in the light-harvesting complexes. Utilizing wild-type and mutant LH1 and LH2 from purple bacterium containing different carotenoids Tsargorodska et al.[156] observe different splitting energies, and thus are able to demonstrate that the coupling mechanism of plasmons and excitons is sensitive to the electronic states in the light harvesting complexes (Fig. 18). For example, the extinction spectrum of a hexagonal array of gold nanodisks of period $310 \pm 30$ nm, diameter $154 \pm 22$ nm and height $19 \pm 3$ nm demonstrate these dramatic changes after binding with wild-type LH2. This results in a splitting of the plasmon band at wavelengths of 527 and 624 nm. The dramatic change in the extinction spectrum after the attachment of LH2 to the array of gold nanostructures is indicative of plasmon-protein coupling. Similar behavior is also reported with the attachment of LH1 to the array of gold nanostructures also displaying a splitting of the plasmonic band at 537 and 652 nm.

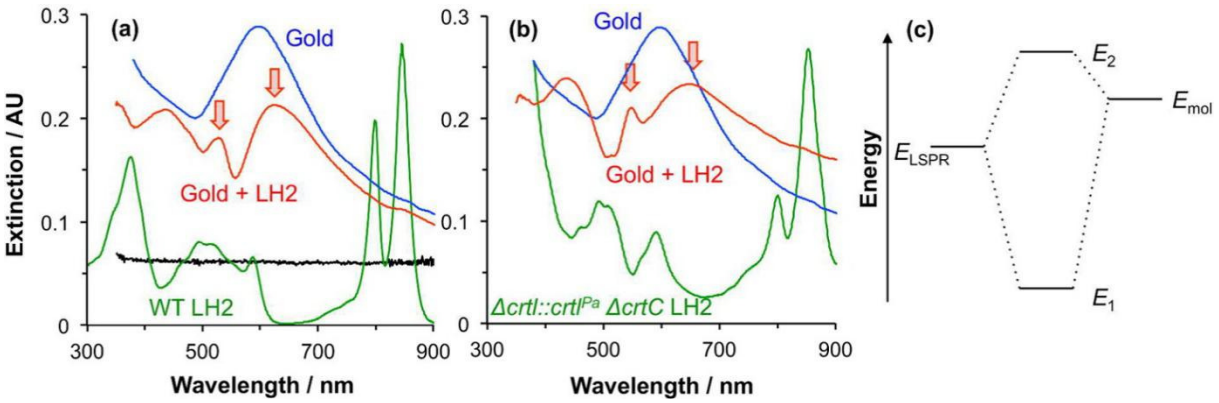


**Fig. 18** Extinction spectra for arrays of gold nanostructures before and after (blue and red, respectively) attachment of the light-harvesting complexes (a) wild-type LH2 and (b) the ΔcrtI::crtI$^{Pa}$ ΔcrtC mutant of LH2. The arrows are indicative of the splitting of the LSPR plasmonic band, while the absorption spectra of the proteins in solution are shown in green. The extinction spectrum of a monolayer of wild-type LH2 adsorbed on glass is presented as a black trace in (a). (c) describes the resultant two new peaks with energies $E_1$ and $E_2$ due to the strong LSPR and exciton state coupling. Reprinted from Ref[156] with attribution and adherence to Creative Commons Attribution License (CC BY) http://creativecommons.org/licenses/by/4.0/

Tsargorodska et al.[156] are further able to reveal these dependencies of the coupling strengths on molecular organizations and protein coverage in a comparative experiment where they utilize light-harvesting complexes with different carotenoid compositions but of otherwise identical structures (Fig. 19). Simultaneously, these marked differences in coupling strengths provide a new dimension of analysis that helps reflect the differing molecular organizations of the light harvesting complexes under consideration, and their means of transfer optical energy into the corresponding reaction centers.

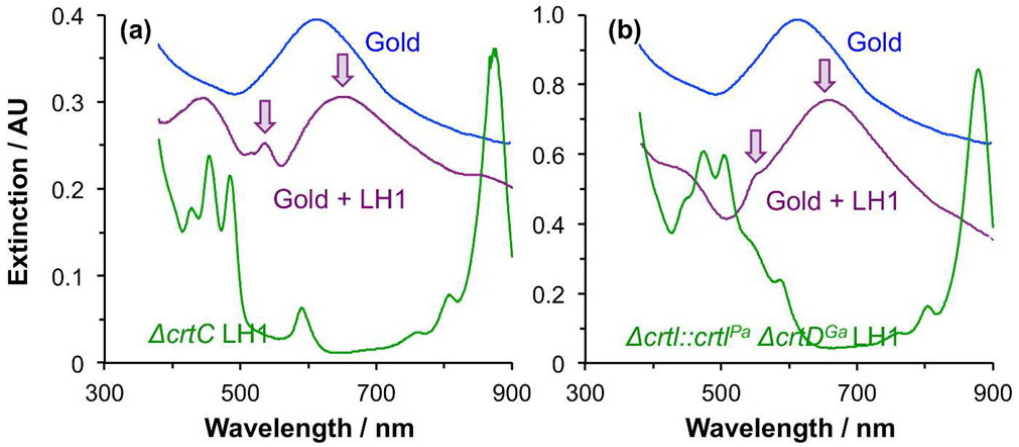


**Fig. 19** Extinction spectra for arrays of gold nanostructures before and after (blue and purple, respectively) attachment of the light-harvesting complexes (a) the ΔcrtC mutant of LH1 and (b) the Δcrtl::crtl$^{Pa}$ ΔcrtD$^{Ga}$ mutant of LH1. The absorption spectra of the proteins in solution are shown in green. Reprinted with permission from Ref[156] with attribution and adherence to Creative Commons Attribution License (CC BY) http://creativecommons.org/licenses/by/4.0/

In a similar fashion, another study by Li et al.[158] has demonstrated that the orientation of the exciton dipole has a significant influence in plasmon-exciton coupling. Diverting from the strong coupling regime, Li et al.[158] explore the weak coupling regime in relation to the ability of SPPs to localize and guide light in subwavelength metallic structures, an active region of interest in photonic and optoelectronic applications. Li et al.[158] demonstrate a new approach to tackling the structural limitations faced in the excitation of SPPs in optoelectronic and photonic devices alike thus far being realized only in prisms,[159] gratings,[160] antennas,[161] and subsequently leading to difficulties in interconnection with conventional material components.[162] Taking advantage of the fact that exciton dipoles have a large range of wave-vectors in their near-field regime,[163, 164] an alternative strategy in directly coupling SPPs with exciton dipoles is considered, and is used to demonstrate that if the dipole orientation at the dielectric/metal interface were changed, it may

lead to significant differences in SPP excitation efficiencies, and consequently, the performance of SPP based devices.

Using a wetting-effect-assisted self-assembly, a hybrid nanostructure with Ag nanowires partially embedded into organic single crystals, in this case Tris[1-phenylisoquinolinato]iridium (III) ($Ir(piq)_3$), is fabricated. Using a focused laser beam, the ordered molecular aggregates are excited to provide Frenkel excitons with regular orientations around the Ag nanowire. These ordered exciton dipoles at the interface assist in launching the SPPs through near field coupling resulting in their propagation along the Ag nanowire and coupling out from the ends of the wires in the form of photons. Simulated electric field analyses present that by altering the direction of the Ag nanowires in the hybrid structure, obtaining structures with different cross angles between the exciton dipoles and the Ag nanowire, that the cross-angle orientation has a great influence on the exciton-SPP coupling efficiency (Fig. 20). Subsequent experimental efforts utilizing photoluminescence and bright field imaging, on the fabricated hybrid nanostructure confirm the simulated data, demonstrating the decisive role of exciton dipole orientation in plasmon-exciton coupling.

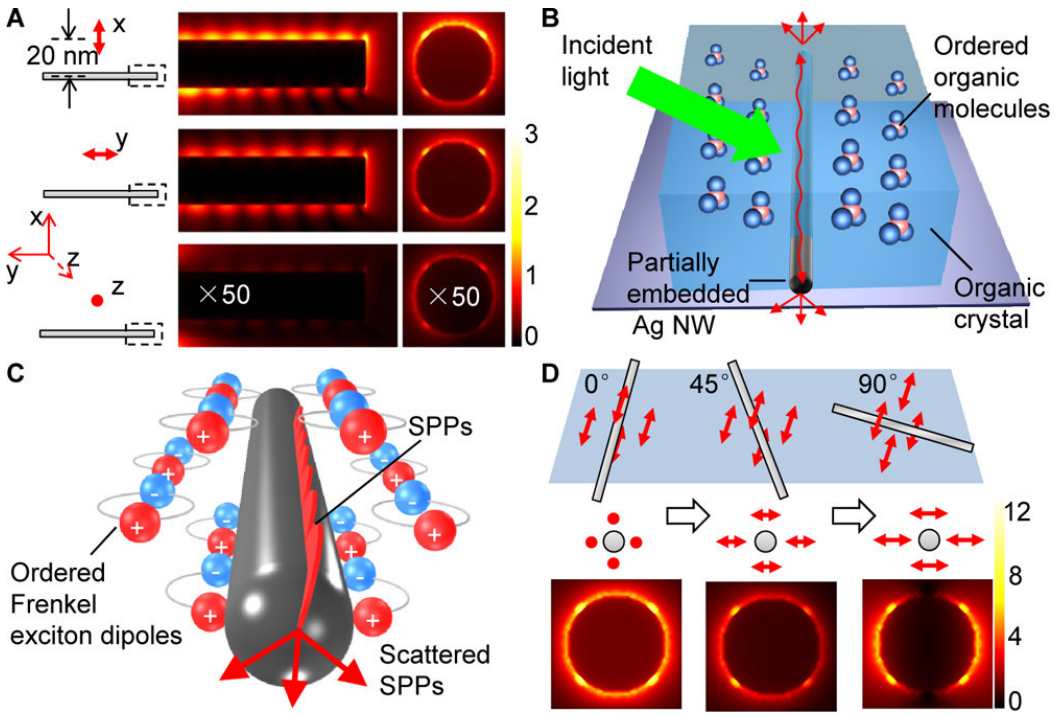


**Fig. 20 Hybrid organic/metal nanowire heterostructure** for the study of orientation-dependent plexciton coupling. (a) $|E|^2$ distributions of SPPs simulated numerically at the end of an Ag nanowire (200 nm diameter diameter and 6 μm in length). SPPs are observed to be launched by a dipole, positioned at the middle of the wire at a distance of 20 nm, oriented along all three coordinate axes x, y, and z respectively. (b) Schematic illustration of the embedded organic/metal nanowire heterostructure. (c) Upon irradiation of an incident light at the organic-metal interface, oriented Frenkel exciton dipoles are created around the metal nanowire. The exciton dipoles assist in successfully launching the SPPs along the Ag nanowire, which eventually scatter into free space at the distal ends. (d) The influence of orientation, represented by the cross angles between the Ag nanowire and dipole polarizations, on the electric field intensity of the SPPS for $0^0$, $45^0$, and $90^0$. Reprinted with permission from Ref[158]. Copyright American Chemical Society (2017).

## 5.2 Plexcitonic Photocatalysis

The development of plexciton-based photocatalytic systems has accompanied the study of plasmon-exciton coupling in an increasing need to facilitate higher efficiency catalytic reactions on the surface of plasmonic nanostructures, a direct alternative to traditional thermal-driven

heterogeneous catalysis.[105, 165, 166] Several notable systems have shown great promise for their use of the strong coupling of plasmons and excitons in prolonging the lifetime of hot electrons, and increasing reaction efficiencies. Many such composite nanomaterials often involve the hybridization of electronic states in two-dimensional inorganic semiconductors and plasmonic metal materials. Systems of monolayer-graphene-Ag nanostructures[148, 150] and monolayer $MoS_2$-Ag nanoparticle hybrids[147] have been successfully applied in plexciton co-driven surface catalytic reactions.

Graphene, a single atomic layer of graphite, has been the center of attention thanks to its unique properties since its discovery in 2004.[167] Ding et al.[150] fabricated graphene-Ag nanowire (NW) hybrid materials (Fig. 21a), and have demonstrated the advantages the hybrid device has presented for surface catalytic reactions. By themselves, both graphene and silver nanowires are unimpressive catalytic substrates for the photoreduction of 4-nitrobenzenethiol (4NBT) to p,p'-dimercaptoazobenzene (DMAB). On graphene, the photoreduction of 4NPB exhibited a strong dependence on laser power, with complete disappearance of the N-O vibration of 4NPB at a Raman shift of 1325 $cm^{-1}$ (and corresponding increase of the Raman intensities of DMAB at 1390 and 1432 $cm^{-1}$), occurring only at a rather high laser power of 6.6 mW. In the case of Ag NWs, the laser-excited SERS spectrum ($\lambda_{exc}$ = 532 nm, $P_{laser}$ = 1.3 mW) contained features corresponding to both 4NBT and DMAB, indicating the chemical reaction to have partially completed.[150] However, for the Ag NW-graphene hybrid, the photoreduction was nearly 100 % complete even at a very weak laser power of 0.01 mW, indicating a synergistic enhancement of the plasmon-to-electron conversion efficiency, which was attributed to strong plasmon-exciton coupling.[150] Through ultrafast pump-probe transient absorption spectroscopy, femtosecond-resolved dynamics of plasmon-exciton coupling of the graphene-Ag nanowire hybrids were

elucidated. Ding et al.[150] demonstrated that although the hot electron transfer from the Ag nanowire to the graphene is slower, clocking around 534 ± 108 fs (Fig. 21b), compared to 240 fs for plasmon induced hot electron transfer from 10 nm gold nanodots to $TiO_2$ nanoparticles,[168] the lifetime of plasmon-induced hot electrons in graphene is 3.2 ± 0.8 ps (Fig. 21c) which is significantly longer than the period of collective electron oscillations in isolated Ag nanowires which is within 150 fs. Similar measurements on charge transfer time between the Ag nanowire and graphene were also made in the NIR (near-infrared) region (Fig. 21d) demonstrating a decrease in the kinetic energy of hot electrons to 0.8265 eV. This corresponds to a transfer time of about 780 ± 92 fs which is slower than in the prior case where the incident wavelength of light is in the visible regime. The fitted curve in (Fig. 21e) also reveals that the lifetime of plasmon-induced hot electrons in graphene is about 3.9 ± 0.9 ps thanks to better optical absorption for graphene in the NIR region. These results indicate that graphene strongly harvests hot electrons and extends the lifetime of the energetic charge carriers from femtoseconds to picoseconds, providing for an enhanced surface-plasmon-to-hot-electron conversion efficiency which is of great significance for plexcitonic systems that incorporate graphene and noble metal nanoparticles.

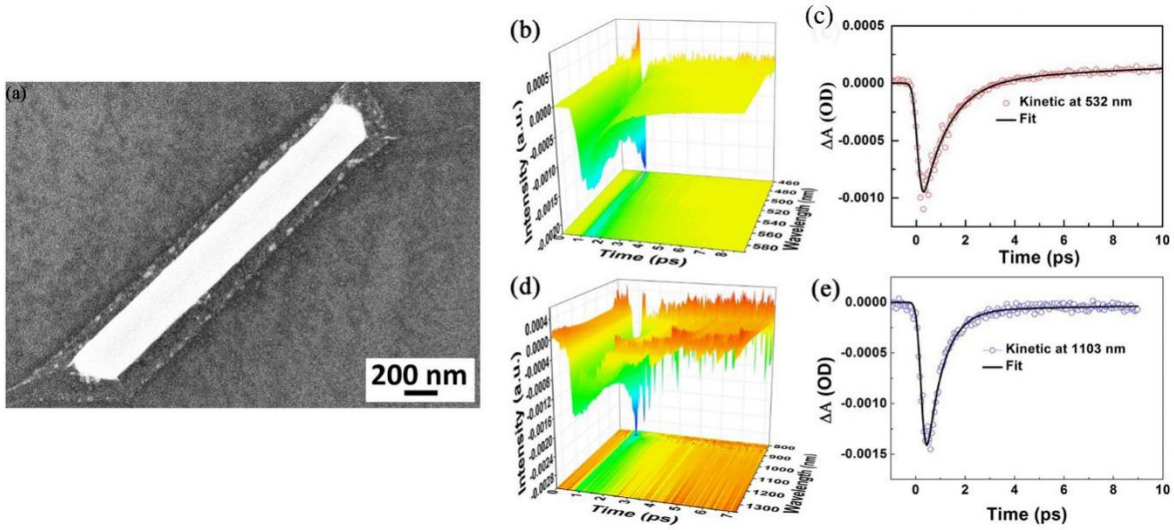


**Fig. 21 Analyzing the properties of graphene-Ag nanowire hybrids.** (a) SEM image of a single Ag nanowire coated with a monolayer of graphene. (b) Ultrafast pump-probe transient absorption spectroscopy of the hybrid structure when excited by a laser of wavelength 400 nm. The graph demonstrates the energy distribution of hot electrons along the measured wavelength range, revealing that plasmon-induced hot electrons lose kinetic energy during their transfer to graphene. (c) Fitted dynamic curve describing the kinetics of the material at 532 nm indicating the lifetime of plasmon-induced hot electrons in graphene. (d) Ultrafast pump-probe transient absorption spectroscopy of the hybrid structure in the NIR region. (e) Corresponding fitted dynamic curve at 1103 nm. Reprinted with permission from Ref.[150] Copyright Nature Publishing Group (2016).

Contrastingly, Yang et al.[147] presented a system of molybdenum disulfide ($MoS_2$), a transition metal dichalcogenide (TMDC), hybridized with a plasmonic metal nanomaterial, in this case Ag NPs, to drive the photoreduction of 4NBP to DMAB. TMDCs at nanoscales have been successfully applied for surface catalytic reactions owing to their unique properties.[169] $MoS_2$, a few layers of which can provide for large surface-to-bulk ratios and quantum confinement effects, is one such example,[170] but the efficiency of surface catalytic reactions using these materials has thus far been quite poor due to their large bandgaps and low yield of hot electrons. In a method similar to that of the plasmon-graphene coupling achieved by Ding et

al.[150], Yang et al.[147] demonstrate that a hybrid system involving a monolayer of $MoS_2$ on plasmonic Ag nanostructures can rectify these problems. While $MoS_2$ showed negligibly small photocatalytic activity under 532 nm laser illumination for the reduction of 4NPB to DMAB, Ag NPs showed modest photocatalytic activity for a laser power of 0.0015 mW with a Raman intensity ratio of product (1432 $cm^{-1}$) reactant (1338 $cm^{-1}$) to reactant of 0.5 in the absence of $MoS_2$ (Fig. 22a).[147] For the same illumination wavelength and laser power, Ag NP/$MoS_2$ hybrids showed an almost six-fold improvement of photocatalytic activity, achieving $I_{1438}/I_{1338}$ of 2.8, demonstrating the synergistic enhancement of photocatalytic activity due to plasmon-exciton interactions. When the laser power was increased to 0.015 mW, the Raman peak at 1338 $cm^{-1}$ (corresponding to the 4NPB reactant) disappeared for the $MoS_2$/Ag hybrid system, while a small peak was still observable for the Ag NPs system, which confirmed the plexcitonic enhancement of photocatalytic activity (Fig. 22b).[147]

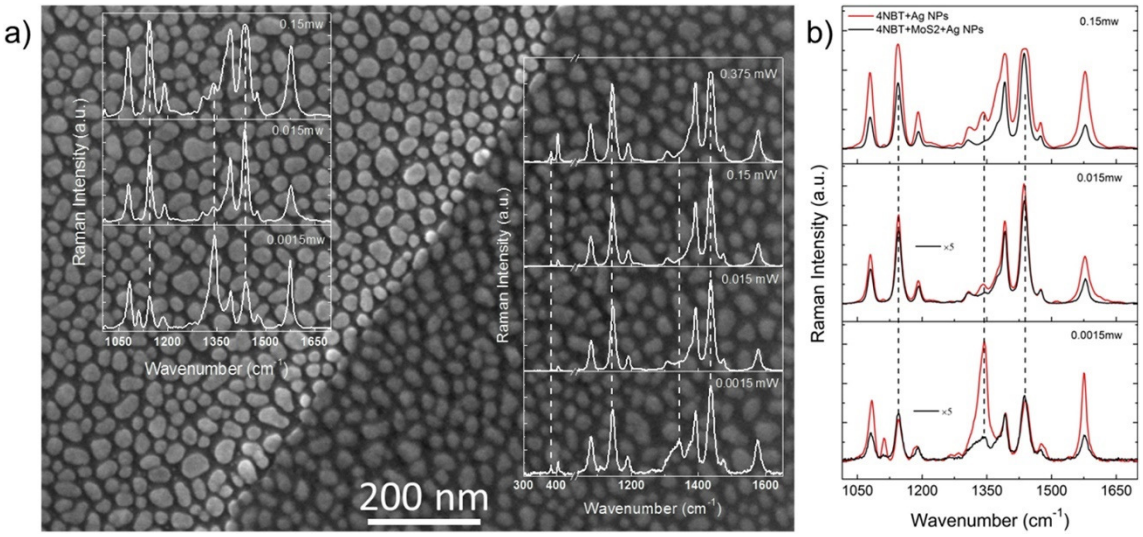


**Fig. 22 SERS analysis of the $MoS_2$-Ag nanocomposites.** (a) The substrate for the relevant experiments and the corresponding SERS spectra are shown, with Ag nanoparticles alone on the left, and for the case where the nanoparticles are covered by $MoS_2$ on the right. (b) Surface catalytic reactions for 25 nm nanoparticles with (black) and without (red) $MoS_2$. At the lower intensity of 0.0015 mW, Yang et al.[147] observe that the ratio of the Raman intensity of the reactant (1338 $cm^{-1}$) to the product (1432 $cm^{-1}$)

is 0.5 without $MoS_2$ and 2.8 with $MoS_2$, confirming the probability of a chemical reaction for molecules directly adsorbed on the Ag NPs is lower than that for those adsorbed on the $MoS_2$/Ag substrate. Reprinted with permission from Ref.[147] Copyright Elsevier (2017).

Yang et al.[147] investigated the plasmon-exciton couplings of monolayer $MoS_2$/Ag nanoparticle hybrids for different sizes of Ag nanoparticles on quartz (with diameters of 6.1 nm, 14.5 nm, and 25 nm) using transmission spectroscopy, fluorescence spectroscopy, and surface-enhanced Raman scattering (SERS) spectroscopy. Transmission spectra of the monolayer $MoS_2$/Ag nanoparticle hybrids on quartz were measured (at thicknesses of 1.5 nm, 5 nm, and 10 nm) to validate plexciton coupling (Fig 12). Atomic force microscopy is used to determine the diameters of the Ag NPs on quartz and are approximately 6.1 nm, 14.5 nm, and 25 nm. For the smaller diameter Ag NPs (6.1 nm) (Fig. 23a) the offset between the LSPR peak (at 458 nm) and the exciton absorption peak of $MoS_2$ results in weak coupling. To rectify this, the resonance peak is tune by increasing evaporation time, depicting a plexciton resonance dependency on the deposition time similar to what has been observed in the work of Nan et al.[72] This is further supported by the fact that the LSPR peaks of nanoparticles of different thicknesses clearly shift plexciton resonance peaks from 458 nm to 515 nm as the Ag nanoparticle sizes increase (Fig. 23b). The strong coupling of the $MoS_2$/Ag nanoparticle hybrid system is noted to occur when the LSPR peak of Ag and the exciton absorption peak of $MoS_2$ overlap and is characterized by a strong plasmonic absorption transition dipole moment consisting of the collective oscillations of electrons interaction with that of the transition dipole moment of $MoS_2$. The absorption of the hybrid system is in fact observed to shift from 438 nm to 532 nm (Fig. 23c).

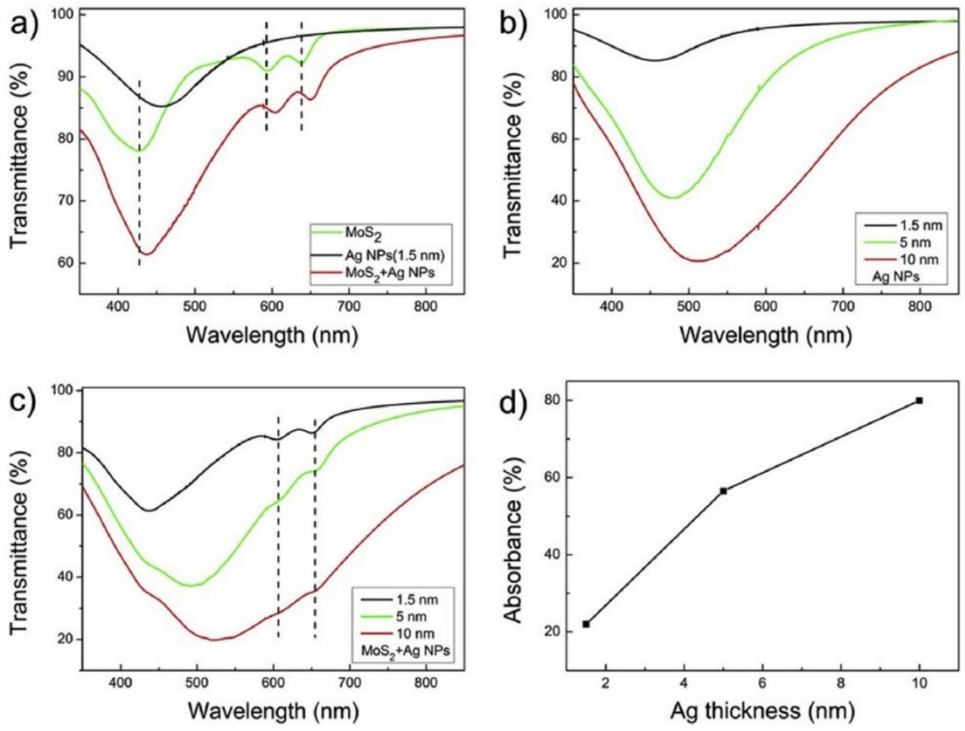


**Fig. 23** (a) Comparisons of transmission spectra of monolayer $MoS_2$, Ag nanoparticles (of diameter 6.1 nm), and $MoS_2$/Ag nanoparticle hybrid structure on a quartz substrate. (b) Transmission spectra of Ag nanoparticles (of diameters 6.1, 14.5, and 25 nm) on varying thicknesses of quartz substrate (1.5, 5, and 10 nm). (c) Transmission spectra of $MoS_2$/Ag nanoparticle hybrids on varying thicknesses of quartz substrate (1.5, 5, and 10 nm). (d) Absorbances for three kinds of hybrid $MoS_2$/Ag nanoparticle structures for incident light of wavelength 532 nm. Reprinted with permission from Ref[147]. Copyright Elsevier (2017).

Photoluminescence results (Fig. 24) also supplement these facts where it is revealed that the plexciton coupling can be adjusted through the tuning of the LSPR; weak coupling is signified by a minimal enhancement in photoluminescence (by a factor of 2.5) (Fig. 24a), and strong coupling by a maximum enhancement in photoluminescence (by a factor of 14) (Fig. 24b). The strongest plexciton coupling case is demonstrated to occur due to the Purcell effect[171] where the photoluminescence intensity of $MoS_2$ is enhanced by a factor of 52 due to the LSPR (Fig. 24d). Enhanced excitation absorption via LSPR is consequently shown to provide for the transfer of thermal energy to the surface of $MoS_2$, and the resultant hot carriers on the surface of

$MoS_2$. This carrier-carrier interaction, Yang et al.[147] emphasize, as vital for the promotion of surface catalytic reactions.

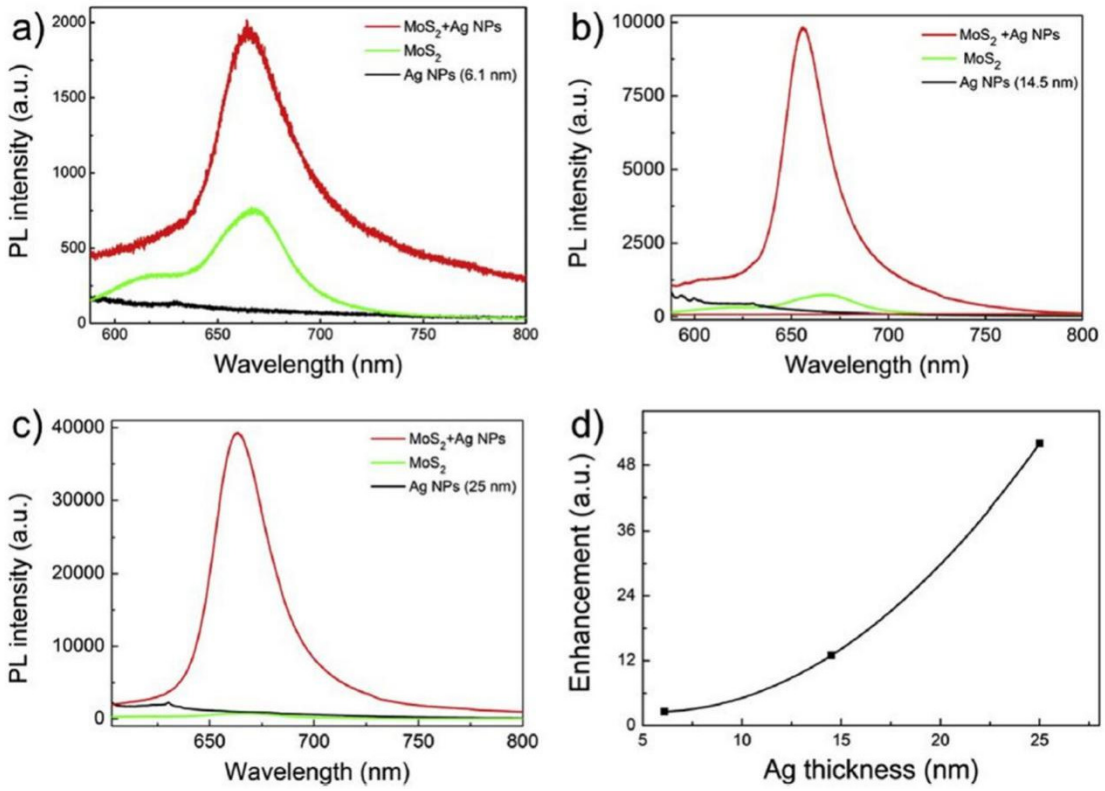


**Fig. 24** (a) – (c) Photoluminescence (PL) spectra of $MoS_2$ displaying PL enhancement through local surface plasmon resonance for Ag nanoparticles of diameters 6.1, 14.5, and 25 nm. (d) LSPR enhancement factors for different quartz thicknesses. Reprinted with permission from Ref[147]. Copyright Elsevier (2017).

Apart from the composite systems seen thus far, the incorporation of semiconductor quantum dots (QDs) in plexcitonic systems has also been of great interest in the field. Semiconductor QDs offer several advantages[34, 172] in that their absorption spectrum extends over a broad range, and can be easily made to overlap with the spectrum of plasmonic nanoparticles of various sizes.[173] In comparison, their emission spectrum is narrower to that of the plasmon, and thus by selecting QDs of appropriate sizes one can tune the exciton emission across the

plasmon resonance. Furthermore, the strong oscillator strength of the QD exciton allows for easy single object experiments.[173] Some of this comes to play in the work of Deng et al.[174] where they combine the local surface plasmon resonance effect of Ag nanoparticles with that of the up-conversion property of nitrogen-doped graphene quantum dots (N-GQD), a property that helps them serve as photosensitizers for capturing visible and near-infrared (NIR) light, in a ternary Ag/N-GQD/g-$C_3N_4$ nanocomposite (Fig. 25).

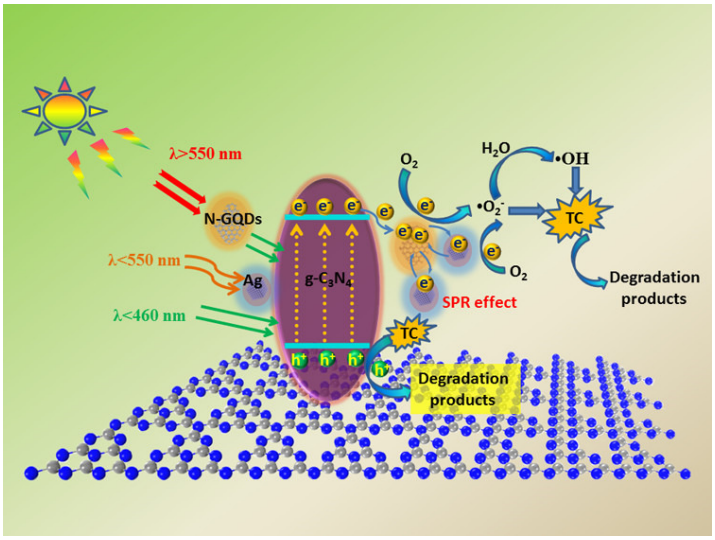


**Fig. 25** Schematic of the ternary Ag/N-GQDs/g-$C_3N_4$ nanocomposite as presented by Deng et al.[174] The boosted photocatalytic activity of the nanocomposite structure, such as its high-percentage removal efficiencies of tetracyline (TC) is attributed to a synergistic effect among its three components each of which promote light absorption and transfer ability as an efficient photocatalyst of broad-spectrum light response with potential for wastewater pollution control. Reprinted with permission from Ref.[174] Copyright American Chemical Society (2017).

Furthermore, N-GQDs provide for low toxicity, adequate electrical conductivity, and excellent photochemical properties.[175, 176] Similarly, it has been understood that Ag/g-$C_3N_4$ composites present enhanced absorption in the whole visible light region, but their inability to harness light of longer wavelengths, such as NIR light, has been their greatest impediment. By co-doping Ag nanoparticles and N-GQDs on a g-$C_3N_4$ nanosheet surface, Deng et al.[174] combine the potential of N-GQDs to efficiently promote the photocatalytic activity of other photocatalysts along with the LSPR effect of Ag nanoparticles, and the visible light response ability of g-$C_3N_4$ to produce novel Ag/N-GQDs/g-$C_3N_4$ nanocomposites that present enhanced full-spectrum light response ability even in NIR light. The experimental results are quantified in the nanocomposite's enhanced ability to efficiently degrade tetracycline, as opposed to pristine g-$C_3N_4$, with removal efficiencies of 92.8 % and 31.3 % under full-spectrum and NIR light irradiation, respectively (Fig. 26).

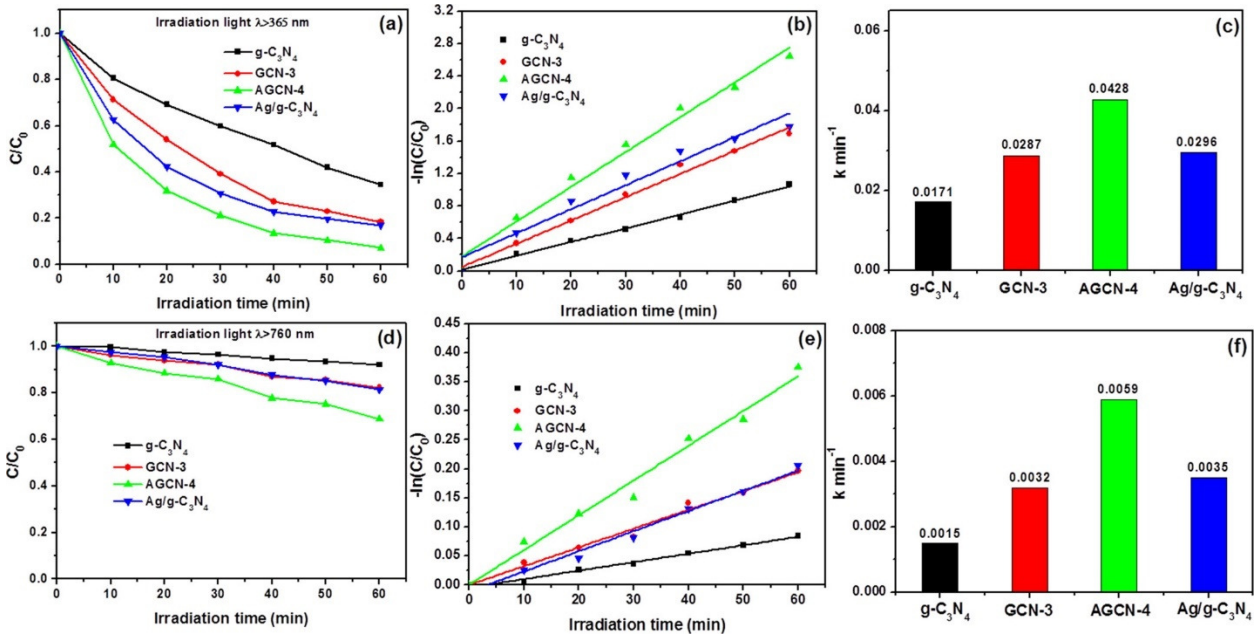


**Fig. 26 Photocatalytic degradation of Tetracyline.** Deng et al.[174] evaluate the performance of the ternary photocatalyst by conducting experiments for TC removal. (a)-(c) Under full-spectrum light

irradiation ($\lambda$ > 365 nm) all the samples display boosted photocatalytic activity for TC removal, with optimal results of 92.8% removal efficiencies evidenced in the ternary nanocomposite AGCN-4. (d) The photocatalytic activity is observed to decline greatly under NIR light irradiation compared to those in visible or full-spectrum light. This is attributed to the long wavelength and relatively weak energy of light in these regimes. Pristine g-$C_3N_4$ was noted to present the weakest photocatalytic performance while the GCN-3 and Ag/g-$C_3N_4$ samples maintain a higher photocatalytic performance, in comparison to the pristine g-$C_3N_4$, but still very low as a standard register. (e)-(f) Meanwhile the ternary nanocomposite's performance is further improved presenting a 31.3% removal efficiency and 0.0059 $min^{-1}$ reaction rate. Reprinted with permission from Ref.[174] Copyright American Chemical Society (2017).

Deng et al.[174] attribute the excellent photocatalytic activity of the ternary Ag/N-GQDs/g-$C_3N_4$ nanocomposite to a synergistic effect among the three components wherein the g-$C_3N_4$ nanosheets serve as a loading matrix for the Ag nanoparticles and N-GQDs. Both the plasmonic Ag nanoparticles and N-GQDs serve as nanoantennae for improved visible-light absorption and enhancement effects, as well as the conversion of NIR light, resulting in the utilization of the full spectrum of solar energy and more photogenerated charge carriers while promoting their transfer and reducing recombination processes. Photoelectrochemical, transient photoluminescence, and UV-vis techniques are further used to distinguish the inherent charge transfer and separation dynamics that occur within the system, allowing for its optimization as a highly efficient, broad-spectrum response photocatalyst.[174]

### 5.3 Plexcitonic Photovoltaics

In-depth investigations on the nature of plexcitonic coupling have also paved the way for numerous developments in photovoltaics. Silicon-based solar cells currently occupy a majority market share in the market for photovoltaic panels despite the glaring issues of weak optical absorption (due to silicon's indirect bandgap) and a highly energy intensive manufacturing

process. The former issue has been addressed through several means but most extensively through the addition of metal nanoparticles (NPs) in the existing structures of silicon solar cells. The extremely localized electric fields on the surface of metal nanoparticles (NPs) can enhance the absorption of silicon in both the strong and weak coupling regimes. Metal NPs are most often employed in photovoltaics to either scatter or trap light themselves.[177] Typically, metal NP arrays are either embedded in the active layer(s) or are found at the junction of the active layer with the adjacent layer in what are deemed as plasmonic solar cells. A deeper discussion of plasmonic solar cell architecture is outside the scope of this article. However, a thorough and complete review of this subject has been compiled by Pohman et al.[127] The architecture of such solar cells shares many commonalities and the most archetypal architectures are shown in (Fig. 27). The use of plasmonics coupled with typical solar cell materials have been investigated for every major type of solar cell, from dye-sensitized solar cells[178, 179] to inorganic[180, 181] to polymer cells.[182, 183]

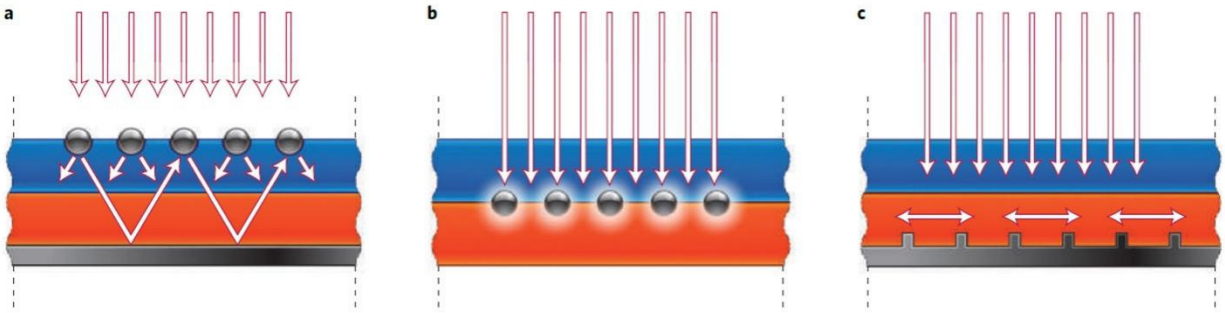


**Fig. 27** (a), (b), and (c) depict the three most common ways in which plasmonic particles are used in a solar cell: light scattering, light trapping by individual particles and trapping via surface plasmon polariton production on arrays. Reprinted with permission from Ref.[127] Copyright Nature Publishing Group (2010).

Research regarding the application of plexcitonic solar cells is still at its infancy but as presented in the work of Balci et al.,[26, 184, 185] the marked difference of plexcitons from their constituents and their significant ability to create new energetic energy levels in participating

materials did not go unnoticed. Plasmonic metal NPs are considered useful for their absorption and scattering abilities;[127, 186] as shown in (Fig. 28), plasmonic nanocrystals are unique as optical systems exhibiting an optical cross section greater than their physical cross section, lending to their ability to greatly enhance the interaction between light and local chromophore materials.[187]

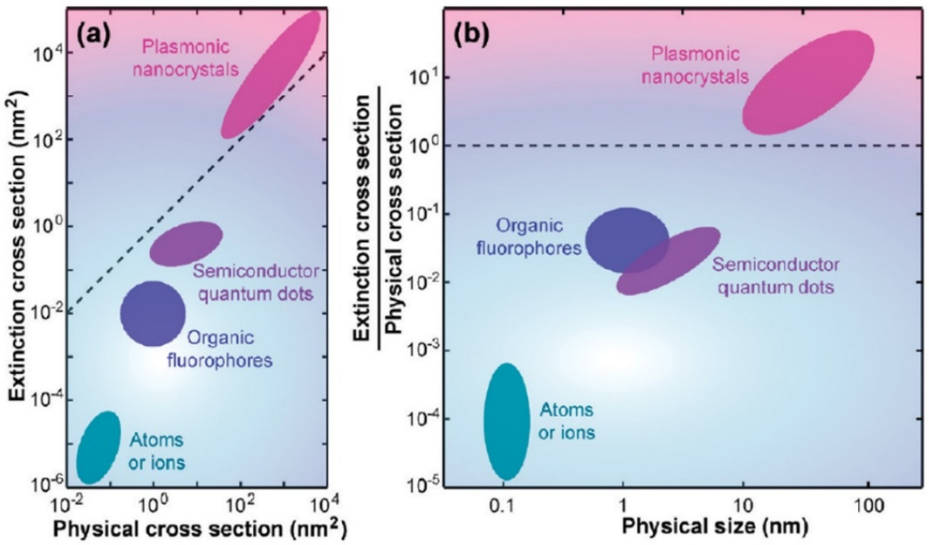


**Fig. 28** (a) The optical properties of several types of optical species in terms of their extinction and physical cross sections, (b) Comparison between the extinction and physical cross sections to the physical size of the same optical species further affirming the uniqueness of plasmonic crystals as optical materials. Reprinted with permission from Ref.[187] Copyright American Chemical Society (2012).

Beyond plasmons, plexcitons can absorb a novel light signature and promote longer exciton lifetimes.[124, 127, 186, 188, 189] Such phenomena have made plexcitonic systems ideal for solar cell applications.[155, 186, 189, 190] Here too, the nature of plexcitonic coupling is a crucial factor.[156] It has been shown that plexcitonic coupling can improve important parameters used to measure the efficiency of solar cells such as the $J_{SC}$ (short-circuit current), $V_{OC}$ (open circuit potential) and PCE (power conversion efficiency).[72, 192] Plexcitons are able to contribute to the photocurrent via an additional charge carrier transfer mechanism known as plasmon resonant energy transfer

(PRET). Surface plasmon (SP) resonant frequency tuning is required to achieve superior PRET, the optimizing of which could lead to plexcitonic solar cells outperforming ordinary solar cells.[189] Plexcitonic analogs can be found in almost every type of solar cell, ranging from polymer to silicon and perovskite. Such flexibility in application is one of the great strengths of employing a plexcitonic approach to light harvesting.

A case study in example follows the work of Nan et al.[72] who demonstrate the design of plexciton-sensitized solar cells (plexciton-SSCs) with higher injection efficiencies and sum output power as compared to individual plasmon- and exciton-SSCs. It is suggested that the Fano resonance induced by strong plasmon-exciton coupling provides an efficient channel for the conversion and coherent transfer of energetic charge carriers from metallic plasmons to molecular excitons and organic dye molecules. Nan et al.[72] present a three-level experiment in a comparative review of the ultrafast dynamical processes and energy transfer channel efficiencies in plasmon-SSCs involving gold nanofilms (NFs) composed of Au nanoparticles (AuNPs) on $TiO_2$, an exciton-SSC involving a metal-molecule hybrid system consisting of Au nanofilms decorated by cholorophyll (Chl) molecules, and a plexciton-SSC based on a combination of the former plasmon and exciton-SSCs (Fig. 29).

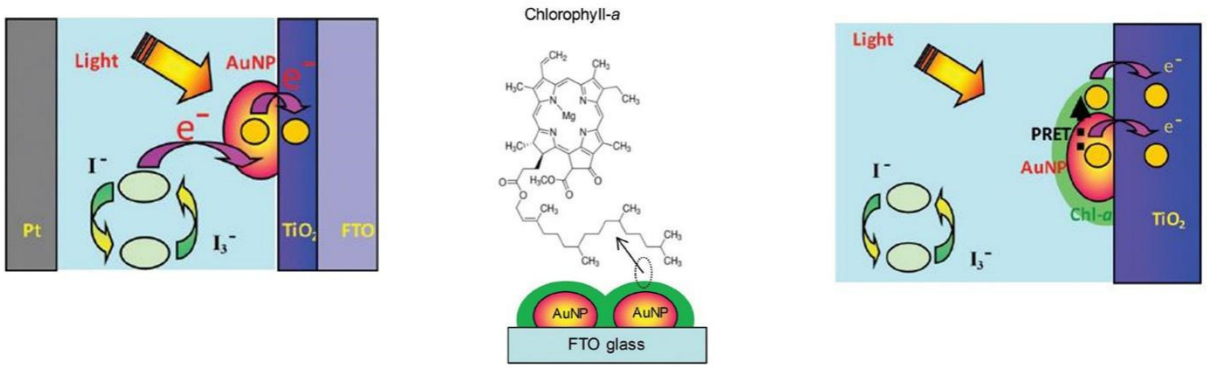

**Fig. 29 Hybrid Plexcitonic Solar Cell.** Schematics of the three systems that Nan et al.[72] analyze in addressing the development of a hybrid plexciton-sensitized solar cell (plexciton-SSC). (Left) Plasmon-sensitized solar cell (plasmon-ssc) depicting the charge transfer channel from the bare plasmon to cell anodes in a noble-metal nanoparticle-semiconductor device where a thin film of Au nanoparticles is deposited atop a $TiO_2$ surface set on a transparent FTO conductive substrate, with a Pt film as the counter anode. $I^- \leftrightarrow I_3^-$ is utilized as the redox agent for the electrolyte. LSPR of the gold nanoparticles results in the transfer of photoelectrons from the Au nanoparticle to the conduction band of $TiO_2$ and are subsequently injected into the anode. (Center) Exciton-sensitized solar cell (exciton-SSC) where a thin film of Au nanoparticles is decorated with chlorophyll (Chl) molecules. Inset: chemical structure of a Chl molecule. (Right) Plexciton-SSC of Au nanoparticles on a $TiO_2$ substrate and decorated with cholorophyll (Chl) molecules. Efficient plasmon resonance energy transfer from the metallic plasmons of the Au nanoparticles to molecular excitons, via strong coupling, leads to a hybrid photoelectron transfer channel from the plexcitonic complex to the $TiO_2$ metal oxide system. Reprinted with permission from Ref.[72] Copyright Royal Society of Chemistry (2016).

The varied nature of the surface plasmon resonance (SPR) of the Au NFs, tuned from 550 to 780 nm, is shown to be dependent on the deposition time with a broadening of the spectral width and a red-shift of the SPR wavelength as the deposition time increases (Fig. 30a). Spectral data on the plasmonic response of the relevant samples is obtained using UV-Vis-NIR spectroscopy. The open-circuit voltage ($V_{OC}$) of the AuNF-SSCs is seen to increase from 60 mV to a maximum of 126 mV as deposition time increases to 90 s ($\lambda_{SPR}$ = 709 nm), while the short-circuit current ($J_{SC}$) increases from 13 μA $cm^{-2}$ to a maximum of 30 μA $cm^{-2}$ as deposition time increases to 100 s ($\lambda_{SPR}$ = 739 nm) (Fig. 30b). Both $V_{OC}$ and $J_{SC}$ decrease as the SPR is further redshifted. A similar analysis of the exciton-SSC is used to demonstrate the tunability of the plexciton Fano resonance and the SPR of Au@Chl hybrids. The strong coupling between plasmons and excitons is identified by Rabi splitting in the absorption spectra, with a stronger

plasmon-exciton coupling at larger concentrations of molecular Chl (Fig. 30c). The SPR wavelength is tunable from 550 to 780 nm by selective control of the density of the deposited Au NPs and the mass thickness of the film, mutually dependent on the deposition time. Using the time-resolved optical differential transmission method, Nan et al.[72] identify three relevant features for coherent energy transfer from plasmons to excitons in these hybrid systems: (i) increasing dye concentrations enlarge coupling between plasmons and excitons while inducing a deeper Fano dip (Fig. 30d-30e), (ii) the maximum Fano dip is characteristic of the energy of the molecular exciton resonance, and (iii) that the depth of the Fano dip is most prominent when coupled around the plasmon resonance.[72]

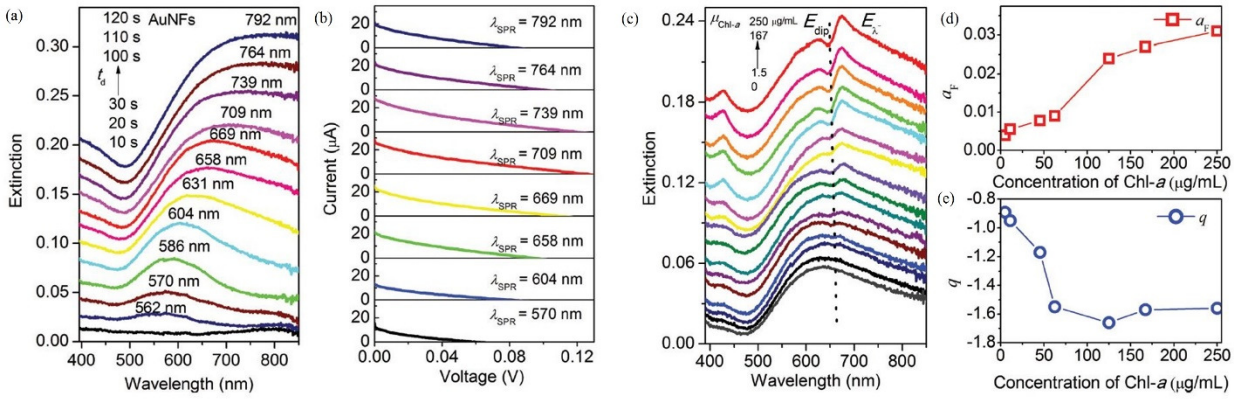


**Fig. 30 Spectral Characterization of the Plasmon-SSC and Exciton SSC.** (a) Extinction spectra of Au nanofilms in the plasmon-SSC for different deposition times. (b) Localized surface plasmon resonance dependent J-V curves of the plasmon-sensitized solar cell. (c) Fano line-shaped extinction spectra of exciton-SSC with a fixed LSPR at 620 nm for varying dye concentrations from 1.5 to 250 $\mu$g mL$^{-1}$. The Fano dip is identified by the dotted line. (d) - (e) Dependency of the Fano amplitude $a_F$ and the Fano factor $q$ on the dye concentration. As the concentration of Chl molecules increase, the Fano dip becomes blue-shifted, and is accompanied by corresponding increases in the Fano amplitude and factor. Reprinted with permission from Ref.[72] Copyright Royal Society of Chemistry (2016).

It is also important to distinguish the charge-separation pathways that occur in the three individual systems. In the case of the plasmon-SSCs involving gold NFs composed of AuNPs on $TiO_2$, the surface plasmon resonance of the AuNPs induces a dipole and supports the transition of photoelectrons under light excitation, which are transferred from the surface plasmon resonance level of the AuNPs to the conduction band of the $TiO_2$ film, and subsequently injected into the anode. This is very much the plasmonic counterpart to the classical interfacial charge transfer mechanism (IFCT), also referred to as plasmon-induced metal-to-semiconductor interfacial transition (PICTT)[193] where the noble metal plasmon, thanks to the strong coupling and mixing of the metal and semiconductor levels, allows for the direct generation of an electron in the semiconductor and a hole in the noble metal. In the case of the AuNPs, the dipole induced by the surface plasmon resonance does exactly this and acts as a supportive energy level promoting the direct generation of electron in the semiconductor and a hole in the noble metal.

On the other hand, in the case of the exciton-SSC, the Chl molecules have S- and Q-exciton absorption bands at around 420 nm and 660 nm, respectively. It is the incoherent coupling of the S-band exciton of the Chl moleucles with *d*-band bound electrons of AuNFs that leads to the weak peak in (Fig. 30c) around 420 nm. Meanwhile, the coherent coupling of the Q-band excitons of the Chl molecules with the surface plasmon resonance of the AuNFs leads to the asymmetric Fano resonance line-shape. The Fano dip in the absorption spectrum can be attributed to coherent plasmon resonant energy transfer (PRET) from the metal nanostructure to the dye molecules. Alternatively, it could also be understood that the dephasing of the plasmon of the AuNFs is attributable to the presence of the molecular adsorbate in a process known as chemical interface damping (CID). The broadening of the resonance evidenced in (Fig. 30c) further supplements this view and describes how CID, absent in the IFCT mechanism, provides

an alternative and additional pathway for the dephasing of the plasmon and transfer of the energetic charge carriers. To further distinguish the plexcitonic charge transfer process via PRET, Nan et al.[72] used time-resolved optical differential transmission to observe the transient absorption spectra of Chl, the Au film, and the Au@Chl hybrid at the Fano dip wavelength around 650 nm. While a positive signal for the current is observed for the AuNFs, attributed to the decay of hot electrons converted from plasmons as well as hot electron-phonon coupling, Chl displays no obvious signal as the amount of Chl is too small, while the Au@Chl hybrid provides a negative signal response. This is seen as directly indicative of the fact that the excited-state energy upon resonant illumination can relax through PRET in the strongly coupled Au@Chl hybrids.

The processes aforementioned in describing the charge carrier mechanisms of the plasmon-SSC and the exciton-SSC culminate in the plexciton-SSC where an efficient channel of coherent charge transfer is found involving an additive process of PICTT between the AuNFs and $TiO_2$ supplemented by the small molecule plasmon-enhanced interfacial charge transfer from the adsorbed Chl molecule to the semiconductor in a dissociation induced electron transition (DIET) process,[23, 69] a subset of CID, to enhance light-harvesting efficiencies.[72]

Nan et al.[72] explored the performance of a plexciton-SSC (Fig. 31) based on Au@Chl hybrids. It is noted that both the $J_{SC}$ and the $V_{OC}$ of the Au@Chl-SSCs experience prominent increases, by 66 % for the former and 37 % for the latter, compared to those of AuNF-SSCs (Fig. 31a-31b). This is because of the resonant coupling between the plasmons of the AuNFs with excitons from the Chl molecules at a wavelength of 709 nm. The relevance of structural parameters is duly noted as the corresponding values for $J_{SC}$ and $V_{OC}$ of the Au@Chl-SSCs are smaller than that of Chl-SSC when deposition time is < 30 s. This is correlated with the small

size of the AuNPs and the off-set resonance of the plasmon and exciton. Maximal power outputs of 0.6 and 1.3 μW (Fig. 31c), for AuNF-SSC and Au@Chl-SSC respectively, as opposed to 0.3 and 0.1 μW for Chl-SSC and bare $TiO_2$-SSC confirm that plexciton-SSCs with strong Fano resonances, via the careful adjustment of the microstructure and plasmons of AuNFs to achieve optimal coupling with excitonic molecules, provide a more efficient transfer channel of photoelectrodes.

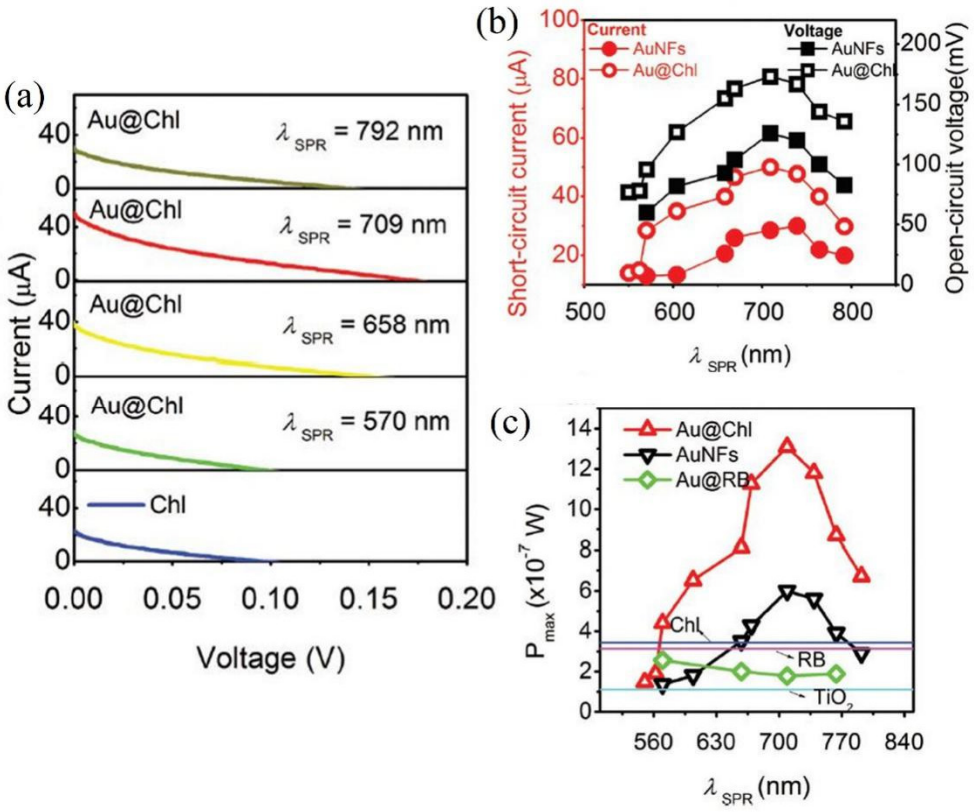


**Fig. 31 Hybrid Plexcitonic Solar Cell.** (a) – (b) Short-circuit current ($J_{SC}$) and open-circuit voltage ($V_{OC}$) of the hybrid plexciton-SSC. Note the prominent increase in both parameters due to the strong coupling that occurs between the plasmonic Au nanoparticles and the excitonic Chl molecule. Both $J_{SC}$ and $V_{OC}$ of the plexciton-SSC reach their maxima at a LSPR wavelength of 709 nm for a deposition time of 90 s. Compared to that of the exciton-SSC the plexciton-SSC does register a smaller $J_{SC}$ and $V_{OC}$ when deposition time is < 30 s. This is attributed to the small size of the Au nanoparticles and possible

resonance off-set between the plasmon and exciton. (c) Maximal power comparisons of plexciton-SSCs (red line) and plasmon-SSCs (black line) showing that the maximum power increases by ~180% in the case of the plexciton-SSC due to the Fano resonance between the Chl molecules and the Au nanoparticle film. On the other hand, another plexcitonic complex involving Rhodamine Blue molecules with Au nanoparticle films do not experience the same optimization due to an absence in explicit signature of a Fano resonance. Reprinted with permission from Ref.[72] Copyright Royal Society of Chemistry (2016).

As such, there is a growing interest in the field to identify photoactive materials that are capable of plexcitonic coupling and their effective translation toward electrical performance. Several research groups have found that J-aggregate dyes, whose structure resemble organic semiconductors used in solar cells today, are capable of plexcitonic coupling.[155, 194]

Symonds et al.[195] found evidence of strong coupling at room temperature between a surface plasmon and an exciton from a layered two-dimensional perovskite type semiconductor spin coated onto a silver film in an organic-inorganic hybrid architecture (Fig. 32, Left). Symonds et al.[195] note how the strong coupling regime leads to the formation of plexciton states, or mixed plasmon/exciton states, involving high and low energy polaritonic branches. Definitive and quantitative proof of strong coupling is determined from the observation of an anticrossing with a Rabi splitting of 167 meV observed in the dispersion lines resulting from reflectometry experiments performed at room temperature in the Kretschmann geometry (Fig. 32, Right).[2]

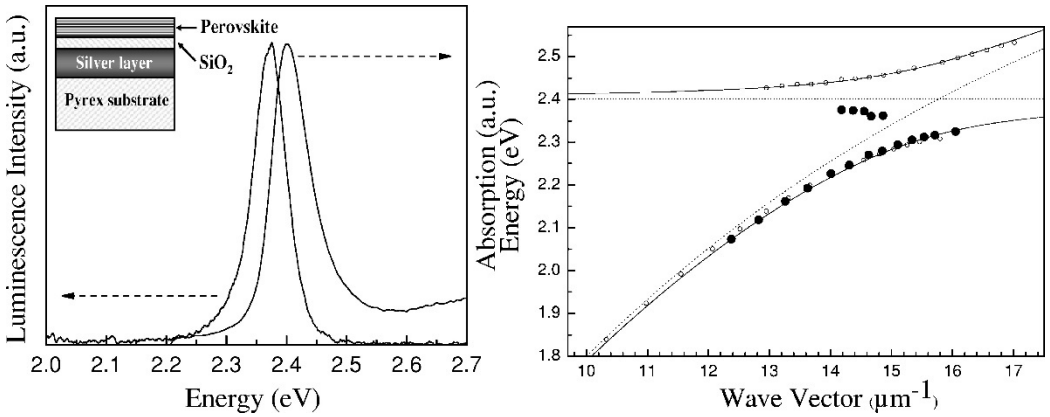


**Fig. 32 Emission of plexcitonic states.** (Left) Absorption and emission spectra at room temperature of the perovskite layer deposited onto a glass substrate. A layout of the sample is provided in the inset. A clear absorption peak is evident at 2.402 eV and is attributed to the excitons formed in the inorganic layers.[195] The emission spectrum also presents a Stokes shift of 31 meV compared to the absorption spectrum matching previous measurements on similar types of materials. (Right) Reflectometry energy (empty circles) is observed to decrease as a function of the wave vector. An anticrossing between the dispersion lines appears, providing characterization of the strong coupling that occurs between the surface plasmon of the metallic Ag, and the excitonic perovskite. Dotted lines represent the energy of the uncoupled plasmon and exciton, and the solid lines are the calculated polaritonic dispersion branches. Black circles indicate the positions in energy of the luminescence peaks. Reprinted with permission from Ref.[195] Copyright AIP Publishing (2007).

Balci et al.[184] discovered that the plexciton coupling strength could be tuned by the altering the concentration of the photoactive material. This was achieved by controlling the number of dye molecules adsorbed upon metallic nanoparticles which has a significant influence on the magnitude of Rabi splitting energy, an indicator of the strength of the coupling between the plasmonic nanoparticles and dye molecules, that is fundamental to obtaining hybrid metal-organic plexcitonic nanostructures with tunable optical properties in the visible spectrum (Fig. 33a).

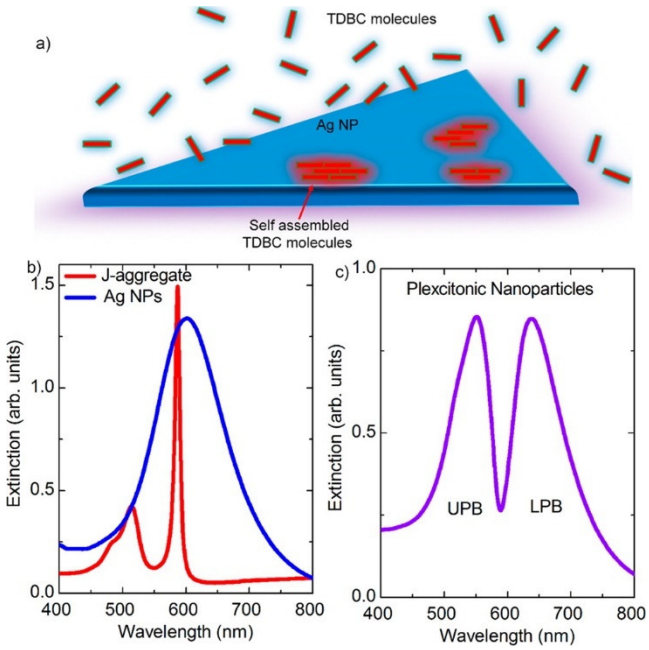


**Fig. 33 TDBC-Ag NP Plexcitonic System.** (a) Schematic representation of the self-assembly process involving TDBC dye molecules on an Ag NP. (b) Extincation spectra of Ag NPs and 0.1 mM TDBC, the self-assembled J-aggregate, in aqueous solution. The localized surface plasmon resonance of the Ag NPs is observed at around 600 nm while the broad absorbance peak around 513 nm is attributed to the TDBC monomer, and the sharp absorbance peak at 587 nm coming from the aggregated TDBC molecules. (c) Plexcitonic coupling and nanoparticle formation in the system is identified by the signature Rabi splitting of energies in the exctinction spectrum following the self-assembly of the individual TDBC molecules on the Ag NPs in an aqueous solution. Two new polariton branches, an upper polariton branch (UPB) and a lower polariton branch (LPB), are formed. Reprinted with permission from Ref.[184] Copyright American Chemical Society (2016).

By adjusting the concentration of dye molecules used in a unique synthesis of plexcitonic nanoparticles, Balci et al.[184] are able to control the number of dye molecules involving a cyanine dye, (5,5',6,6'-tetrachlorodi(4-sulfobutyl)-benzimidazolocarbocyanine (TDBC) self-assembled on Ag nanoprisms (Ag NPs) (Fig. 34a). These individual dye molecules self-assemble into J-aggregates on the Ag NPs forming a plexcitonic system identified by the inherent Rabi splitting of energies that is observed in the corresponding extinction spectra. The tunability of the

plexcitonic system is further confirmed by considering the extinction spectra of the Ag NPs synthesized with varying concentrations of TDBC molecules resulting in the observation of a transition from the weak to the ultrastrong coupling regime (Fig. 34b).

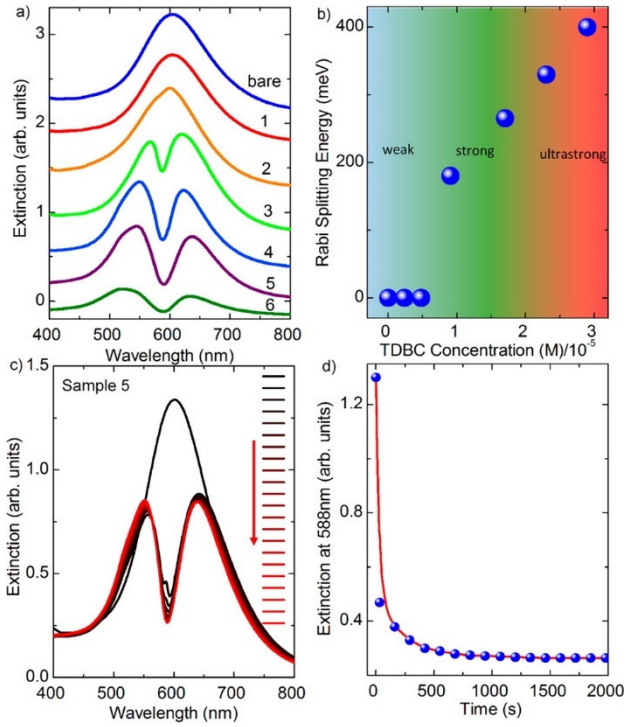


**Fig. 34 Tuning the Ag NP – TDBC plexcitonic System.** (a) Extinction spectra of Ag NPs when synthesized with increasing concentrations of TDBC molecules (by varying the volume, while the concentration of TDBC remains at 0.1 mM) in the aqueous solution from samples 1 to 6. The notable shifts in the Rabi splitting energy wavelengths and peaks directly provide proof of the plexcitonic system's tunability. (b) The Rabi splitting energy magnitudes are observed to increase with the concentration of TDBC molecules displaying a gradual transition from the weak to the ultra-strong coupling regime. (c) The kinetics of the J-aggregate formation of the surface of the Ag NPs is studied. The extinction spectra of sample 4 as a function of time is shown in with each spectrum being taken after ~ 2 min. (d) The plot of the extinction at 587 nm vs. time for the sample 4 presents proof of the formation of the plexcitonic nanoparticles in less than a few minutes. Reprinted with permission from Ref.[184] Copyright American Chemical Society (2016).

In a similar fashion, researchers have also shown that CdSe nanorods capped with Au or Pt beads are able to undergo ultrafast charge separation[196] where the CdSe phase transfers between 90% and 60% of hot electrons (and 80 % and 100 % of cold or Drude electrons) to the Pt or Au ends, respectively. The dynamics of the photoexcited charge carriers in CdSe/Au and CdSe/Pt nanorods were probed using ultrafast spectroscopy. It was upon photoexcitation at the 400 nm wavelength that Yu et al.[196] found that the results showed both hot and cold electron transfer from CdSe to the metal component. While the injection of the photoinduced electrons into the Au tip was observed to be faster than that into the Pt nanoparticles, only Pt could completely extract the excited electrons from the CdSe nanorod (Fig. 35).[196]

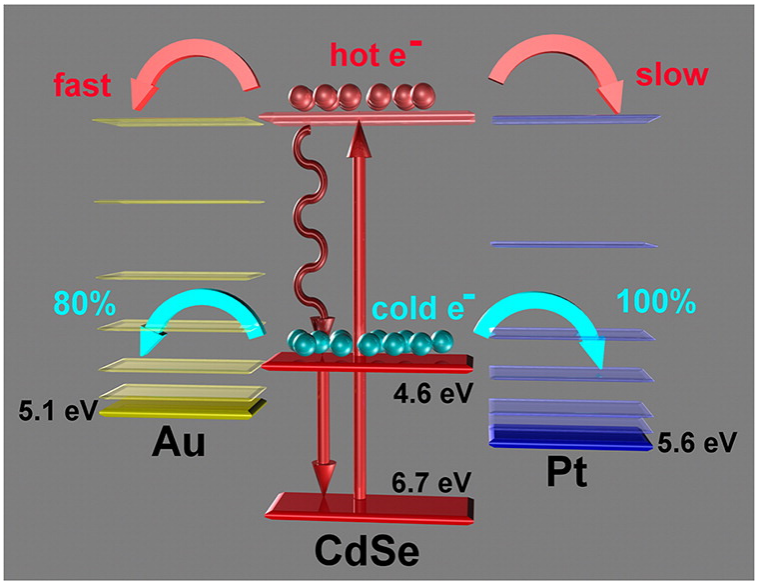


**Fig. 35 Schematic representation of the band alignment and charge transfer mechanisms of CdSe/Au and CdSe/Pt nanorods.** By combining temperature-dependent photoluminescence spectra, Yu et al.[196] demonstrate that the migration of photogenerated charge carriers can be ascribed to the band alignment dynamics and the charge storage/discharge behavior of the metallic components. In the schematic seen above, 400 nm photoexcitation has excess energy above the conduction band edge of the CdSe rod. Thus hot electrons/holes release this excess energy and move to the bottom of the conduction band via intraband relaxation. This charge separation is further enhanced by the presence of

the Au and Pt components by way of fast hot and cold electron transfer. Following the cold electron transfer, 20% of the photoexcited charge carriers still remain in the CdSe/Au over a nanosecond timescale, while CdSe/Pt results in an optimal extraction of all the electrons in the CdSe rod. Reprinted with permission from Ref.[196] Copyright American Chemical Society (2013).

Though it would seem a simple logical progression that current organic and hybrid photovoltaics would prove capable of being converted to plexcitonic solar cells, plexcitonic systems are not without their own shortcomings. Independent groups have found that when the exciton producing material is in close proximity to metallic nanoparticles, exciton lifetimes are decreased due to the presence of additional decay pathways where the exciton may either annihilate producing a surface plasmon[191] or undergo resonant electron transfer to the metal,[197-199] the former process being a source of photocurrent loss and the latter being useful when transfer to the metal phase is the desired outcome. Li et al.[200] found that the amount of surface plasmon production was tunable when using a core-shell structure. The authors encapsulated a CdSe/ZnS QD with $Al_2O_3$ shells of varying thickness and found that a thickness of 35 nm was the best at suppressing SP production (Fig 36).

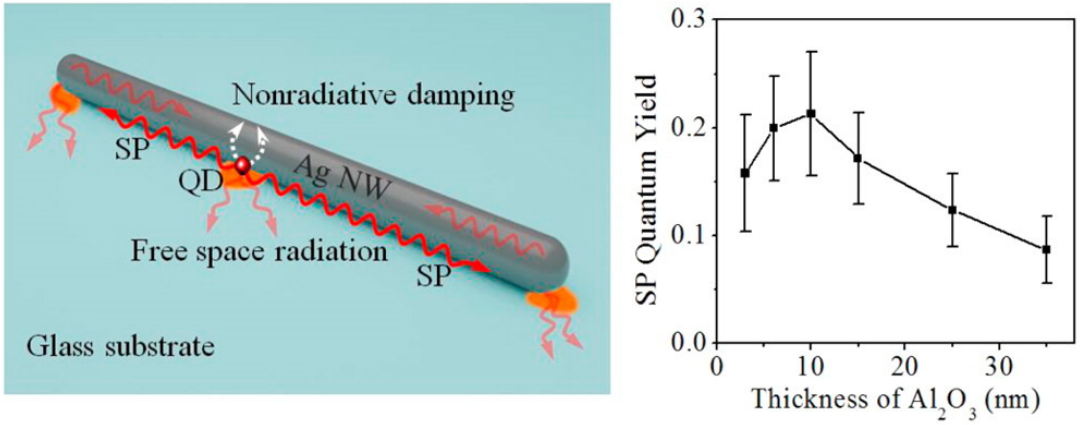


**Fig. 36 CdSe/ZnS Quantum Dots Coupled with Ag Nanowire.** The interactions between surface plasmons (SPs) in metal nanostructures and excitons in quantum dots (QDs) are of great interest for

applications that are strongly dependent on the quantum yield of SPs. Li et al.[200] utilize the SP guiding property of the nanowire as a means to measure the decay rates of all the exciton recombination channels i.e. direct free space radiation, SP generation, and nonradiative damping. This is achieved by encapsulating the CdSe/ZnS QDs with $Al_2O_3$ (Left) shells of varying thicknesses where thicknesses of 35 nm and 10 nm result in minimum and maximum SP quantum yields from the different distance-dependent decay rates of the three identified decay channels (Right). Reprinted with permission from Ref.[200] Copyright American Chemical Society (2015).

This shows that there may be a lower limit to the distance between plexcitonic materials to garner productive plexcitonic coupling. To avoid the close physical proximity of metal NPs to photoactive layers, both core-shell structures[190, 200] and insulating spacers such as $SiO_2$ have been employed.[201]

### 5.4 Plexcitonic Luminescence

The world's largest application of electroluminescence is in light emitting diodes (LEDs). LEDs have always been plagued by relatively low luminescence quantum yields and low outcoupling efficiencies due to which improving their efficiency has long been a focus of research.[202] Several studies have shown that plexcitonic coupling can modify the emission properties of fluorophores.[200-203] Specifically, it has been shown that plasmon-exciton coupled (plexcitonic) systems are capable of modifying and enhancing the emission rate of quantum dots (QDs)[204, 205], semiconductors,[206, 207] and organic dyes[208] both by factors of more than 10. Most notably, Okamoto et al.[209, 210] found that plexcitonic coupling between an Ag film and InGaN/GaN quantum wires displayed a 14-fold increase in PL than uncoupled samples. The authors were able to tune the strength of plexcitonic coupling by varying the thickness of the GaN spacer that separated the metal film from the InGaN quantum wells (QWs). Their experimental setup is shown schematically in (Fig. 37a). (Fig. 37b) shows the PL curve of the InGaN-metal coupled

systems when spaced 10 nm apart by the spacer. Al and Ag samples exhibited a PL intensity increase by factors of 8 and 14, respectively.

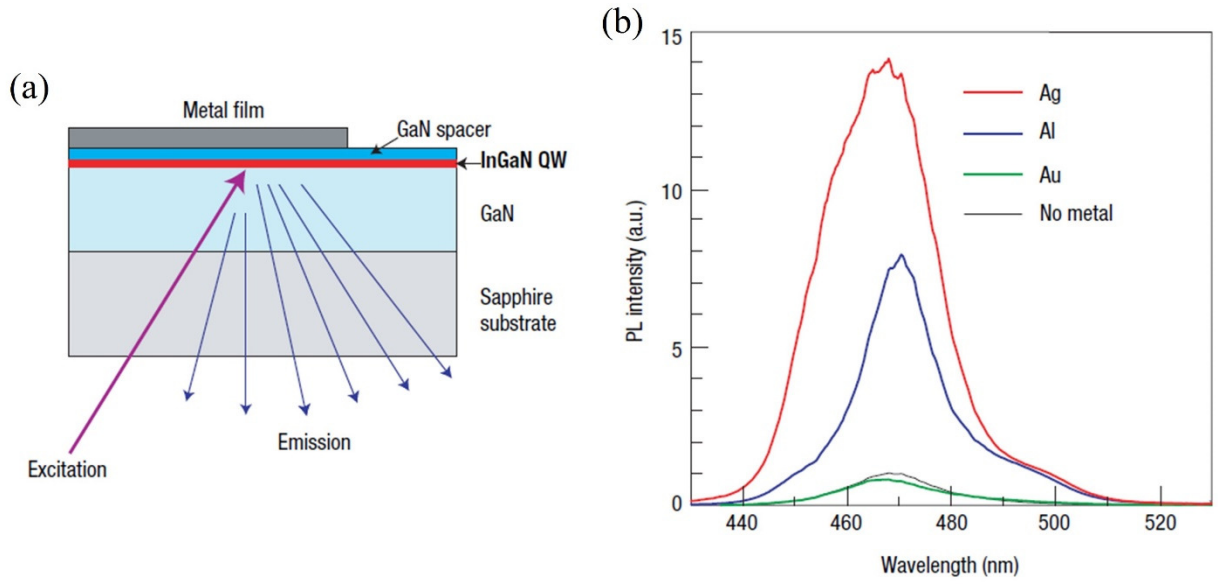


**Fig. 37** (a) Schematic of the structure of the plexcitonic LED where the metal film represents the plasmonic material, (b) Photoluminescence spectrum of the plexcitonic LEDs compared to the normal LED. The spectra of the normal LED has been normalized to 1. Reprinted with permission from Ref.[209] Copyright Nature Publishing Group (2004).

Nepal et al.[211] have shown a scalable, well-controlled and simple route to quantum dot (emitter) - Au nanorod (plasmonic units) architectures from solution using common solvents and organic compounds. By merely tailoring the molecular spacers, concentrations and reaction times, the group was able to alter the location and spacing of the QD coated Au nanorods. Furthermore, the system displayed a 5-times enhancement in photoluminescence compared to its non-plexcitonic analog (Fig. 38).[211]

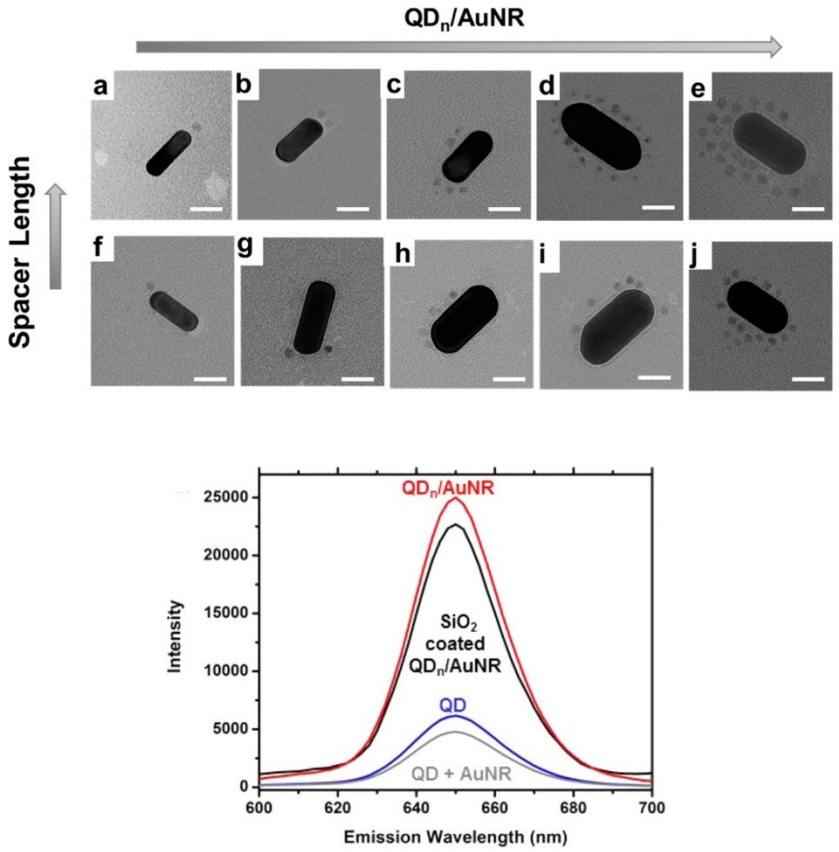


**Fig. 38** (Top) Structural control of spacing, position, and number of QDs per AuNR in QD-AuNR assemblies in aqueous solution. Spacing length is controlled by changing lignad length, while ligand position and the number of QDs per is controlled by incrementing QD concentration from 0.2 (a,b,f,g), 0.5, (c,h), 1.5 (d,i), and 2.5 nM (e,j) at 0.2 nM AuNR concentration. (Bottom) The subsequent photophysical properties of QDn/AuNR in aqueous solution and on a glass surface, confirming the fact that the plexcitonic counterpart to the QD/AuNR system produces a 5-times photoluminescence enhancement as opposed to its non-plexcitonic analogs. Adapted and reprinted with permission from Ref.[211] Copyright American Chemical Society (2013).

Similarly, in 2010 Fujiki et al.[212] constructed an $Alq_3$ (tris(8-hydroxylquinolianato) aluminum (III)) based OLED structure in which Au NPs were embedded in the hole transport layer. The structure of their device is shown below in (Fig. 39a). By tuning the thickness of the hole transport layer, the authors were able to tune the plexcitonic coupling between the Au NPs

and the excitons formed in the emissive layers. (Fig. 39b) displays the electroluminescence spectrum with respect to current density for both the normal and the plexcitonic devices, denoted as Normal-D (or OLED) and Surface-Plasmon Coupled Emission OLED (SPCE-D), respectively. As observed in (Fig. 39b), the emission intensity of the SPCE-D system increases sharply at a current density value of 2 $mA/cm^2$ as opposed to the Normal-D system. The plexcitonic LED demonstrated a 20-fold increase in IQE (internal quantum efficiency) where the value of the IQEs for the SPCE-D and the Normal-D systems at 15 V were estimated to be approximately $1.7 \times 10^{-6}$ and $8.7 \times 10^{-8}$, respectively.[212] By obtaining the onset voltages of emissions and the emission spectra for Normal-D and SPCE-D, Fujiki et al.[212] are able to clarify the mechanism behind the enhancement effect. The onset voltages of the two samples are found to be 11.5 V for both, indicating that the presence of Au nanoparticles does not influence the charge injection efficiency. Rather, the effect of SPCE in improving the emission efficiency in the OLED structure is attributed to the enhancement of OLED emissive sites. These sites prove to be locations where high densities of excitons are localized within several nanometers from the interface between the hole and electron transport layers[213] via coupling with localized surface plasmons from the Au nanoparticles.[212]

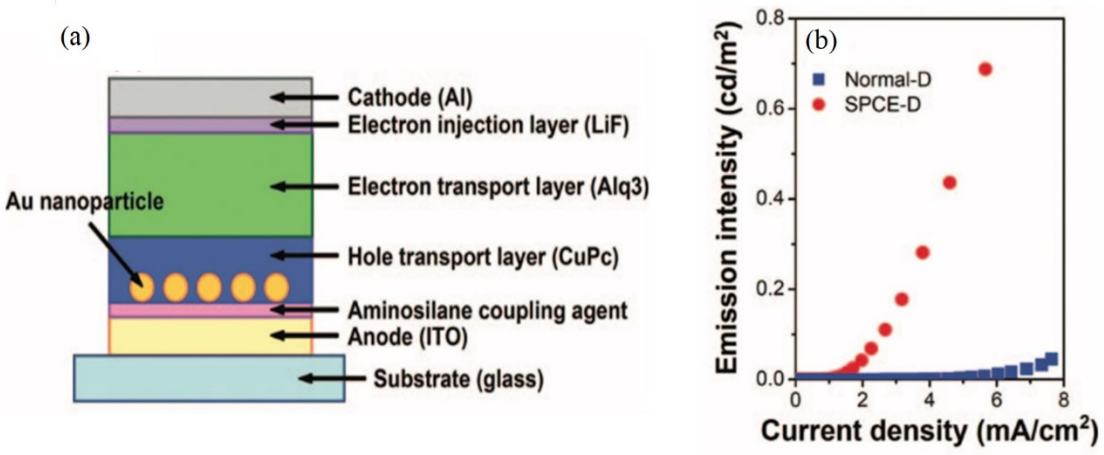

**Fig. 39** (a) Schematic of the plexcitonic OLED structure, (b) Emission intensity as a function of current density for the normal and plexcitonic OLEDs denoted by Normal-D and SPCE-D respectively. Reprinted with permission from Ref.[212] Copyright AIP Publishing (2010).

A few interesting approaches have been taken to harnessing plexcitonic coupling for efficient light-emission purposes. In 2012, Lawrie et al.[214] demonstrated that by varying simple parameters of a plasmonic array such as the pitch (center-to-center distance) and particle edge distances, one could vary the strength of the plexcitonic coupling and thus shift the color of emitted light even into the elusive near-UV spectrum (Fig. 40).

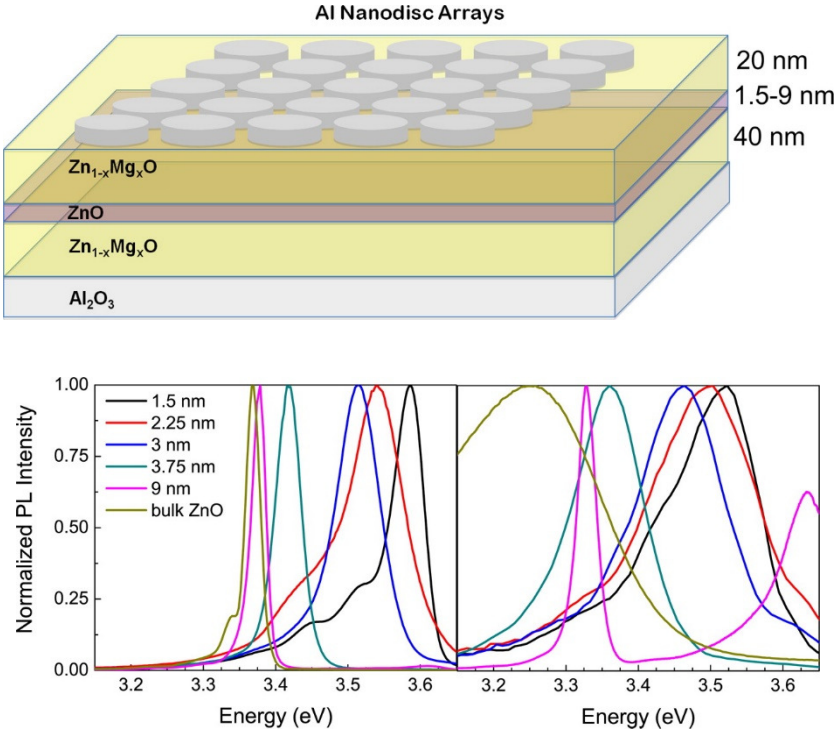


**Fig. 40** (Top) Schematic of the ZnO single quantum wells (SQWs) covered with Al nanoparticle (60-91 nm in diameter) arrays with an array pitch of 150 – 450 nm. (Bottom) The normalized SQW photoluminescence spectra acquired at T = 15 K (Left) and at room temperature (Right) for varying well widths of 1.5-9nm and for bulk (500 nm) ZnO, illustrating tuning of the emitted light along the near-UV spectrum. Adapted and reprinted with permission from Ref.[214] Copyright American Chemical Society (2012).

Taking the application of tunable heterostructures even further, Eizner et al.[215] were able to create Al nanoarrays that coupled with J-aggregates. This makes use of both an inexpensive metal and an organic semiconductor. The group also found enhanced absorbance and photoluminescence was possible across a range of wavelengths by simply tuning the parameters of the Al array. The authors varied the diameter of the disk-shaped NPs and the length and width of the pill-shaped NP as well as the center-to-center distance (pitch) in order to access the entire visible spectrum as well as portions of the UV spectrum. Potentially, LEDs or OLEDs of nearly any color could be produced by simply altering the metal nanoarrays coupled to the same basic diode structure. Finally, Eizner et al.[215] were able to create polarized light sensitive arrays. These arrays would luminesce either visible or UV light based on the direction of polarization of the incident light. (Fig. 41) shows the important array parameters as well as SEM and optical images of the plexcitonic systems.

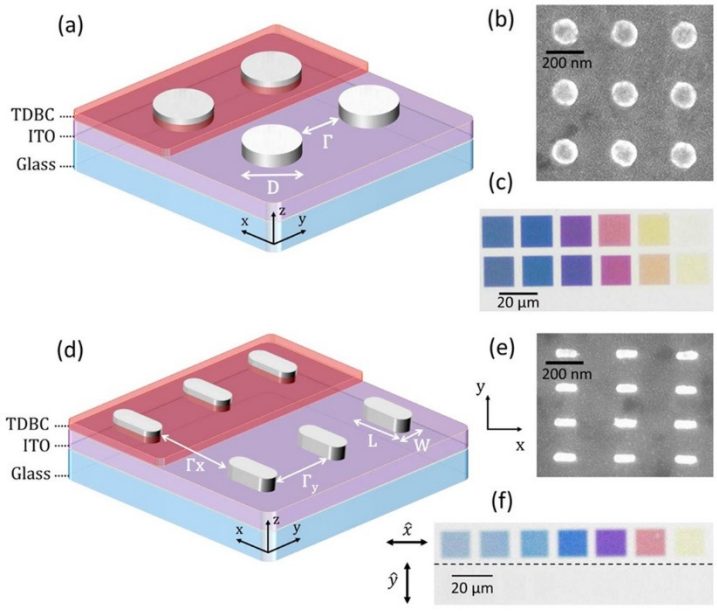


**Fig. 41** (a) Schematic of the disk-shaped Al NPs embedded in the TDBC dye layer, (b) SEM image of the disk-shaped array, (c) Transmission image of disk-shaped array sheets with varying Al NP diameters, (d)

Schematic of the pill-shaped Al NPs embedded in the TDBC dye lay, (e) SEM image of the disk-shaped array, (f) Transmission image of pill-shaped NP array sheets with varying Al NP length and width. The top of set of slides are illuminated by light polarized in the denoted x-plane while the bottom set are illuminated by light polarized in the y-plane. Reprinted with permission from Ref.[215] Copyright American Chemical Society (2015).

As mentioned in the previous section, quenching can be a concern when photoactive molecules are in extremely close proximity to metal NPs. In 2006, Anger et al.[205] measured the dependence of the fluorescence intensity for a single molecule of nile blue dye in the presence of a gradually approaching Au nanosphere. A maximal fluorescence intensity was achieved when the molecule was placed at a distance ~ 5 nm away from the surface of the Au nanosphere. It is understood that as the molecule is moved toward the surface of the metal nanosphere, the molecule experiences an exponentially increasing local electric field intensity leading to a continuous increase in its excitation rate, thus indicating that the fluorescence intensity is a synergistic result of the excitation rate enhancement and the modification of the overall quantum yield. On the other hand, fluorescence quenching is found to occur when the spacing is roughly less than 5 nm.[205] Anger et al.[205] also emphasize that the relative dipole orientations of the fluorophore and plasmonic nanocrystal are very important for enhanced fluorescence as both the excitation and emission enhancements are strongly dependent on the molecular dipole orientation relative to the polarization of the electric field.

In comparison, as shown earlier, Li et al.[200] found that optimum PL intensity for a CdSe/ZnS QD was achieved when it was placed 35 nm from an Ag NW. The distances between the QD and NW were achieved by encapsulating the QD with an $Al_2O_3$ layer. It should be noted that the discrepancy could be accounted for since significantly different materials were used in either study. Another representative study of similar nature is done by Liu et al.[216] who studied

the effect of plasmonic Pt NPs concentrations on a colloidal $CsPbBr_3$ perovskite structure semiconductor NPs discovering photoluminescence (PL) quenching and exciton lifetime lengthening at higher Pt NP concentrations. The PL lifetimes of the colloidal $CsPbBr_3$ semiconductor nanoparticles were extended from 17.7 ns to 30.8 ns. This is a beneficial property favoring the catalytic function of the semiconductor component of the composite structure, as it extends exciton lifetime, further increasing the probability of charge transfer to an adsorbed surface catalyst which will be of great application in solar cells as a longer lifetime allows more time for charge separation to occur. Finally, while surface plasmons can be a large source of inefficiency in OLEDs, Hobson et al.[202] found that plexcitonic arrays on OLED materials can be used to recover that lost energy. Since then, OLEDs incorporating periodic Au NP arrays have even been found to increase luminescence intensity more than 10-fold.[217]

In this manner, these representative studies present the great potential there is in incorporating plexcitonics for advanced applications in optical enhancement, OLEDs, and fluorescence spectroscopy.

## 6. Perspective on Future Work

Despite the myriad applications that have been brought forward to demonstrate the exciting potential of plexcitonic systems for photocatalysis, photovoltaics, and luminescence, the detailed mechanisms of plasmon-exciton interactions as observed in these hybrid and composite nanomaterials are yet to be fully understood. For example, in the case of plasmon-graphene co-driven chemical reactions, we have yet to get a complete picture of the ultrafast dynamical processes that result in the transference of plasmon-induced hot electrons to graphene. In fact, the very basic nature and reason behind the higher efficiencies of catalytic reactions as well as the damping processes evidenced in these hybrid systems, eludes our current understanding, and

while various theoretical and experimental approaches have contested these questions, a consistent framework is yet to emerge bridging the physics behind plasmons and excitons. [33, 75, 149, 156, 218-220] Moving forward, this is a significant challenge that must be tackled in gaining access to a greater understanding of plexciton dynamics, and the exploitation of said quasiparticles in various nanotechnological applications.

Altogether, the study of plexcitonics offers a wide range of opportunities to learn and control light-matter interactions and electromagnetic energy at the nanoscale. Among various other systems, plexcitonic hybrid metal-semiconductor nanostructures hold great promise in their contribution to understanding the behavior of strong and weak coupling, two physical processes, at the core of various nanophotonic phenomena. Light-matter coupling, and more precisely, strong coupling, is a phenomenon that connects material science with quantum electrodynamics. This not only offers us the possibility to mold and monitor material and molecular properties through the hybridization of the quantum field, essentially designing quasi-particles, but also assists the development of novel complex materials such as high-temperature superconductors, photocatalysts, and topological materials etc.[74] By controlling the interactions between the vacuum field and material oscillators, strong coupling would enable us to govern biological dynamics, and quantum mechanical processes such as chemical reactivity, phase transitions, and spectroscopy etc. This will assist toward the fabrication of exotic devices in nanoscale optics and photonics all the while bridging the fields of physics, chemistry, and engineering. Further investigations on the practical applications of strong coupling could be made by considering systems that increase the coupling strength and allow the coupled system to interact with surrounding media. An example would involve systems consisting of ensembles of emitters separately coupled to plasmonic cavities.[221]

While various linear optical properties have been studied and utilized extensively in diverse relevant applications, plexcitonic hybrid nanostructures open the venue towards exploring nonlinear optical properties that can be utilized for optical switching, amplification, and regulation of light-matter interactions at the nanoscale.[132] Ultrafast probe studies of plexcitonic interactions will help optimize the design of potential plexcitonic nanostructures with ultrafast functionalities. The potential of plexcitonic systems is vast. The interactions between plasmons and excitons in semiconductor nanostructures can be harnessed for their complementary advantages such as prolonged lifetime of excitons in semiconductor nanostructures and enhanced quantum yields and performance efficiencies in various optoelectronic devices ranging from light emitting diodes to solar cells as well as semiconductor photocatalytic systems. Plexcitonics, in its inherent matter-light hybridization regimes of strong and weak coupling also contribute to venues for potential development and optimization of applications such as low-threshold lasers, biomedical detection techniques, and quantum information processing methods.

Moving forward, challenges remain in both experimental and theoretical aspects of the field. It will be necessary to develop a theoretical framework under which the intrinsic losses observed in plexcitonic systems can be addressed as well as provide alternatives in gain structures that can be integrated. Methods must also be developed to sustain surface plasmon resonance and exciton dipole strengths for efficient plexcitonic interactions. The study of surface properties will be crucial to understanding the origin of strong and weak plexciton interactions.[132] Even more so, many quantum properties of surface plasmons are yet to be fully explored and there still remain huge obstacles to fully realizing functioning and reliable quantum devices that take advantage of plasmonics. This concurrently applies for plexcitonics which is, in

essence, the amalgamation of plasmons and excitons. Most importantly, as we consider the miniaturization of said hybrid systems, we must bring into question the current quantization methods, largely macroscopic in their approach, and their applicability in the microscale. One such consideration would involve the requirement of density functional theory combined with quantum optics and plasmonics. Much of this can also be supplemented by numerical simulations that can provide insights toward the electromagnetic phenomena involved in the interaction of light and matter at the diverse length scales encountered in various plexcitonic applications.

## 7. Conclusion

This review provides a survey of the current research in the field of plexcitonics. Plexcitons are quasiparticles used to describe the interactions of two other quasiparticles – plasmons and excitons. In the strong coupling regime, plexcitonic systems are characterized by a large Rabi splitting in their optical spectra while in the weak coupling regime, plexcitonic interactions modify the intensity of optical absorption and the rate of spontaneous emission. Nanofabrication and materials chemistry are important in engineering nanoscale configurations wherein discrete metal nanoparticles or arrays of noble metal nanoparticles are found in close proximity with excitonic absorbers and/or emitters to achieve the requisite degree of coupling. The plexcitonic coupling of noble metal surface plasmons with excitons in 2D semiconductor sheets such as graphene, reduced graphene oxide and transition metal dichalcogenides have been used to demonstrate a synergistic enhancement in the rate of surface photocatalytic reactions. Various binary and recently established ternary nanocomposites of graphene and noble metal nanoparticles have been used to display improved visible-light absorption and enhancement effects, resulting in the utilization of the full spectrum of solar energy and the generation of

energetic charge carriers promoting excellent photocatalytic systems while foregoing losses via transfer and recombination processes. In strongly emissive organic semiconductor films, III-V nanowires and II-VI quantum dots, plexcitonic coupling has been used to shift the emission wavelength of light emitting devices, achieve enhanced photoluminescence and electroluminescence, and demonstrate polarization sensitivity. Diverse photovoltaic architectures involving plasmon-SSCs, exciton-SSCs, and their analysis have set the stage for the optimization of hybrid plexciton-SSCs translating towards efficient electrical performance. The great potential of plexcitonic applications notwithstanding, challenges remain in the road ahead to provide for the extensive commercialization of said devices. Alongside theoretical developments to shed light on the coupling mechanics involved in plexcitonic applications, the advancement of novel fabrication techniques as well as ultrafast probing methods, the experimental functionalities of plexcitonic nanostructures can be further optimized for better control of optical properties and energy flow for diverse applications in optoelectronics.

## Conflicts of Interest

There are no conflicts of interest to declare.

## Acknowledgements

All authors thank NSERC and University of Alberta Future Energy Systems for financial support.

### References

1. L. Novotny, *Principles of nano-optics*, Cambridge University Press, New York, 2012.
2. S. A. Maier, *Plasmonics : fundamentals and applications*, Springer, New York, 2007.
3. M. Sukharev and A. Nitzan, *J. Phys. Condens. Matter*, 2017, **29**, 443003.
4. S. I. Pekar, *J. Phys. Chem. Solids*, 1958, **5**, 11-22.
5. E. Cao, W. H. Lin, M. T. Sun, W. J. Liang and Y. Z. Song, *Nanophotonics*, 2018, **7**, 145-167.
6. T. Low, A. Chaves, J. D. Caldwell, A. Kumar, N. X. Fang, P. Avouris, T. F. Heinz, F. Guinea, L. Martin-Moreno and F. Koppens, *Nat. Mater.*, 2016, **16**, 182.

7. J. Yuen-Zhou, S. K. Saikin, T. Zhu, M. C. Onbasli, C. A. Ross, V. Bulovic and M. A. Baldo, *Nat. Commun.*, 2016, **7**, 11783.
8. N. T. Fofang, T. H. Park, O. Neumann, N. A. Mirin, P. Nordlander and N. J. Halas, *Nano Lett.*, 2008, **8**, 3481-3487.
9. J. Frenkel, *Phys. Rev.*, 1931, **37**, 17-44.
10. W. Y. Liang, *Phys. Educ.*, 1970, **5**, 226.
11. M. Dresselhaus, G. Dresselhaus, S. B. Cronin and A. Gomes Souza Filho, in *Solid State Properties: From Bulk to Nano*, Springer Berlin Heidelberg, Berlin, Heidelberg, 2018, pp. 411-441.
12. J. F. Muth, J. H. Lee, I. K. Shmagin, R. M. Kolbas, H. C. C. Jr., B. P. Keller, U. K. Mishra and S. P. DenBaars, *Appl. Phys. Lett.*, 1997, **71**, 2572-2574.
13. A. M. Askar and K. Shankar, *J. Nanosci. Nanotechnol.*, 2016, **16**, 5890-5901.
14. S. M. Menke and R. J. Holmes, *Energ. Environ. Sci.*, 2014, **7**, 499-512.
15. R. Kisslinger, W. Hua and K. Shankar, *Polymers*, 2017, **9**, 35.
16. S. A. March, D. B. Riley, C. Clegg, D. Webber, X. Liu, M. Dobrowolska, J. K. Furdyna, I. G. Hill and K. C. Hall, *ACS Photonics*, 2017, **4**, 1515-1521.
17. S. Blumstengel, S. Sadofev, C. Xu, J. Puls and F. Henneberger, *Phys. Rev. Lett.*, 2006, **97**, 237401.
18. J. R. Schaibley, H. Yu, G. Clark, P. Rivera, J. S. Ross, K. L. Seyler, W. Yao and X. Xu, *Nat. Rev. Mater.*, 2016, **1**, 16055.
19. E. C. Le Ru, *Principles of surface-enhanced Raman spectroscopy and related plasmonic effects*, Elsevier, Amsterdam 1st ed. edn., 2009.
20. M. Wang, M. Ye, J. Iocozzia, C. Lin and Z. Lin, *Adv. Sci.*, 2016, **3**, 1600024.
21. A. W. Wark, H. J. Lee and R. M. Corn, *Anal. Chem.*, 2005, **77**, 3904-3907.
22. M. E. Stewart, C. R. Anderton, L. B. Thompson, J. Maria, S. K. Gray, J. A. Rogers and R. G. Nuzzo, *Chem. Rev.*, 2008, **108**, 494-521.
23. M. J. Kale, T. Avanesian and P. Christopher, *ACS Catal.*, 2014, **4**, 116-128.
24. M. Rycenga, C. M. Cobley, J. Zeng, W. Li, C. H. Moran, Q. Zhang, D. Qin and Y. Xia, *Chem. Rev.*, 2011, **111**, 3669-3712.
25. Y. B. Zheng, B. K. Juluri, L. Lin Jensen, D. Ahmed, M. Lu, L. Jensen and T. J. Huang, *Adv. Mater.*, 2010, **22**, 3603-3607.
26. S. Balci, *Opt. Lett.*, 2013, **38**, 4498-4501.
27. C. Symonds, C. Bonnand, J. Plenet, A. Bréhier, R. Parashkov, J. Lauret, E. Deleporte and J. Bellessa, *New J. Phys.*, 2008, **10**, 065017.
28. K. Wu, W. E. Rodríguez-Córdoba, Y. Yang and T. Lian, *Nano Lett.*, 2013, **13**, 5255-5263.
29. W. Liu, B. Lee, C. H. Naylor, H.-S. Ee, J. Park, A. T. C. Johnson and R. Agarwal, *Nano Lett.*, 2016, **16**, 1262-1269.
30. D. Zheng, S. P. Zhang, Q. Deng, M. Kang, P. Nordlander and H. X. Xu, *Nano Lett.*, 2017, **17**, 3809-3814.
31. M. Wang, A. Krasnok, T. Zhang, L. Scarabelli, H. Liu, Z. Wu, L. M. Liz-Marzán, M. Terrones, A. Alù and Y. Zheng, *Adv. Mater.*, 2018, **30**, 1705779.
32. T. Ozel, P. L. Hernandez-Martinez, E. Mutlugun, O. Akin, S. Nizamoglu, I. O. Ozel, Q. Zhang, Q. H. Xiong and H. V. Demir, *Nano Lett.*, 2013, **13**, 3065-3072.
33. A. Manjavacas, F. J. G. D. Abajo and P. Nordlander, *Nano Lett.*, 2011, **11**, 2318-2323.
34. Y. Fedutik, V. V. Temnov, O. Schops, U. Woggon and M. V. Artemyev, *Phys. Rev. Lett.*, 2007, **99**, 4.
35. J. Bellessa, C. Bonnand, J. C. Plenet and J. Mugnier, *Phys. Rev. Lett.*, 2004, **93**, 036404-036401.
36. E. Thoms, P. Sippel, D. Reuter, M. Weiß, A. Loidl and S. Krohns, *Sci. Rep.*, 2017, **7**, 7463.
37. M. F. García-Sánchez, J. C. M'Peko, A. R. Ruiz-Salvador, G. Rodríguez-Gattorno, Y. Echevarría, F. Fernández-Gutierrez and A. Delgado, *J. Chem. Educ.*, 2003, **80**, 1062-1073.

38. J. B. Theeten and D. E. Aspnes, *Annu. Rev. Mater. Sci.*, 1981, **11**, 97-122.
39. P. Drude, *Ann. Phys. (Berl.)*, 1900, **306**, 566-613.
40. P. Drude, *Ann. Phys. (Berl.)*, 1900, **308**, 369-402.
41. N. W. Ashcroft and N. D. Mermin, *Solid state physics*, Holt, Rinehart and Winston, New York, 1976.
42. U. Kreibig and M. Vollmer, *Optical properties of metal clusters*, Berlin; New York: Springer, 1995.
43. A. D. Rakić, M. L. Majewski, A. B. Djurišsić and J. M. Elazar, *Appl. Opt.*, 1998, **37**, 5271-5283.
44. D. Sarid and W. A. Challener, *Modern introduction to surface plasmons : Theory, Mathematica modeling, and Applications*, Cambridge; New York: Cambridge University Press, 2010.
45. J. Gersten and A. Nitzan, *J. Chem. Phys.*, 1980, **73**, 3023-3027.
46. M. Moskovits, *J. Raman Spectrosc.*, 2005, **36**, 485-496.
47. T. Sen and A. Patra, *J. Phys. Chem. C*, 2012, **116**, 17307-17317.
48. T. Pal and S. K. Ghosha, *Phys. Chem. Chem. Phys.*, 2009, **11**, 3831-3844.
49. D. Melnikau, D. Savateeva, A. Susha, A. L. Rogach and Y. P. Rakovich, *Nanoscale Res. Lett.*, 2013, **8**, 2-6.
50. N. T. Fofang, T. H. Park, O. Neumann, N. A. Mirin, P. Nordlander and N. J. Halas, *Nano Lett.*, 2008, **8**, 3481-3487.
51. B. G. DeLacy, W. Qiu, M. Soljačić, C. W. Hsu, O. D. Miller, S. G. Johnson and J. D. Joannopoulos, *Opt. Express*, 2013, **21**, 19103-19103.
52. G. W. Ford and W. H. Weber, *Phys. Rep.*, 1984, **113**, 195-287.
53. R. Fuchs and R. G. Barrera, *Phys. Rev. B*, 1981, **24**, 2940-2950.
54. R. H. Dicke, *Phys. Rev.*, 1954, **93**, 99-110.
55. I. Pockrand, J. D. Swalen, R. Santo, A. Brillante and M. R. Philpott, *J. Chem. Phys.*, 1978, **69**, 4001-4011.
56. P. Törmä and W. L. Barnes, *Rep. Prog. Phys.*, 2015, **78**, 013901.
57. J. I. Gersten and A. Nitzan, *Chem. Phys. Lett.*, 1984, **104**, 31-37.
58. S. Saini, G. Srinivas and B. Bagchi, *J. Phys. Chem. B*, 2009, **113**, 1817-1832.
59. C. A. Marocico and J. Knoester, *Phys. Rev. A*, 2011, **84**, 053824.
60. C. A. Marocico and J. Knoester, *Phys. Rev. A*, 2009, **79**, 053816.
61. A. O. Govorov, J. Lee and N. A. Kotov, *Phys. Rev. B*, 2007, **76**, 125308.
62. G. Khitrova, H. M. Gibbs, M. Kira, S. W. Koch and A. Scherer, *Nat. Phys.*, 2006, **2**, 81.
63. H. M. Gibbs, G. Khitrova and S. W. Koch, *Nat. Photonics*, 2011, **5**, 273.
64. P. Lodahl, S. Mahmoodian and S. Stobbe, *Rev. Mod. Phys.*, 2015, **87**, 347-400.
65. A. O. Govorov, G. W. Bryant, W. Zhang, T. Skeini, J. Lee, N. A. Kotov, J. M. Slocik and R. R. Naik, *Nano Lett.*, 2006, **6**, 984-994.
66. V. N. Pustovit and T. V. Shahbazyan, *Phys. Rev. B*, 2010, **82**, 075429.
67. S. M. Sadeghi, *Phys. Rev. B*, 2009, **79**, 233309.
68. D. F. Walls, *Quantum Optics*, Springer, Berlin, 2008.
69. C. Boerigter, U. Aslam and S. Linic, *ACS Nano*, 2016, **10**, 6108-6115.
70. M. S. Tame, K. R. McEnery, Ş. K. Özdemir, J. Lee, S. A. Maier and M. S. Kim, *Nat. Phys.*, 2013, **9**, 329.
71. A. E. Miroshnichenko, S. Flach and Y. S. Kivshar, *Rev. Mod. Phys.*, 2010, **82**, 2257-2298.
72. F. Nan, S. J. Ding, L. Ma, Z. Q. Cheng, Y. T. Zhong, Y. F. Zhang, Y. H. Qiu, X. G. Li, L. Zhou and Q. Q. Wang, *Nanoscale*, 2016, **8**, 15071-15078.
73. S. Dufferwiel, S. Schwarz, F. Withers, A. A. P. Trichet, F. Li, M. Sich, O. Del Pozo-Zamudio, C. Clark, A. Nalitov, D. D. Solnyshkov, G. Malpuech, K. S. Novoselov, J. M. Smith, M. S. Skolnick, D. N. Krizhanovskii and A. I. Tartakovskii, *Nat. Commun.*, 2015, **6**, 8579.
74. B. Kolaric, B. Maes, K. Clays, T. Durt and Y. Caudano, *Adv. Quantum Technol.*, 2018, **0**, 1800001.

75. L. Novotny, *Am. J. Phys.*, 2010, **78**, 1199-1202.
76. S. Haroche and J. M. Raimond, *Exploring the Quantum : Atoms, Cavities and Photons*, Oxford ; New York : Oxford University Press, 2006.
77. A. E. Schlather, N. Large, A. S. Urban, P. Nordlander and N. J. Halas, *Nano Lett.*, 2013, **13**, 3281-3286.
78. N. I. Cade, T. Ritman-Meer and D. Richards, *Phys. Rev. B*, 2009, **79**, 241404.
79. B. H. Bransden and C. J. Joachain, *Introduction to Quantum Mechanics*, Harlow, Essex, England : Longman Scientific & Technical ; New York : Wiley, 1989.
80. B. H. Bransden and C. J. Joachain, *Physics of Atoms and Molecules*, London ; New York : Longman, 1983.
81. M. Pelton and Y. Yamamoto, *Phys. Rev. A*, 1999, **59**, 2418-2421.
82. H. Hapuarachchi, M. Premaratne, Q. L. Bao, W. L. Cheng, S. D. Gunapala and G. P. Agrawal, *Phys. Rev. B*, 2017, **95**, 12.
83. I. Bozhevolnyi Sergey and N. A. Mortensen, *Nanophotonics*, 2017, **6**, 1185.
84. H. Schmid, H. Biebuyck, B. Michel and O. J. F. Martin, *Appl. Phys. Lett.*, 1998, **72**, 2379-2381.
85. J. G. Goodberlet, *Appl. Phys. Lett.*, 2000, **76**, 667-669.
86. J. G. Goodberlet and H. Kavak, *Appl. Phys. Lett.*, 2002, **81**, 1315-1317.
87. O. J. F. Martin, N. B. Piller, H. Schmid, H. Biebuyck and B. Michel, *Opt. Express*, 1998, **3**, 280-285.
88. M. M. Alkaisi, R. J. Blaikie, S. J. McNab, R. Cheung and D. R. S. Cumming, *Appl. Phys. Lett.*, 1999, **75**, 3560-3562.
89. X. Luo and T. Ishihara, *Appl. Phys. Lett.*, 2004, **84**, 4780-4782.
90. M. D. Austin and S. Y. Chou, *Appl. Phys. Lett.*, 2002, **81**, 4431-4433.
91. P. Zijlstra, J. W. M. Chon and M. Gu, *Nature*, 2009, **459**, 410.
92. H. H. Pham, I. Gourevich, J. K. Oh, J. E. N. Jonkman and E. Kumacheva, *Adv. Mater.*, 2004, **16**, 516-520.
93. H. Ditlbacher, J. R. Krenn, B. Lamprecht, A. Leitner and F. R. Aussenegg, *Opt. Lett.*, 2000, **25**, 563-565.
94. N. Yasuro, U. Shinji, K. Miyuki and Y. Sunao, *Jpn. J. Appl. Phys.*, 2003, **42**, 1749.
95. X. Li, J. W. M. Chon, S. Wu, R. A. Evans and M. Gu, *Opt. Lett.*, 2007, **32**, 277-279.
96. D. Day, M. Gu and A. Smallridge, *Adv. Mater.*, 2001, **13**, 1005-1007.
97. S. Kawata and Y. Kawata, *Chem. Rev.*, 2000, **100**, 1777-1788.
98. K. Kalyanasundaram and M. Graetzel, *Curr. Opin. Biotechnol.*, 2010, **21**, 298-310.
99. G. Liu, L. Z. Wang, H. G. Yang, H. M. Cheng and G. Q. Lu, *J. Mater. Chem.*, 2010, **20**, 831-843.
100. H. L. Cui, W. Zhao, C. Y. Yang, H. Yin, T. Q. Lin, Y. F. Shan, Y. Xie, H. Gu and F. Q. Huang, *J. Mater. Chem. A*, 2014, **2**, 8612-8616.
101. M. M. Khan, S. A. Ansari, D. Pradhan, M. O. Ansari, D. H. Han, J. Lee and M. H. Cho, *J. Mater. Chem. A*, 2014, **2**, 637-644.
102. H. Xu, S. X. Ouyang, L. Q. Liu, P. Reunchan, N. Umezawa and J. H. Ye, *J. Mater. Chem. A*, 2014, **2**, 12642-12661.
103. M. Z. Ge, C. Y. Cao, J. Y. Huang, S. H. Li, Z. Chen, K. Q. Zhang, S. S. Al-Deyab and Y. K. Lai, *J. Mater. Chem. A*, 2016, **4**, 6772-6801.
104. P. Kar, S. Farsinezhad, N. Mahdi, Y. Zhang, U. Obuekwe, H. Sharma, J. Shen, N. Semagina and K. Shankar, *Nano Res.*, 2016, **9**, 3478-3493.
105. A. Kudo and Y. Miseki, *Chem. Soc. Rev.*, 2009, **38**, 253-278.
106. F. Wenguang and K. H. L. Michael, *Molecules*, 2016, **21**, 180.
107. Y.-H. Su, Y.-F. Ke, S.-L. Cai and Q.-Y. Yao, *Light Sci. Appl.*, 2012, **1**, e14.
108. S. Mukherjee, F. Libisch, N. Large, O. Neumann, L. V. Brown, J. Cheng, J. B. Lassiter, E. A. Carter, P. Nordlander and N. J. Halas, *Nano Lett.*, 2013, **13**, 240-247.

109. G. V. Hartland, L. V. Besteiro, P. Johns and A. O. Govorov, *ACS Energy Lett.*, 2017, **2**, 1641-1653.
110. Y. Shiraishi, N. Yasumoto, J. Imai, H. Sakamoto, S. Tanaka, S. Ichikawa, B. Ohtani and T. Hirai, *Nanoscale*, 2017, **9**, 8349-8361.
111. S. Mubeen, J. Lee, D. Liu, G. D. Stucky and M. Moskovits, *Nano Lett.*, 2015, **15**, 2132-2136.
112. S. J. Tan, A. Argondizzo, J. D. Ren, L. M. Liu, J. Zhao and H. Petek, *Nat. Photonics*, 2017, **11**, 806-812.
113. Z. Xuming, C. Yu Lim, L. Ru-Shi and T. Din Ping, *Rep. Prog. Phys.*, 2013, **76**, 046401.
114. G. E. Jellison, L. A. Boatner, J. D. Budai, B. S. Jeong and D. P. Norton, *J. Appl. Phys.*, 2003, **93**, 9537-9541.
115. S. Farsinezhad, S. P. Banerjee, B. Bangalore Rajeeva, B. D. Wiltshire, H. Sharma, A. Sura, A. Mohammadpour, P. Kar, R. Fedosejevs and K. Shankar, *ACS Appl. Mater. Inter.*, 2017, **9**, 740-749.
116. J. Schneider, M. Matsuoka, M. Takeuchi, J. Zhang, Y. Horiuchi, M. Anpo and D. W. Bahnemann, *Chem. Rev.*, 2014, **114**, 9919-9986.
117. J. Li and N. Wu, *Catal. Sci. Technol.*, 2015, **5**, 1360-1384.
118. J. Pan, X. Wu, L. Wang, G. Liu, G. Q. Lu and H.-M. Cheng, *Chem. Commun.*, 2011, **47**, 8361-8363.
119. W.-N. Wang, J. Park and P. Biswas, *Catal. Sci. Technol.*, 2011, **1**, 593-600.
120. A. Kongkanand, K. Tvrdy, K. Takechi, M. Kuno and P. V. Kamat, *J. Am. Chem. Soc.*, 2008, **130**, 4007-4015.
121. H. Li, Z. Bian, J. Zhu, Y. Huo, H. Li and Y. Lu, *J. Am. Chem. Soc.*, 2007, **129**, 4538-4539.
122. M. Sachs, E. Pastor, A. Kafizas and J. R. Durrant, *J. Phys. Chem. Lett.*, 2016, **7**, 3742-3746.
123. C. Clavero, *Nat. Photonics*, 2014, **8**, 95-103.
124. H. Wei, H. Xu, D. Ratchford, X. Li and C. K. Shih, *Nano Lett.*, 2009, **9**, 4168-4171.
125. P. Kar, S. Zheng, Y. Zhang, E. Vahidzadeh, A. Manuel, R. Kisslinger, K. Alam, U. Thakur, N. Mahdi, P. Kumar and K. Shankar, *Appl. Catal. B-Environ.*, 2018, DOI: https://doi.org/10.1016/j.apcatb.2018.08.002.
126. L. Zhou, X. Yu and J. Zhu, *Nano Lett.*, 2014, **14**, 1093-1098.
127. H. A. Atwater and A. Polman, *Nat. Mater.*, 2010, **9**, 205-213.
128. X. Wang, R. Long, D. Liu, D. Yang, C. Wang and Y. Xiong, *Nano Energy*, 2016, **24**, 87-93.
129. X. H. Wang, J. G. Li, H. Kamiyama, Y. Moriyoshi and T. Ishigaki, *J. Phys. Chem. B*, 2006, **110**, 6804-6809.
130. L. Shen, G. N. Gibson, N. Poudel, B. Hou, J. Chen, H. Shi, E. Guignon, N. C. Cady, W. D. Page, A. Pilar and S. B. Cronin, *Appl. Phys. Lett.*, 2018, **113**, 113104.
131. A. Sousa-Castillo, M. Comesaña-Hermo, B. Rodríguez-González, M. Pérez-Lorenzo, Z. Wang, X.-T. Kong, A. O. Govorov and M. A. Correa-Duarte, *J. Phys. Chem. C*, 2016, **120**, 11690-11699.
132. M. Achermann, *J. Phys. Chem. Lett.*, 2010, **1**, 2837-2843.
133. P.-F. Guo, S. Wu, Q.-J. Ren, J. Lu, Z. Chen, S.-J. Xiao and Y.-Y. Zhu, *J. Phys. Chem. Lett.*, 2010, **1**, 315-318.
134. A. I. Maaroof, H. Lee, K. Heo, J. Park, D. Cho, B. Y. Lee, M. J. Seong and S. Hong, *J. Phys. Chem. C*, 2013, **117**, 24543-24548.
135. J. Lee, P. Hernandez, J. Lee, A. O. Govorov and N. A. Kotov, *Nat. Mater.*, 2007, **6**, 291.
136. P. Vasa, R. Pomraenke, S. Schwieger, Y. I. Mazur, V. Kunets, P. Srinivasan, E. Johnson, J. E. Kihm, D. S. Kim, E. Runge, G. Salamo and C. Lienau, *Phys. Rev. Lett.*, 2008, **101**, 116801.
137. D. E. Gomez, K. C. Vernon, P. Mulvaney and T. J. Davis, *Nano Lett.*, 2010, **10**, 274-278.
138. P. R. Selvin, *Nat. Struct. Biol.*, 2000, **7**, 730.
139. H. J. Kong, T. R. Polte, E. Alsberg and D. J. Mooney, *Proc. Natl. Acad. Sci. U. S. A.*, 2005, **102**, 4300-4305.
140. X. Gao and J. Zhang, *ChemBioChem*, 2010, **11**, 147-151.
141. H. Sahoo, D. Roccatano, A. Hennig and W. M. Nau, *J. Am. Chem. Soc.*, 2007, **129**, 9762-9772.

142. C. Gell, T. Sabir, J. Westwood, A. Rashid, D. A. M. Smith, S.-A. Harris and P. G. Stockley, *J. Mol. Biol.*, 2008, **384**, 264-278.
143. A. I. Dragan and P. L. Privalov, in *Methods Enzymol.*, Academic Press, 2008, vol. 450, pp. 185-199.
144. A. L. Rodarte and A. R. Tao, *J. Phys. Chem. C*, 2017, **121**, 3496-3502.
145. A. I. Dolinnyi, *J. Phys. Chem. C*, 2015, **119**, 4990-5001.
146. H. Li, D.-e. Sun and Z. Liu, *Chem-Eur. J.*, 2015, **21**, 4944-4948.
147. X. Yang, H. Yu, X. guo, Q. Ding, T. Pullerits, R. Wang, G. Zhang, W. Liang and M. Sun, *Mater. Today*, 2017, **5c**, 72.
148. P. Wang, W. Liu, W. Lin and M. Sun, *J. Raman Spectrosc.*, 2017, **48**, 1144-1147.
149. T. J. Antosiewicz, S. P. Apell and T. Shegai, *ACS Photonics*, 2014, **1**, 454-463.
150. Q. Ding, Y. Shi, M. Chen, H. Li, X. Yang, Y. Qu, W. Liang and M. Sun, *Sci. Rep.*, 2016, **6**, 32724.
151. M. El Kabbash, A. Rahimi Rashed, K. V. Sreekanth, A. De Luca, M. Infusino and G. Strangi, *J. Nanomater.*, 2016, **2016**, 1-21.
152. J. L. Wu, F. C. Chen, Y. S. Hsiao, F. C. Chien, P. L. Chen, C. H. Kuo, M. H. Huang and C. S. Hsu, *ACS Nano*, 2011, **5**, 959-967.
153. E. Prodan and P. Nordlander, *Nano Lett.*, 2003, **3**, 543-547.
154. E. Prodan and P. Nordlander, *J. Chem. Phys.*, 2004, **120**, 5444-5454.
155. N. T. Fofang, N. K. Grady, Z. Fan, A. O. Govorov and N. J. Halas, *Nano Lett.*, 2011, **11**, 1556-1560.
156. A. Tsargorodska, M. L. Cartron, C. Vasilev, G. Kodali, O. A. Mass, J. J. Baumberg, P. L. Dutton, C. N. Hunter, P. Törmä and G. J. Leggett, *Nano Lett.*, 2016, **16**, 6850-6856.
157. Ł. Bujak, M. Olejnik, T. H. P. Brotosudarmo, M. K. Schmidt, N. Czechowski, D. Piatkowski, J. Aizpurua, R. J. Cogdell, W. Heiss and S. Mackowski, *Phys. Chem. Chem. Phys.*, 2014, **16**, 9015-9022.
158. Y. J. Li, Y. Hong, Q. Peng, J. Yao and Y. S. Zhao, *ACS Nano*, 2017, **11**, 10106-10112.
159. H. Ditlbacher, A. Hohenau, D. Wagner, U. Kreibig, M. Rogers, F. Hofer, F. R. Aussenegg and J. R. Krenn, *Phys. Rev. Lett.*, 2005, **95**, 257403.
160. I. R. Hooper and J. R. Sambles, *Phys. Rev. B*, 2002, **65**, 165432.
161. Z. Fang, L. Fan, C. Lin, D. Zhang, A. J. Meixner and X. Zhu, *Nano Lett.*, 2011, **11**, 1676-1680.
162. Y. Yan, C. Zhang, Y. Zheng Jian, J. Yao and S. Zhao Yong, *Adv. Mater.*, 2012, **24**, 5681-5686.
163. Y. Fedutik, V. Temnov, U. Woggon, E. Ustinovich and M. Artemyev, *J. Am. Chem. Soc.*, 2007, **129**, 14939-14945.
164. A. V. Akimov, A. Mukherjee, C. L. Yu, D. E. Chang, A. S. Zibrov, P. R. Hemmer, H. Park and M. D. Lukin, *Nature*, 2007, **450**, 402.
165. M. Fujihira, Y. Satoh and T. Osa, *Nature*, 1981, **293**, 206.
166. A. Fujishima and K. Honda, *Nature*, 1972, **238**, 37.
167. K. S. Novoselov, A. K. Geim, S. V. Morozov, D. Jiang, Y. Zhang, S. V. Dubonos, I. V. Grigorieva and A. A. Firsov, *Science*, 2004, **306**, 666.
168. A. Furube, L. Du, K. Hara, R. Katoh and M. Tachiya, *J. Am. Chem. Soc.*, 2007, **129**, 14852-14853.
169. Q. H. Wang, K. Kalantar-Zadeh, A. Kis, J. N. Coleman and M. S. Strano, *Nat. Nanotechnol.*, 2012, **7**, 699.
170. S. Najmaei, Z. Liu, W. Zhou, X. Zou, G. Shi, S. Lei, B. I. Yakobson, J.-C. Idrobo, P. M. Ajayan and J. Lou, *Nat. Mater.*, 2013, **12**, 754.
171. E. M. Purcell, H. C. Torrey and R. V. Pound, *Phys. Rev.*, 1946, **69**, 37-38.
172. K. T. Shimizu, W. K. Woo, B. R. Fisher, H. J. Eisler and M. G. Bawendi, *Phys. Rev. Lett.*, 2002, **89**, 117401.
173. E. Cohen-Hoshen, G. W. Bryant, I. Pinkas, J. Sperling and I. Bar-Joseph, *Nano Lett.*, 2012, **12**, 4260-4264.

174. Y. Deng, L. Tang, C. Feng, G. Zeng, J. Wang, Y. Lu, Y. Liu, J. Yu, S. Chen and Y. Zhou, *ACS Appl. Mater. Inter.*, 2017, **9**, 42816-42828.
175. L. Tang, R. Ji, X. Li, K. S. Teng and S. P. Lau, *J. Mater. Chem. C*, 2013, **1**, 4908-4915.
176. Q. Li, S. Zhang, L. Dai and L.-s. Li, *J. Am. Chem. Soc.*, 2012, **134**, 18932-18935.
177. N. Zhou, V. López-Puente, Q. Wang, L. Polavarapu, I. Pastoriza-Santos and Q.-H. Xu, *RSC Adv.*, 2015, **5**, 29076-29097.
178. H. F. Zarick, O. Hurd, J. A. Webb, C. Hungerford, W. R. Erwin and R. Bardhan, *ACS Photonics*, 2014, **1**, 806-811.
179. Y. C. Yen, P. H. Chen, J. Z. Chen, J. A. Chen and K. J. Lin, *ACS Appl. Mater. Inter.*, 2015, **7**, 1892-1898.
180. M. Chen, H. Yu, N. Zhao, L. Shao, J. Wang, S. V. Kershaw and A. L. Rogach, *ACS Nano*, 2014, **8**, 8208-8216.
181. S. Jin, E. DeMarco, M. J. Pellin, O. K. Farha, G. P. Wiederrecht and J. T. Hupp, *J. Phys. Chem. Lett.*, 2013, **4**, 3527-3533.
182. C. Lee, H.-J. Song, K. Jung, G. Lee, H. Choi, K. Ha, M. Choi, H.-J. Song, Y. Ko, J. Y. Kim, J. Song, C. Lee, K. Ahn and J.-K. Lee, *ACS Nano*, 2014, **8**, 2590-2601.
183. B. Wu, T. Z. Oo, X. Li, X. Liu, X. Wu, E. K. L. Yeow, H. J. Fan, N. Mathews and T. C. Sum, *J. Phys. Chem. C*, 2012, **116**, 14820-14825.
184. S. Balci, B. Kucukoz, O. Balci, A. Karatay, C. Kocabas and G. Yaglioglu, *ACS Photonics*, 2016, **3**, 2010-2016.
185. S. Balci, B. Kucukoz, A. Karatay, G. Yaglioglu, O. Balci and C. Kocabas, *ACS Photonics*, 2016, **3**, 2010-2016.
186. K. Nakayama, K. Tanabe and H. A. Atwater, *Appl. Phys. Lett.*, 2008, **93**.
187. T. Ming, H. Chen, R. Jiang, Q. Li and J. Wang, *J. Phys. Chem. Lett.*, 2012, **3**, 191-202.
188. T. Ozel, P. L. Hernandez-Martinez, E. Mutlugun, O. Akin, S. Nizamoglu, I. O. Ozel, Q. Zhang, Q. Xiong and H. V. Demir, *Nano Lett.*, 2013, **13**, 3065-3072.
189. F. Nan, S. J. Ding, L. Ma, Z. Q. Cheng, Y. T. Zhong, Y. F. Zhang, Y. H. Qiu, X. Li, L. Zhou and Q. Q. Wang, *Nanoscale*, 2016, **8**, 15071-15078.
190. T. J. Antosiewicz, S. P. Apell and T. Shegai, *ACS Photonics*, 2014, **1**, 454-463.
191. H. Xu, S. Kawata, D. J. Bergman, X. Zhu and H. Wei, presented in part at the SPIE/COS Photonics Asia 2016.
192. X. Dang, J. Qi, M. T. Klug, P. Y. Chen, D. S. Yun, N. X. Fang, P. T. Hammond and A. M. Belcher, *Nano Lett.*, 2013, **13**, 637-642.
193. K. Wu, J. Chen, J. R. McBride and T. Lian, *Science*, 2015, **349**, 632.
194. J. Bellessa, C. Bonnand, J. C. Plenet and J. Mugnier, *Phys. Rev. Lett.*, 2004, **93**, 036404.
195. C. Symonds, J. Bellessa, J. C. Plenet, A. Bréhier, R. Parashkov, J. S. Lauret and E. Deleporte, *Appl. Phys. Lett.*, 2007, **90**.
196. P. Yu, X. Wen, Y.-C. Lee, W.-C. Lee, C.-C. Kang and J. Tang, *J. Phys. Chem. Lett.*, 2013, **4**, 3596-3601.
197. D. C. Marinica, H. Lourenco-Martins, J. Aizpurua and A. G. Borisov, *Nano Lett.*, 2013, **13**, 5972-5978.
198. S. Bhattacharyya and A. Patra, *J. Photochem. Photobiol., C*, 2014, **20**, 51-70.
199. C. D. Lindstrom and X. Y. Zhu, *Chem. Rev.*, 2006, **106**, 4281-4300.
200. Q. Li, H. Wei and H. Xu, *Nano Lett.*, 2015, **15**, 8181-8187.
201. K. N'Konou, L. Peres and P. Torchio, *Plasmonics*, 2017, **13**, 297-303.
202. P. A. Hobson, S. Wedge, J. A. E. Wasey, W. L. Barnes and I. Sage, *Adv. Mater.*, 2002, **14**, 1393-1396.

203. E. Dulkeith, A. C. Morteani, T. Niedereichholz, T. A. Klar, J. Feldmann, S. A. Levi, F. C. van Veggel, D. N. Reinhoudt, M. Moller and D. I. Gittins, *Phys. Rev. Lett.*, 2002, **89**, 203002.
204. Y. Fedutik, V. V. Temnov, O. Schops, U. Woggon and M. V. Artemyev, *Phys. Rev. Lett.*, 2007, **99**, 136802.
205. P. Anger, P. Bharadwaj and L. Novotny, *Phys. Rev. Lett.*, 2006, **96**, 113002.
206. M.-T. Cheng, S.-D. Liu, H.-J. Zhou, Z.-H. Hao and Q.-Q. Wang, *Opt. Lett.*, 2007, **32**, 2125-2127.
207. A. Neogi, C.-W. Lee, H. O. Everitt, T. Kuroda, A. Tackeuchi and E. Yablonovitch, *Phys. Rev. B*, 2002, **66**.
208. S. Kuhn, U. Hakanson, L. Rogobete and V. Sandoghdar, *Phys. Rev. Lett.*, 2006, **97**, 017402.
209. K. Okamoto, I. Niki, A. Shvartser, Y. Narukawa, T. Mukai and A. Scherer, *Nat. Mater.*, 2004, **3**, 601-605.
210. K. Okamoto, M. Funato, Y. Kawakami and K. Tamada, *J. Photochem. Photobiol., C*, 2017, **32**, 58-77.
211. D. Nepal, L. F. Drummy, S. Biswas, K. Park and R. A. Vaia, *ACS Nano*, 2013, **7**, 9064-9074.
212. A. Fujiki, T. Uemura, N. Zettsu, M. Akai-Kasaya, A. Saito and Y. Kuwahara, *Appl. Phys. Lett.*, 2010, **96**.
213. O. Yutaka, S. Takumi, K. Yoshitaka and Y. Katsumi, *J. Phys. D: Appl. Phys.*, 1999, **32**, 87.
214. B. J. Lawrie, K. W. Kim, D. P. Norton and R. F. Haglund, Jr., *Nano Lett.*, 2012, **12**, 6152-6157.
215. E. Eizner, O. Avayu, R. Ditcovski and T. Ellenbogen, *Nano Lett.*, 2015, **15**, 6215-6221.
216. C. Liu, J. Zhang, Y. Chen, P. Jing, L. Zhang, H. Zhao, X. Fu and L. Wang, *Mater. Res. Express*, 2018, **5**.
217. P. J. Cheng, J. A. Cheng, Z. W. Lin and C. H. Tien, *SID Symposium Digest of Technical Papers*, 2012, **40**, 1730-1733.
218. L. Weihua, C. Yaqian, W. Peijie and S. Mengtao, *Langmuir*, 2017, **33**, 12102-12107.
219. D. E. Gómez, H. Giessen and T. J. Davis, *J. Phys. Chem. C*, 2014, **118**, 23963-23969.
220. R. Thomas, A. Thomas, S. Pullanchery, L. Joseph, S. M. Somasundaran, R. S. Swathi, S. K. Gray and K. G. Thomas, *ACS Nano*, 2018, **12**, 402-415.
221. D. S. Dovzhenko, S. V. Ryabchuk, Y. P. Rakovich and I. R. Nabiev, *Nanoscale*, 2018, **10**, 3589-3605.